Master's thesis

NTNU
Norwegian University of Science and Technology
Faculty of Engineering
Department of Structural Engineering

Martin Mascella

Global Analysis of Submerged Floating Tunnels Under Hydrodynamic Loading

Master's thesis in Civil Engineering-Structures
Supervisor: Nils Erik Anders Rønnquist
June 2020

NTNU
Norwegian University of
Science and Technology

Martin Mascella

Global Analysis of Submerged Floating Tunnels Under Hydrodynamic Loading

Master’s thesis in Civil Engineering-Structures
Supervisor: Nils Erik Anders Rønnquist
June 2020

Norwegian University of Science and Technology
Faculty of Engineering
Department of Structural Engineering

NTNU
Norwegian University of
Science and Technology

POLITECNICO
MILANO 1863

School of Civil, Environmental and Land Management Engineering
Master degree in Civil Engineering-Structures

Global Analysis of Submerged Floating Tunnels Under Hydrodynamic Loading

***Supervisor*: Prof. Federico Perotti**
***Co-supervisor*: Prof. Luca Martinelli**

Norwegian University of Science and Technology

***Erasmus supervisor*: Prof. Nils Erik Anders Rønnquist**
***Erasmus co-supervisor*: Postdoc Øyvind Wiig Petersen**

***Author*:**
Martin Mascella, 913074

Academic Year 2019/2020
Session I

To my family

Summary

This master's thesis includes several preliminary designs of Submerged Floating Tunnels (SFT) and its responses to hydrodynamic loading. SFT is a never built transport structure, which can be use for crossing lakes, straights or fjords. In this thesis are considered tether stabilized SFTs , which requires deep water foundations too.
Generally, deep water foundations and anchoring system installation are highly dependent on the water depth and soil characteristics, and they might not be feasible for really deep waters. In this thesis project case studies are carried out in order to eventually reduce the number of necessary tethers.

First, a detailed literature review of existing SFT designs and reports is included. It focuses on the differences and similarities of the concepts, different proposed tunnel cross-sections, supporting systems and tunnel alignments are compared.
The thesis aim is to identify the effects of the tunnel alignment on the structural response. A conceptual design is performed using simplified methods and literature recommendations. Simple and effective draft designs are obtained in this phase.

Four different design concepts are developed. Three models have a double curvature configuration of the tunnel and they differ in the tether arrangment and number, and buoyancy weight ratio. One model is a straight SFT with vertical tethers at mid-span. In one model also a pulley connection between the tethers and the tunnel is implemented.

Static, modal and dynamic analysis have been performed using both the software Abaqus, and analytical methods. Through the static analysis, which neglects the fluid-structure interaction, is highlighted the dependence of each model on the buoyancy weight ratio amplitude. A non-conservative harmonic regular wave dynamic analysis is performed on the four models in order to compare their responses. This analysis is also compared to an irregular wave analysis in order to demonstrate that the assumptions made during the harmonic analysis are highly conservative. Sensitivity tests on the loading conditions and the end connection stiffness are performed. It results suitable a stiffness in between the pin and the clamped connections. Overall it appears that the double arch configuration has a sufficient lateral stiffness and so inclined tethers are not needed. Moreover the structural dynamic oscillations are reduced adopting a double curvature in comparison to a straight tunnel configuration.

Sintesi

Nella presente tesi di laurea magistrale sono realizzati diversi progetti preliminari di ponti di Archimede, con le relative risposte strutturali dovute a carichi idrodinamici. Il ponte di Archimede è una struttura mai costruita in passato, e può essere utilizzato per attraversamenti di laghi, stretti o fiordi.
In questa tesi sono considerati ponti di Archimede con l'ausilio di acoraggi in campata, i quali richiedono fondazioni in profondità. Generalmente, il sistema di acoraggio e le relative fondazioni variano in base alla profondià e alle caratteristiche del suolo, ed in alcuni casi la realizzazione può risultare complessa. Nel presente progetto di tesi sono presi in considerazione alcuni casi di studio, e approfondite ricerche sono svolte per ridurre il numero necessario di ancoraggi.

Innanzitutto, una dettagliata revisone della letteratura e di progetti esistenti viene riportata. Particolare attenzione è rivolta alle differenze e alle similitudini nelle diverse soluzioni progettuali. Inoltre sono confrontate diverse sezioni trasversali , sistemi di supporto e allineamenti longitudinali del tunnel.
Lo scopo della tesi è quello di identificare e valutare gli effetti della curvatura del tunnel sulla risposta strutturale. Una analisi concettuale viene eseguita, con l'ausilio di metodi analitici e raccomandazioni letterarie, per ottenere semplici ed efficaci proposte progettuali.

Quattro differenti modelli strutturali vengono creati. Tre di essi hanno in comune la doppia curvatura della sezione longitudinale e differiscono tra di loro per la disposizione ed il numero di ancoraggi, ed il rapporto peso-galleggiamento. Un ultimo modello è un ponte di Archimede rettilineo con implemento di ancoraggi verticali in mezzeria. In uno dei modelli considerati è inserita una pulleggia come connessione interposta tra il tunnel i gli ancoraggi.

Analisi statiche, modali e dinamiche sono realizzate sia con il software Abaqus/Aqua che con metodi analitici. Grazie alla analisi statica, la quale trascura l'interazione fluido-struttura, viene evidenziato l'effetto su di ogni modello del rapporto peso-galleggiamento. Una analisi dinamica con onde armoniche regolari ed ipotesi non conservative viene effettuata per confrontare le risposte strutturali dei vari modelli. In aggiunta, una analisi non deterministica con onde irregolari viene effettuata per valutare il grado di affidabilità della analisi con onde armoniche, dal confronto risulta che l'analisi armonica è conservativa. Sono svolti infine studi di sensitività sulle condizioni di carico e sulla rigidezza delle connessioni alle spalle del ponte. Da essi risulta che la connesione più adatta è compresa tra un semplice appoggio ed un incastro. Complessivamente risulta che la configurazione con doppia curvatura ha una sufficiente rigidezza laterale e quindi gli ancoraggi inclinati sono innecessari. Inoltre, le oscillazioni dinamiche sono ridotte se viene adottata una doppia curvatura della sezione longitudinale rispetto ad un allineamento rettilineo.

Preface

This Master's thesis is the concluding part of the Master Degree in Civil Engineering, at Politecnico di Milano. The thesis is written during 2020 at the Norwegian University of Science and Technology (NTNU).

I would like to thank my supervisors and co-supervisors of NTNU and Politecnico di Milano, and Arianna Minoretti of Statens Vegvesen, for making this great experience possible. Without their guidance, immense knowledge and passionate participation the study would not be completed.

Special thanks goes to Øyvind Petersen for the great technical support during the process. Gratitude is also extended to Prof. Federico Perotti and Prof. Luca Martinelli, who first introduced to me Submerged Floating Tunnels.

I would also like to thank Prof. Anders Rønnquist and Arianna Minoretti who has contributed with interesting discussions and valuable recommendations.

Martin Mascella
Trondheim, June 2020

Table of Contents

List of Tables

List of Figures

Abbreviations

BWR = Buoyancy Weight Ratio
CDBT = Center Distance Between Tunnels
CDF = Cumulative Distribution Function
DFT = Discrete Fourier Transform
DNV = Det Norske Veritas
DOF = Degree of Freedom
FE = Finite Element
FEM = Finite Element Model
FFT = Fast Fourier Transform
HH-T = Hilbert-Hughes-Taylor
JONSWAP = Joint North Sea Wave Project
NPRA = Norwegian Public Roads Administration
PDF = Probability Density Function
RWA = Regular Wave Analysis
SFT = Submerged Floating Tunnel
SFTB = Submerged Floating Tube Bridge
SLS = Serviceability Limit State
ULS = Ultimate Limit State
VIV = Vortex Induced Vibration

Symbols

A = External cross sectional area
A_c = Cross sectional area
a_{max} = Acceleration limit state
$[C]$ = Damping matrix
C_a = Added mass coefficient
C_d = Drag force coefficient
C_m = Inertia coefficient
c_p = Phase velocity of a regular wave
d = Water depth
D_e = Tunnel outer diameter
D_i = Tunnel inner diameter
E = Elastic modulus
f = Steel volume fraction / Rise of the arch
F = Force vector
$f(t)$ = Dynamic load
f_{ck} = Characteristic compression strength
f_{ctm} = Tensile strength
F_D = Drag force
F_m = Inertia force
f_{yk} = Characteristic yield strength
g = Gravitational constant
G = Shear modulus
H = Wave height
H_s = Significant wave height
I = Moment of inertia
k = Wave number
$[K]$ = Stiffness matrix
$K_h(n)$ = Modal heave stiffness
$K_s(n)$ = Modal sway stiffness
k_{tether} = Tether axial stiffness
L = Wave length
L_i = Tether length
$[M]$ = Mass matrix
m_a = Added mass
$M_h(n)$ = Modal heave mass
m_i = Generalized mass of the $i - mode$
$m_{i,eff}$ = Effective mass of the $i - mode$
$M_s(n)$ = Modal sway mass
m_{tunnel} = Mass of the tunnel per unit length
m_{tether} = Mass of the tether per unit length

M_x = Bending moment around the $x - axis$
M_y = Bending moment around the $y - axis$
N = Axial force
p = Water pressure
p_0 = Atmospheric pressure
q = Net distribured force
R = Radius of curvature
R_D = Reduction factor
R_e = External radius
R_i = Internal radius
s = Sea state parameter
S_x = Power spectrum
S_y = Shear force on the $y - axis$
S_z = Shear force on the $z - axis$
t = Time
T = Period
t_c = Thickness of reinforced concrete layer
t_1 = Thickness of external steel layer
t_2 = Thickness of internal steel layer
T_i = Tether tension
T_p = Significant wave period
T_1 = Axial force in the inclined tether
T_2 = Axial force in the vertical tether
V = Volume of the tunnel cross section
$\mathbf{v}$ = Fluid velocity vector
$\dot{v}$ = Fluid acceleration
v_2 = Fluid velocity in the shielded tunnel
W = Fluid domain
w = Wave energy directional function
x = Displacement / Longitudinal coordinate
$X(\omega)$ = Fourier transform
X_k = Discrete Fourier transform
$\dot{x}$ = Tunnel velocity
$\ddot{x}$ = Tunnel acceleration
$\{x\}$ = Tunnel vector of displacements
$\{\dot{x}\}$ = Tunnel vector of velocities
$\{\ddot{x}\}$ = Tunnel vector of accelerations
y = Horizontal coordinate
z = Vertical coordinate
z_s = Free surface coordinate

0.0.1 Greek

α = Rayleigh damping mass coefficient
ρ = Density
Δ = Gradient
ϕ = Velocity potential
$\phi(n, x)$ = Assumed modal shape function
ω = Angular frequency
ω_p = Peak wave frequency
γ^δ = Peak enhancement factor
σ_0 = Width of the peak region
β = Wave angle of attack
β = Rayleigh damping stiffness coefficient
Θ_{rel} = Relative angle between wave direction and tunnel axis
Γ = Gamma function
Γ_i = Participation factor of the $i - mode$
$\{\Phi\}$ = Eigenvector
ψ = Damping ratio
δ_{max} = Deflection limit state
ν = Poisson ratio
ε = Strain
μ = Friction coefficient

Chapter 1

Introduction

Submerged Floating Tunnel (SFT), known as Archimedes Bridge in Italy is an innovative typology of structure, which can be used to cross straits, large lakes or fjords. It generally consists of a tunnel tube suspended in water, anchor cables and deep water foundations. A typical submerged floating tunnel is shown in Fig. 1.1.

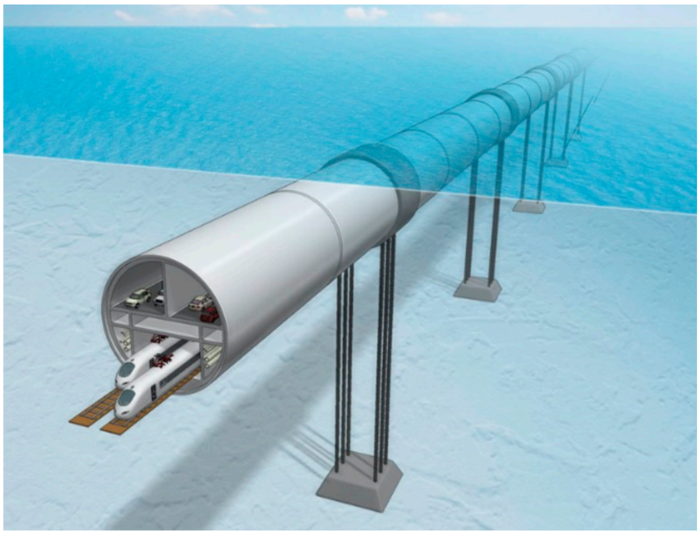

Figure 1.1: Tether stabilized submerged floating tunnel,[Won et al., 2019]

The submerged floating tunnel is a never built structure, but in the last decades many research groups are becoming more interested on it, especially in Italy, Norway and Japan. The growing interest consists in the fact that SFT becomes a viable alternative for transport structure, especially in deep water crossing.

The majority of the previous SFT's projects are focused on large crossing, where a suspended bridge might not be a feasible alternative. However, SFT might work brilliant for relatively short crossing due to two particular aspects:

- *Invisible structure.* Places of special beauty or historical value should be preserved for the future, this can be done opting for a SFT rather than a bridge.

- ◇ *Reduced environmental impact.* Local acoustic pollution and exposure to emissions from vehicle are reduced.

An other important aspect to be considered for the construction of the first SFT is the user perception of danger, to which users could gradually get used to if the firs ever built tunnel is relatively short.
Generally, deep water foundations and anchoring installation are expensive, time consuming, and highly dependent on the water depth. The objective of this thesis project is to analyze whether the number of anchoring bars might be reduced modifying the tunnel alignment.

The first chapter is an introduction to the thesis. The chapter contains the thesis objectives, a short background study, and a description of the structure of the report.
Chapter two is a detailed review of existing SFT projects, with focus on the design features. Several cross-sections, supporting systems and tunnel alignment are compared.

Chapter three describes the structural loads acting on the SFT. The most relevant hydrodynamic theories are also reported along the chapter.
In chapter four is carried out a conceptual design of the structure. Environmental actions are modelled through simplified procedure and an analytical method is developed. A preliminary structure is defined considering also literature recommendations.

Chapter five describes the modelling of the main global finite element model. It also includes the geometrical parameters of all the tunnels analyzed, and an extensive description of the static and dynamic analysis set up. Sensitivity study are also explained through this chapter.

Chapter six concerns the different analysis results for all the analysis described in chapter five. The most important results are given with a belonging description, supported by plots and discussion of the results.

The thesis conclusion is presented, based upon the results from chapters six and four. In addition, multiple suggestions for further work are herein listed.

Chapter 2

Literature Review

The following is adapted from the author's project thesis. In the literature the Submerged Floating Tunnel (SFT) is referred with different acronyms such as Submerged Floating Tube Bridge (SFTB) and Archimedes' Bridge. It is a novel structure that can be used to cross deep waters such as fjord, lakes, rivers, canals or straits. The structure has never been built, but it has been considered and designed in different locations for the E-39 project in Norway, for the Messina strait in Italy, the Qiandao Lake in the Republic of China and various sites in Japan. It generally consists of a tunnel tube suspended in water, an anchoring system, and deep-water foundations or pontoons. SFTs are generally used where the water depth is larger than 50 meters, the crossing length is larger than 1 km and the preservation of a scenic view or a natural habitat is considered important [Perotti et al., 2013]. Moreover, it has a great advantage in comparison with a subsea tunnel in fjord crossing where the water depth is large in comparison with the length.

2.1 Design Features

Generally, the tunnel cross section is designed so that the buoyancy covers the structural weight and the tunnel is then subjected to an upward force, which is exerted by a fluid [Won et al., 2019]. However, in some of the latest design where pontoons are used the tunnel is subjected to a downward force. The balance of buoyancy weight ratio plays an important role to control the dynamic behaviour of SFTs when tension leg is used to stabilize a structure under water.

There are different types of tube cross sections, like circular, elliptical, polygonal and rectangular. The configuration depends not only on structural purposes, but also on the facilities and the traffic lanes considered, in some cases it is included a railway or a pedestrian walk.

The driving criterion for the design of the concrete tube is the water tightness criterion in SLS, this requirement is common in all the designs of SFTs. Therefore, the membrane forces in the concrete shall be always of compression and cracks should be avoided. This criterion governs the amount of prestressing and post tensioning level in the concrete tubes.

In the design of the Bjørnafjord's SFTB it has been chosen a twin tube cross section, which has several advantages. In case of foreseen scenarios in one tube, the other can be used as escape route by the users. The twin tube cross section has by test shown a stable behaviour under current and wave action, eliminating the need for extra design remedies to eliminate uncontrolled motion [Olsen et al., 2016]. Moreover wind-tunnel tests underline twin tube as a preferable cross section rather than a rectangular box.
In most of the projects the cross section is made by concrete and steel reinforcement, while in the Prototype in Qindao Lake the cross section is a steel-concrete-aluminium sandwich [Mazzolani et al., 2008]. The external aluminium layer, which is corrosion-resistant, works as an energy absorber in case of external impact, due to its alveolate shape. However, in this case the length of the tunnel is 100m, while in the Bjørnafjord project it is over 5000 meters.

The external diameter, on the other hand, has the prominent influence on the ratio between the water buoyancy and the tunnel weight (BWR), which is expected to be larger than one. It was detected that the increase of the BWR ratio, that usually ranges between 1.25 to 1.4, can lead to impressive improvements of the SFT response to extremely severe sea states [Perotti et al., 2013]. The BWR is controlled by the water ballast, which is important during both the installation procedures and functioning of the structure. The size of the ballast is fundamentally different between the pontoon solution and the tether solutions that are described afterwar.

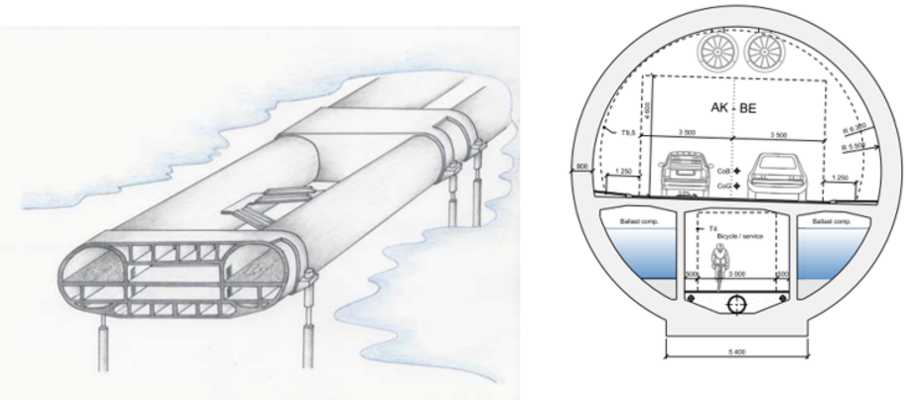

Figure 2.1: Twin tube configuration ,[Olsen et al., 2016]

Generally, cylindrical shapes are preferred because they minimize the drag force due to current, and the vortex shedding induced vibrations. In addition, adopting a round shape for the tunnel prevent rotational moment due to fluid forces. Moreover, it is the best shape for uniform inner/outer pressure. The only drawback is that they are more expensive in the fabrication.

The elliptical cross section has a greater impact resistance due to explosion to that of rectangular and circular cross section. The analysis of the impact acceleration of pipe sections with different cross sections, shows that the impact acceleration peak values of the rectangular cross section are the biggest in both flow direction, followed by those of the circular and then the elliptical shapes, [Gang et al., 2020].

Another type of cross section is the triple deck, Fig. 2.2. The advantages for this proposal are the efficient shape for primary load carrying of vertical and horizontal loads, and the reduced volume concrete compared to the twin tube solution. However, it is less efficient for secondary load carrying (plate bending), and it is subjected to high drag forces and vortex shedding. This solution is suitable only for single span tunnel, [Xiang et al., 2017].

Figure 2.2: Triple deck cross section, [Xiang et al., 2017]

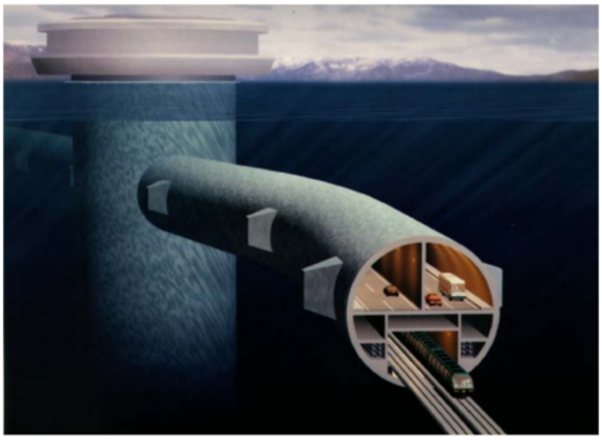

Figure 2.3: Funka Bay SBT crossing in Japan, [Kanie, 2010]

In japan the first feasibility design of a SFT is referred to the Funka Bay crossing, Fig. 2.3, which has a total length of 30Km and a maximum depth of 120m, [Kanie, 2010]. The tunnel consists of a single cylinder with a steel skin plate for the perimeter of the tunnel and light weight concrete for the body, the buoyancy weight ratio is 1.5. In this design, special attention is given to arrange the legs in the cross section not to cause rotational torque by restoring force with horizontal and vertical displacements. For that purpose, it is introduced the idea of a flexible leg installed around the tunnel through the frictionless sheath to tie the left and right tethers. Then the forces acting in the legs are automatically kept in equilibrium.

Due to large reaction forces in the landafalls of the SFTs, it is a common design strategy to increase the cross-section dimensions in these regions.

2.1.1 Horizontal Bracing-Twin Tube SFTB

A rigid connection between the two tubes is achieved by diagonal bracings. Some bracings with regular spacing are adopted to secure escape routes, control rooms and other facilities. Horizontal bracing between the main cross tubes is required to limit the lateral wave induced flexural response to an acceptable level.

A comparative study is presented in [Olsen et al., 2016]. It outlines the truss model as the best option compared to a Vierendeel model, Fig. 2.4. Whereas the truss and Vierendeel configuration exhibit similar global response in terms of tube axial forces, their local response differs significantly. The Vierendeel frame rotates under pure shear, consequently secondary bending moment in the main tubes are much higher.

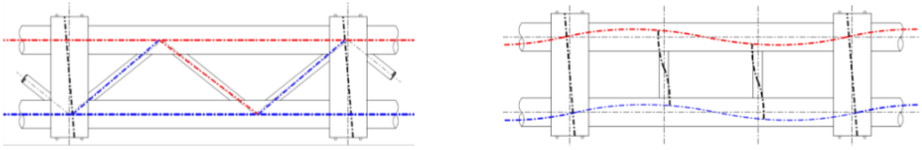

Figure 2.4: Comparison horizontal bracing system, [Olsen et al., 2016]

2.2 SFT with Different Support Systems

An anchoring system can be any method used for securing the structure to a foundation system or to the ground. In previous designs, 6 types of anchoring system in submerged floating tunnels have been considered,(1) pontoons on the water surface,(2) fixed support, (3) tension legs to the bottom (tethers),(4) horizontal and vertical support, (5) horizontal anchoring, (6) single span solution. There are no modern models referring to the fixed support solution where columns on the sea bottom are needed.
Each concept has its own cons and pros. Thus, the first step before any further analysis should be to evaluate the technical feasibility of each concept, and focus put on the most promising concepts [Xiang et al., 2017].

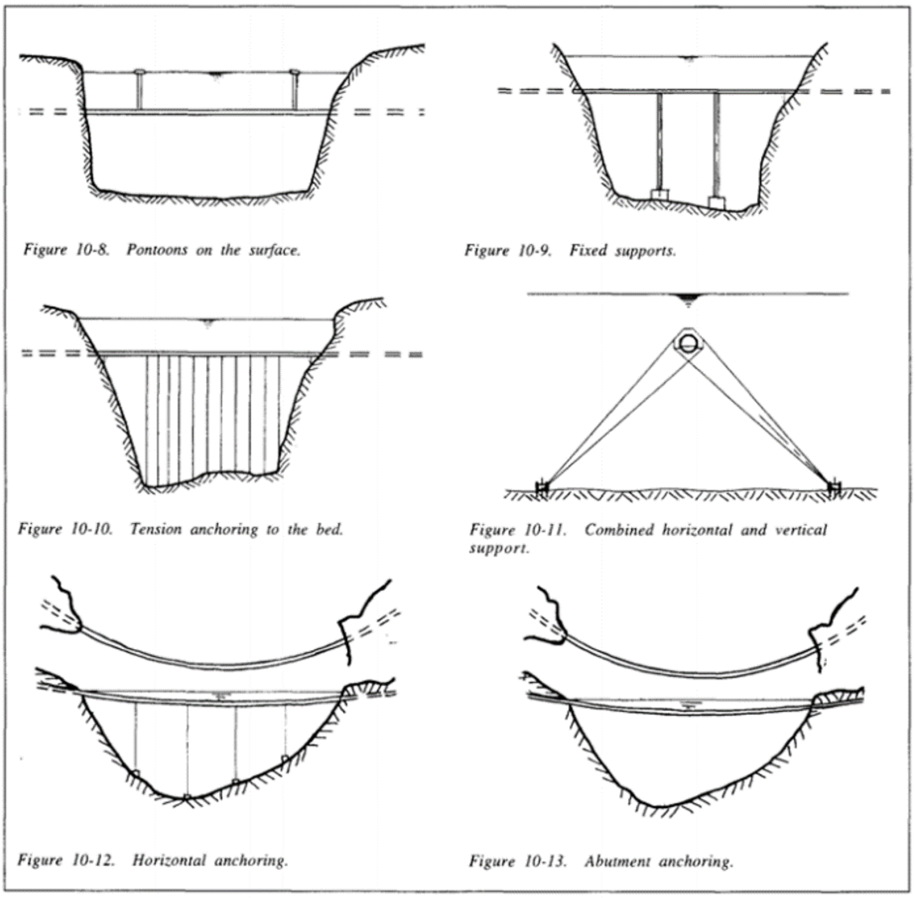

Figure 10-8. Pontoons on the surface.

Figure 10-9. Fixed supports.

Figure 10-10. Tension anchoring to the bed.

Figure 10-11. Combined horizontal and vertical support.

Figure 10-12. Horizontal anchoring.

Figure 10-13. Abutment anchoring.

Figure 2.5: Different types of SFTs, characterized by different support systems, [Feriani et al., 2006]

◇ *Single Span Solution*

It does not need intermediate foundations therefore it has a less complex installation. There are no risks due to settlements or tether damage. It is limited for short span due to the high forces in the abutments, this concept can be optimized choosing the best radius of curvature of the tunnel.

◇ *Tether and Pontoon stabilized solution*

Comparison between the tether and the pontoon stabilized SFTB is taken from the study for the Bjørnafjord crossing, [Olsen et al., 2016]. The main difference is that in one case is needed negative buoyancy and in the other case positive buoyancy.

The pontoons interact with the waves in the surface, and that will transfer more motion to the tube compared to the tether. Moreover, they are more vulnerable to ship impact. To that point a solution is proposed in [Reinertsen and Group, 2012], where a weak link solution is introduced between in the shafts to prevent overstressing of the tunnel structure. The tunnel is so designed to tolerate loss of one pontoon without losing its structural integrity or suffering other structural damage. The installation of pontoons is easier than tethers.

The tether stabilized SFT gives no visual impact from shore and free ship passage, but it is slightly more sensible to submarine passage than the previous solution. Two basic elements have been considered in [Perotti et al., 2018] as tether solutions, cables and tubular sections. The latter is deemed to be preferable for inclined long elements, since can benefit from buoyancy in order to avoid catenary effects, which unavoidably penalize serviceability performance.
The configuration in Fig. 2.6 with two couples of vertical cables and a W-shaped group of cables in the mid-span guarantees the best performances under the hydrodynamic loads, from the point of view of both the tunnel and the cables. It is therefore, recommended for areas with high seismic actions and currents.

It has been proved that discrepancy between the results of the 2D or 3D models of SFTs decreases as the tether stiffness increases. This indicates that the adoption of Morison's equation for evaluating the fluid loading on the tunnel is a reasonable assumption when the tether stiffness is high [Tariverdilo et al., 2011].

Results of Parametric Vibration in the SFT system with different cable inclinations, and effect of flow velocity, shows that a cable angle of 45° can weaken the coupling effect of vibration between the cables and the tube [Yiqiang and Chunfeng, 2013].

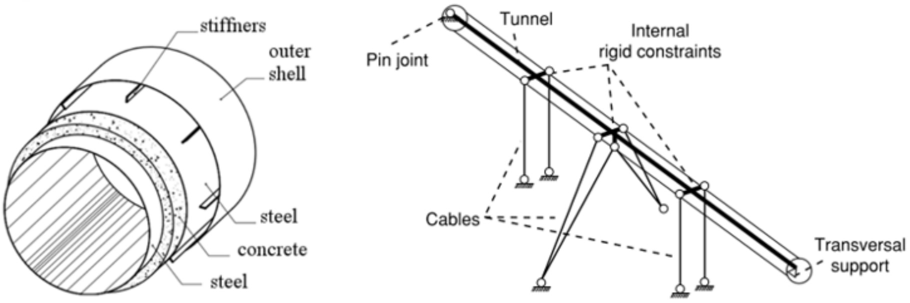

Figure 2.6: Tether tubular cross section (left), [Mazzolani et al., 2008], and tether layout (right) ,[Perotti et al., 2018]

2.3 Horizontal Alignment

Several horizontal alignments have been considered in [Olsen et al., 2016] including straight line, single curve and double S-shape. Despite producing the longest centreline, the arch shape is selected for reasons of its flexibility to thermal expansion, favourable roadway layout.

Owing to the fixed constraint conditions, a considerable in-plane flexural rigidity and moderate arch axial compression, the tube bridge has a high in-plane buckling and snap-through resistance. Hence, a higher span-to-rise ratio can be utilized to better suit economy and dynamic performance.

In the design of Sognefjord crossing, [Reinertsen and Group, 2012], is used a Radius of curvature of 2681 m. Whereas, in order to maintain a provident speed limit of 120 km/h, a minimum radius R_{min} equal to 3200m is reported in [Olsen et al., 2016], which corresponds to an arch with a span-to-rise ratio of 4.0. It is important to notice that the arch configuration has been mostly proposed for the fjord crossings, due to the fact that the currents mainly maintain the same direction during time.

2.4 Pros and Cons of SFTs

SFT has superior advantages to conventional crossing technologies such as bridge or subsea tunnel but it also requires technological innovation to keep the structural stability against environmental disturbance with safety measures for unexpected emergency,[Perotti et al., 2013]. Some of the advantages are listed below:

- *Very small environmental impact, since it is an invisible structure*
- *Reduced interference with the passage of ships*
- *Zero downtime due to weather conditions*
- *Can be almost entirely removed at the end of the lifetime*
- *The cost is not very dependent on the length*

On the contrary some of the cons which explain why it is a never-built structure are listed below:

- *More complex safety assessment*
- *There are difficulties at the installation phase*
- *Adverse psychological reasons for the users*
- *Innovative structures need more challenges and tests*

The pros justify the great interest in SFTs. On the other hand, more investigations are needed, and the social impact has to be considered too.

2.5 Buoyancy Weight Ratio

The buoyancy weight ration (BWR) changes the vibration characteristics and affect the internal forces amplitude, of the SFT. Selecting an appropriate BWR value is a significant design step in the design of a SFT [Lin et al., 2018].

Experiments were carried out by [Hong and Ge, 2010], shows that a change in the BWR results in a variation of dynamic responses. An other research computed by [Long et al., 2009], where the effect of tunnel length and BWR on the dynamic response were studied, states that the BWR has an higher contribution than the tunnel length, if the same boundary conditions are used.

Slack phenomena in the tethers is largely dependent on the BWR and wave height. A larger BWR reduces the probability of slacking in tethers, while a larger significant wave height increases it [F. et al., 2011]. Vertical forces in SFT are mainly due to buoyancy forces, the BWR is positive for tether stabilized SFT and negative for pontoon stabilize SFT [Olsen et al., 2016].

Considering a tether stabilized SFT, and higher BWR has some advantages and drawbacks. Generally, for tether stabilized SFTs the BWR ranges in between 1.2 to 1.5.

Chapter 3

Theory

3.1 General Loads

The following is adapted from the author's project thesis. The chapter will summarize all the relevant loads acting on SFTs after the installation procedure. The SFT is mainly subjected to static, dynamic and impact loads.Loads in SFTs can be divided in 4 main groups.

Permanent actions:

- *Dead load*
- *Buoyancy*
- *Post-tensioning*

Environmental actions:

- *Current*
- *Waves*
- *Earthquake-Seaquake*
- *Water pressure-Tidal load*

Service Actions:

- *Traffic*
- *Ballast*

Accidental actions:

- *Explosion*
- *Ship/Submarine collision*
- *Flooding*

In this report collisions, earthquakes, flooding and explosion will not be considered.

3.2 Permanent Actions

3.2.1 Dead Load

The dead load, also called self-weight of the structure, includes the weight of tunnel sections, asphalt, structural elements as bracing system, and permanent equipment.

3.2.2 Buoyancy

The term buoyant force refers to the upward-directed force that water exerts on the SFT which is completely immersed in the fluid. The Archimedes principle states that the buoyant force exerted on an object that is submerged partially or completely in a fluid is equal to the weight of the fluid that is displaced by the object.

$$BuoyancyForce = \rho * V * g \tag{3.1}$$

where V is the volume of the structure, ρ is the mean sea water density, and g is the gravitational constant.

The buoyancy weight ratio (BWR) is an important parameter in SFT. In the case of tether stabilized SFTs the BWR usually ranges between 1.2-1.5. An high value of BWR guarantees permanent tension in the tethers and reduces the motion amplitudes, but generates higher bending moments that can be critical at the landfalls.

3.3 Environmental Actions

3.3.1 Waves Theory

Waves are the response made by the water to gravity, and surface tension caused by wind. The size of the waves increases with the time that the wind has been blowing and the fetch size. The waves running away from the wind that has generated them far away from the local site are called “swell” and they are present even when local wind is not present. The wave heights are limited, theoretically to one seventh of the wavelength.

In the analysis of the SFT is usually adopted the Airy wave theory as in [Olsen et al., 2016] and [Feriani et al., 2006]. The basic assumptions of this theory are that the fluid is incompressible and inviscid, and the flow is irrotational. Typically, a wave motion can be described geometrically by three parameters, the height H, the length L, and the water depth d. The Airy wave is a linearize theory and it is justified when the Ursell’s number (3.2) is much smaller than 1 [Kuznetsov et al., 2009].

$$\frac{HL^2}{d^3} << 1 \tag{3.2}$$

The airy wave theory is implemented in Abaqus, and here will be reported the basic equations on which the theory is based. For detailed information one can refer to [Moreau, 2003].

- Conservation of mass
  $$\rho_t + \nabla(\rho \mathbf{v}) = 0 \quad in \quad W \tag{3.3}$$
  where, the subscript t stays for partial derivative in time, ρ is the fluid density, ∇ is the gradient, and **v** is the fluid velocity vector in the domain W.
- The fluid is incompressible
  $$\nabla \mathbf{v} = 0 \quad in \quad W \tag{3.4}$$
- Euler equation
  $$\mathbf{v}_t + \mathbf{v}(\nabla \mathbf{v}) = -\rho^{-1}\nabla p + \mathbf{g} \tag{3.5}$$
  Here **g** is the gravity force vector and p the pressure.
- A velocity potential ϕ exist thanks to the previous assumption of irrotational flow
  $$\mathbf{v} = \nabla \phi \quad in \quad W \tag{3.6}$$
- From equation (3.4) and (3.6) is possible to obtain the Laplace equation
  $$\nabla^2 \phi = 0 \quad in \quad W \tag{3.7}$$
- From equation (3.5) and (3.6) is possible to obtain the Bernoulli's equation
  $$\phi_t + \frac{|\nabla \phi|^2}{2} = -\frac{p}{\rho} - g(z - z_0) + \frac{p_0}{\rho} \quad in \quad W \tag{3.8}$$
  p_0 is the atmospheric pressure and z the vertical coordinate.

Let η be the elevation of the surface at time t above the mean fluid surface level.Since η can be assumed small with respect to the water depth, a dynamic boundary condition on the free surface can be derived assuming $z = z_s$.

- Dynamic boundary condition on the surface $z = z_s$
  $$\eta = -\frac{\phi_t}{g} \tag{3.9}$$

The velocity of the fluid normal to the surface is equal to the normal velocity of the surface.

- kinematic boundary condition on the surface$z = z_s$
  $$\eta_t - z_t = \eta_t - \phi_z = 0 \tag{3.10}$$

- The boundary condition at the seabed $z = 0$

$$\phi_z = 0 \tag{3.11}$$

The solution of the governing equations and boundary conditions is integrated in the software Abaqus/Aqua, choosing the potential ϕ as a combination of two independent functions, one dependent on time and planar coordinate ad the other on the vertical coordinate. A Fourier series expansion, with respect to space and time is made. Finally the velocity and acceleration time histories of the fluid particles are obtained.

Dispersion Relation

The dispersion relation, which links the wavelength to the water depth is fundamental for engineering applications. The dispersion relation states that waves with a given frequency must have a certain wavelength.

$$L = \frac{gT^2}{2\pi} \tanh(\frac{2\pi d}{L}) \Leftrightarrow \omega^2 = kg \tanh(kd) \tag{3.12}$$

T, ω	are the wave period and frequency
L, k	are the wavelength and wave number
g	is the gravity constant
d	is the water depth

The speed of the crest of the wave as it moves along, called *phase velocity*, c_p, of a regular wave is defined as

$$c_p = \frac{L}{T} = \frac{\omega}{k} \tag{3.13}$$

Depending on the ratio between water depth and wavelength there are two particular cases.

Shallow Water
When $d/L < 0.05$, the water depth is much smaller than the wavelength. In this case $\tanh(kd)$ can be replaced with kd. Thus,

$$\omega = \pm\sqrt{gdk} \quad , \quad c_p = \sqrt{gd} \tag{3.14}$$

Deep water
When $d/L > 0.5$, the water depth is large compared to the wavelength. In this case $\tanh kd$ can be replaced with 1. Thus,

$$\omega = \pm\sqrt{gk} \quad , \quad c_p = \sqrt{\frac{g}{k}} \tag{3.15}$$

3.3.2 Morison Equation

Morison equation can be used to calculate wave actions when the cross-sectional dimensions are significantly smaller than the wave length. The Morison equation states that the fluid force is a superposition of a term in phase with the acceleration (inertia), and a term whose dominant component is in phase with the velocity of the flow (drag). The Morison equation is deterministic. In other words, it takes in to account the history of the flow and the frequency of flow oscillations by some coefficients.

C_d, C_m	are the drag and inertia coefficients, $C_m = C_a + 1$
C_a	is the added mass coefficient
x	is the body displacement

The Morison equation for a fixed cylinder with area A and diameter D is,

$$F(t) = \rho C_m A \dot{v} + \frac{1}{2}\rho C_d D v^2 \tag{3.16}$$

Considering the motion of the object the equation can be written as in [Perotti et al., 2013],

$$F(t) = \frac{1}{2} C_d \rho D |v - \dot{x}|(v - \dot{x}) + C_m \rho A(\dot{v} - \ddot{x}) + \rho A \ddot{x} \tag{3.17}$$

The third term is the Froude-Krylov force which describes non viscous forces acting on a floating body in irregular waves.

The Morison inertia force for a fixed tube related to the wave frequency and amplitude can be written as [Olsen et al., 2016],

$$F_m = ((1 + C_a)\rho A \omega^2 e^{-kd})h \tag{3.18}$$

where ω is the wave angular frequency, and k is the wave number. The wave number is strictly related to the wave Dispersion Equation. The Morison drag force for a pipeline with fixed ends can be approximated to

$$F_D = \frac{1}{2}\rho_w C_D v^2 D \tag{3.19}$$

Shadow effects on the second tube

Considering the double submerged floating tube bridge configuration, one tube will partially protect the other from current loads. Shadow effects on the second tube can be calculated by Schlichting's wake formula using Blenvis approach with virtual origin 6 diameters in front of the first cylinder, [Reinertsen and Group, 2012].

$$\frac{v_2^2}{v^2} = 1 - 2 * 0.95 * \sqrt{\frac{C_d D}{CDBT + 6D}} \tag{3.20}$$

where CDBT is the Center Distance Between Tunnels, v_2 is the flow velocity in the shielded cylinder.

3.3.3 Jonswap Wave Spectrum Model

Jonswap Spectrum is one of the most studied and used wave spectrum models [Silva, 2015].

$$S(\omega) = \alpha\omega^{-5}e^{-\frac{5}{4}(\frac{\omega}{\omega_p})^{-4}}\gamma^{\delta} \tag{3.21}$$

$$\delta = e^{-\frac{(\omega-\omega_p)^2}{2\sigma_0^2\omega_p^2}} \tag{3.22}$$

$$\alpha = \frac{5}{16}(1-0.287ln\gamma)H_s^2\omega_p^4 \tag{3.23}$$

$$\sigma_0 = \begin{Bmatrix} 0.07, & if \quad \omega < \omega_p \\ 0.09, & if \quad \omega > \omega_p \end{Bmatrix} \tag{3.24}$$

$$\gamma = \begin{Bmatrix} 5, & if & \phi \leq 3.6 \\ e^{5.75-1.15\phi}, & if & 3.6 < \phi < 5 \\ 1, & if & \phi \geq 5 \end{Bmatrix} ; \phi = \frac{T_p}{\sqrt{H_s}} \tag{3.25}$$

Where,

γ^{δ},σ_0	are the peak enhancement factor and the width of the peak region;
ω_p,T_p	are the peak wave frequency and period;
Hs	is the significant wave height.

The value of γ can be taken equal to 5 for swell waves. Based on a sensitivity study, the wave directions shall be chosen to give the highest dynamic response of the tube bridge [Olsen et al., 2016]. In abaqus the waves are modelled as a single wave event using either the Airy wave theory or the 5^{th} order Stokes theory.

3.3.4 Wave Directionality

The effect of wave directionality and wave spreading is introduced in from of a reduction factor. Many SFT models in this thesis have a parabolic shape, therefore, the relative angle between the wave direction and the tunnel axis is not constant, and a reduction of the significant flow should be applied. This is useful in order to obtain a two dimensional description of the sea state.

The reduction factor given by [Veritas, 2002] is

$$R_D = \sqrt{\int_{-pi/2}^{pi/2} w(\beta)sin^2(\Theta_{rel}-\beta)d\beta} \tag{3.26}$$

The energy directional function is given by a frequency independent cosine function is

$$w(\beta) = \frac{\Gamma(1+s/2)}{\sqrt{\pi}\Gamma(0.5+s/2)} cos^s(\beta) \quad for \quad |\beta| < \frac{\pi}{2} \tag{3.27}$$

Γ is the gamma function and it is defined as

$$\Gamma(s) = \int_0^\infty t^{s-1} e^{-t} dt \tag{3.28}$$

The spreading parameter s is a function of the sea state. For regular sea states ranges between 2 and 4 for wind waves, and between 6 and 8 for swells. The graphs for the directional function, and reduction factor with s values of interest for this thesis project are reported in Figs. 3.1 and 3.2.

Θ_{rel} is the relative direction between wave direction and tunnel axis.
β is the wave direction

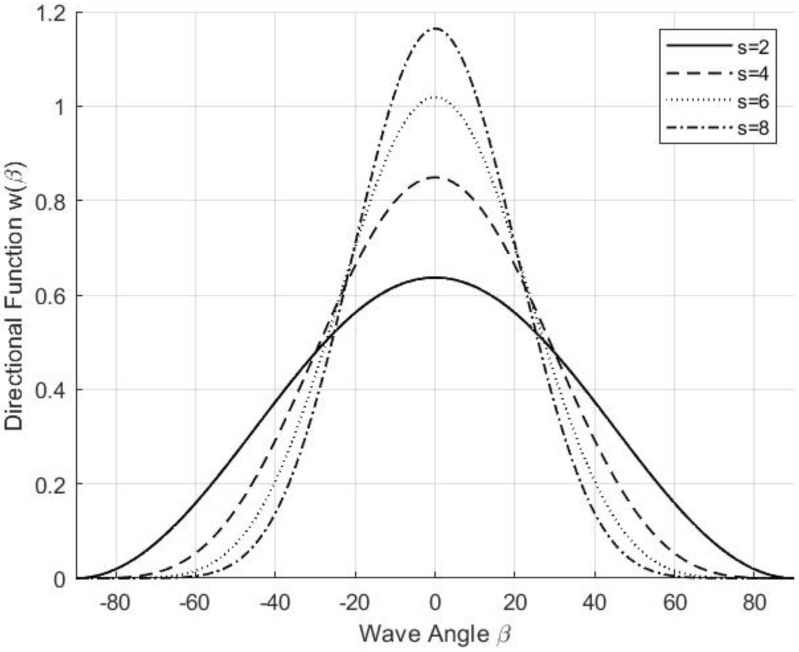

Figure 3.1: Wave energy spreading function

3.3.5 Tidal Loads

The effects on tidal load on tether stabilize SFT are negligible compared to the other actions. Tidal loads are more important for the pontoon stabilized SFT where there are forces induced by the changing of water level at the pontoons, [Olsen et al., 2016].

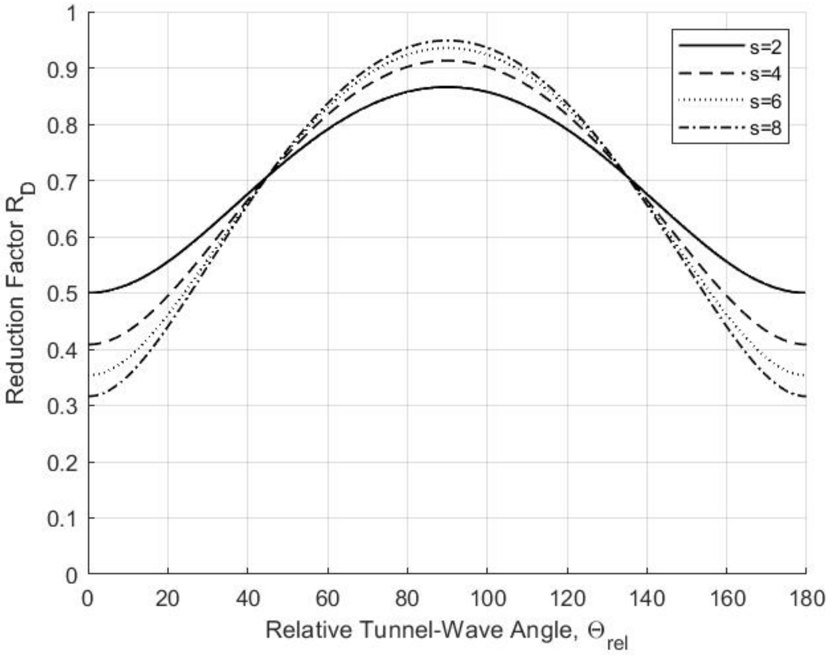

Figure 3.2: Reduction Factor due to wave directionality and spreading

3.4 Modal Analysis

Modal analysis is the theory dealing with the dynamics of structure described by modes. Once known the mass and stiffness matrices, it is possible to find the natural frequencies of the structure. The natural modes of vibration are inherent to a dynamic system and are determined completely by its physical properties (mass,stiffness,damping) and their spatial distributions.

Each natural mode is described in terms of its natural frequency, the modal damping factor, and the mode shape. The natural frequencies are important to make sure that resonance condition does not happen during the analysis. This means that the frequency of the structure should be different from the frequency of an expected load condition. If resonance occurs the structure may experience serious damage due to large displacements.

When dealing with the modal analysis of a multi degree of freedom system the equation of motion become :

$$[M]\{\ddot{x}\} + [C]\{\dot{x}\} + [K]\{x\} = \{0\} \tag{3.29}$$

Here, $[M]$ is the mass matrix, $[C]$ is the damping matix and $[K]$ is the stiffness matrix. Generally, it does not exist a set of principal coordinates, which uncouple equation (3.29). This because the matrix C can not be diagonalized as the other two matrices. One proposal to overcome this issue is indicated in *Theory of Sound* written by Rayleigh, where the damping matrix is assumed proportional to the mass and stiffness matrices. A method to estimate the proportionality coefficients for large systems is reported in section 3.4.2. In some cases due to large displacement effect, also the stiffness matrix may not be positive definite or symmetric.

3.4.1 Modal Analysis in Abaqus - Lanczos Eigensolver

The modal analysis for undamped multi degree of freedom systems is applicable for dynamic structures when damping is negligible [He and FU, 2001]. SFTs structures have generally low damping, for instance a damping ratio of 0.008 was assumed in [Olsen et al., 2016] and in [Reinertsen and Group, 2012]. Therefore neglecting the damping matrix [C] and assuming the stiffness matrix [K] positive definite, the eingenvalue problem can be written as:

$$([K] - \omega_i^2[M])\{\Phi_i\} = \{0\} \tag{3.30}$$

Where ω is the circular frequency and $\{\Phi\}$ the eigenvector.

Modal analysis in finite element programs is generally related to a large number of degree of freedoms. Therefore, stiffness and mass matrices are very large and often sparse. Only few eigenpairs are required and in this case iterative solvers such as Lanczos tend to be the most efficient. The Lanczos method is well suited to the task of computing a few eigenvalues and eigenvectors of a large symmetric matrix [Parlett and Scott, 1979]. Abaqus implemets together with Lanczos algorithm, the Householder metehod, which is used to reduce a general matrix to a symmetric tridiagonal matrix.

Modal participation factor

The degree of partecipation of its natural mode in the overall vibration is determined both by properties of the excitation source and by the mode shapes of the system [He and FU, 2001]. The effective mass participation analysis is performed in order to estimate how many relevant modes are needed to be calculated. The total number of modes extracted needs to include approximately 90% of the mass participation. In Abaqus the participation factors are defined for translational degree of freedom and rotational degree of freedom around the center of rotation. The generalize mass for the $i - mode$ (equation 3.31) and the participation factor (equation 3.32) are :

$$m_i = \{\Phi_i\}^t[M]\{\Phi_i\} \tag{3.31}$$

$$\Gamma_i = \frac{\{\Phi_i\}^t[M]\{T\}]}{m_i} \tag{3.32}$$

Where $\{T\}$ is he influence vector which represent the displacement of the masses considering a rigid body response in a defined direction. For instance, for an horizontal excitation $\{T\}$ is the unit vector. Finally the effective modal mass can be evaluated (equation3.33). Its is a useful parameter in order to understand how the mass is distributed in the modes.

$$m_{i,eff} = m_i\Gamma_i^2 \tag{3.33}$$

In other words the effective mass of the $i - mode$ is the fraction of the total static mass that can be attributed to this mode (static inertia for rotation modes).

3.4.2 Simplified Method for Eigenfrequencies

In the early stage of the design it might be necessary to carry out a modal analysis by an analytical method. The simplified model can be also useful as a comparison with the FEM results. This method is limited to a straight tunnel configuration. The method explained here can be found in [Xiang et al., 2017], here is slightly adapted for a tether configuration. The assumed shape function for mode n and variable of the length x is

$$\phi(n,x) = e^{-\beta(n)x} - cos(\beta(n)x) + \alpha(n)sin(\beta(n)x) - (-1)^n \frac{e^{\beta(n)(x-L)} - e^{-\beta(n)(x+L)}}{1 + e^{-2k(n)}} \tag{3.34}$$

$$\alpha(n) = \frac{sin(k(n))}{(-1)^n - cos(k(n))} \tag{3.35}$$

$$k(n) = (n+0.5)\pi - \frac{(-1)^n}{cosh((n+0.5)pi)} \tag{3.36}$$

$$\beta(n) = \frac{k(n)}{L} \tag{3.37}$$

The modal masses are calculated for each shape function and the can be divided in sway and heave direction

$$M_s(n) = \int_0^L (m_{tunnel}(x) + m_a(x))\phi(x,n)^2 dx + (m_{tether} + m_a)\frac{1}{3}\sum_i \phi(j_i,n)^2 \tag{3.38}$$

$$M_h(n) = \int_0^L (m_{tunnel}(x) + m_a(x))\phi(x,n)^2 dx + (m_{tether} + m_a)\sum_i \phi(j_i,n)^2 \tag{3.39}$$

m_{tunnel} and m_{tether} are respectively the total masses of tunnel and tether per unit length, m_a is the added mass due to the surrounding fluid. The added mass has to be calculated for the tunnel and the tethers, the equation is reported in (equation 3.44).

The modal stiffnesses for the sway and heave direction are

$$K_s(n) = \int_0^L EI_z(\frac{d^2\phi(x,n)}{d^2x})^2 dx + \sum_i \frac{T_i}{L_i}\phi(j_i,n)^2 \tag{3.40}$$

$$K_h(n) = \int_0^L EI_y(\frac{d^2\phi(x,n)}{d^2x})^2 dx + k_{tether}\sum_i \phi(j_i,n)^2 \tag{3.41}$$

i	is the tether number
j	is the the tether location
T	is the tether tension
L_i	is the length of the i^{th} tether
k_{tether}	is the tether axial stiffness

3.4.3 Added Mass

For the case of bodies underwater, an additional effect from the fluid acting on the structure when formulating the system equation of motion must be considered. This added effect is called added mass (m_a), and generally is taken into account by a coefficient.
In physical sense, the added mass is the weight added to a system due to the fact than an accelerating body must move some volume of surrounding fluid with it as it moves.

For a simple system composed only by a point mass, a dashpot and a spring the equation of motion is

$$m\ddot{x} + c\dot{x} + kx = f(t) - m_a\ddot{x} \tag{3.42}$$

The natural frequency of the system is simply

$$\omega = \sqrt{\frac{k}{m + m_a}} \tag{3.43}$$

The hydrodynamic mass coefficient can only be determined by experiments. It depends on flow conditions around the structure, the structural shape, and the roughness of the structure. Values of the added mass coefficient (C_a), can be found in [Veritas, 2002]. The added mass for a cylinder is

$$m_a = C_a\rho * \frac{\pi}{4}D^2 \tag{3.44}$$

3.4.4 Damping Parameters

When the Rayleigh damping model is used, the damping matrix [C] of a structure is a linear combination of mass [M] and stiffness matrixes [K].

$$[C] = \alpha[M] + \beta[K] \tag{3.45}$$

where α and β represent the mass and the stiffness proportional damping coefficients.

$$\begin{Bmatrix} \alpha \\ \beta \end{Bmatrix} = \frac{2\omega_j\omega_i}{\omega_j^2 - \omega_i^2} \begin{pmatrix} \omega_j & -\omega_i \\ -\frac{1}{\omega_j} & \frac{1}{\omega_i} \end{pmatrix} \begin{Bmatrix} \xi_i \\ \xi_j \end{Bmatrix} \tag{3.46}$$

ξ_i,ξ_j are the damping ratios
ω_i,ω_j are the natural frequencies

The equation (3.46) can be simplified by assuming ξ_i=ξ_j.

$$\begin{Bmatrix} \alpha \\ \beta \end{Bmatrix} = \frac{2\xi}{\omega_j + \omega_i} \begin{Bmatrix} \omega_i \omega_j \\ 1 \end{Bmatrix} \tag{3.47}$$

For complex structures and structures with a high number of modes that contribute greatly to dynamic responses, difficulties in selecting two orders of reference frequencies to obtain reasonable Rayleigh damping coefficients α and β are encountered [Song and Su, 2017]. Therefore an other method is implemented for the Computation of Rayleigh Damping Coefficients for Large Systems [Chowdhury and Dasgupta, 2003].
The method is a steb by step method :

1. Select ξ_1
2. Select ξ_m, where m is the number of significant modes
3. Obtain ξ_i by linear interpolation for intermediate modes

$$\xi_i = \frac{\xi_m - \xi_1}{\omega_m - \omega_1}(\omega_i - \omega_1) + \xi_1, 1 < i < m \tag{3.48}$$

4. Obtain ξ_i by linear interpolation for modes grater than m

$$\xi_i = \frac{\xi_m - \xi_1}{\omega_m - \omega_1}(\omega_m + 1 - \omega_m) + \xi_m, m < i < 2.5m \tag{3.49}$$

5. In the equation (3.46) set i=m and j=1 and evaluate β
6. Obtain α from β

$$\alpha = 2\xi_1\omega_1 - \beta\omega_1^2 \tag{3.50}$$

7. Repeat points 5 and 6 by setting i=2.5m
8. Calculate the average of the values of α and β obtained

At the end of the step procedure can be obtain 4 different curves for the damping ratio. Three of them are obtained by the equation (3.51) using the 3 different sets of values of α and β. And the last one is obtained by the (3.48).

$$\xi_i = \frac{\alpha}{2\omega_i} + \frac{\beta\omega_i}{2} \tag{3.51}$$

3.5 Dynamic Analysis

Dynamic loads are defined as time-varying loads whose magnitude, direction of application , or position vary continuously with time. Therefore, also the structural response varies continuously with time. Two basic approaches are possible in order to evaluate the response of structure to dynamic loads, the deterministic and non-deterministic approach.

In deterministic approach, the time history of the loading is fully known with highly varying and irregular load magnitude, loading can be classified as prescribed dynamic loading. In non-deterministic approach, the time history of loading is not completely known but can be defined in statistical sense, the loading is termed as random dynamic loading, [Chandrasekaran, 2018].

Deterministic analysis lead to displacement time history corresponding to the given load time history. Stress, strain and internal forces are derived from the established displacement configuration. In case of non-deterministic analyses, results obtained will provide statistical information of the displacements under the action of a statistically defined loading. Other aspects such as stress, strain, and internal forces shall be computed directly by similar independent non-deterministic analyses rather than from deriving them from the displacement results [Chandrasekaran, 2018].

In a deterministic analysis the waves can be modelled with different wave theories such as Airy wave, Stockes waves Cnoidal waves or Fourier series waves [Xiang and ZHENG, 2013]. In a non-deterministic analysis, the sea state, which is typically 3h hours, is assumed as zero-mean ergodic Gaussian process. This can be defined completely by a wave spectrum. For north sea, Jonswap or Torsethaugen wave spectrums are recommended.

In a deterministic approach the solution of the problem (structural response) is generally determined by analytical solutions or numerical solution. Analytical solutions are limited to simple structure, while numerical analysis is much more comprehensive. There are also semi-anaythical solutions, where the equation of motion is transformed analytically to a relatively simple form and then numerical methods are used for its integration [Bajer and Dyniewicz, 2012]. However, semi-analytical solutions are not versatile and thus they are unsuitable for engineering practice. The equation of motion of a multi degree of freedom damped system is :

$$[M]\{\ddot{x}\} + [C]\{\dot{x}\} + [K]\{x\} = \{F\} \tag{3.52}$$

Where $\{F\}$ is dependent on the structure-fluid interaction theory chosen. The equation of motion is often solved in finite element analysis by Newmark method, Bossak method or Hilbert, Hughes and Taylor method.

Non-deterministic structural response analysis is generally based on a 3 hours sea state, for a 50 year return period, probabilistic properties.

3.5.1 Discrete Fourier Transform

The Fourier transform is an integral transform with many practical applications, it convert a signal from the time-domain to the frequency-domain.

If $x(t)$ is a periodic funtion of time t, with period T, then the complex form of the Fourier transform can be written as:

$$X(\omega) = \frac{1}{2\pi}\int_{-\infty}^{\infty} x(t)e^{-i\omega t}dt \tag{3.53}$$

Very often a function x(t) is given only in terms of values at finitely many points, and one is interested in extending Fourier analysis to this case. In this situation, dealing with sampled values rather than functions, it is possible to replace the Fourier transform by the so-called discrete Fourier transform (DFT), [Erwin Kreiszyg, 2008].

Considering that equally spaced samples are available and represented by discrete time series $x_r = x(t_r)$, $r = 0, 1, 2, ..., (N - 1)$, where N is the number of samples. In this case the integral may be replaced approximately by the summation

$$X_k = \frac{1}{N}\sum_{r=0}^{N-1} x_r e^{-i(2\pi kr/N)} \tag{3.54}$$

In the dynamic analysis computed by FEM, $N = \frac{T}{\Delta}$, where T is the period of analysis and Δ the sampling interval. In order to avoid aliasing effects it is important to remember that the coefficient X_k, calculated by the DFT are correct only for frequencies up to $\frac{\pi}{\Delta}$, [Newland, 2005a].

3.5.2 Hilbert, Hughes and Taylor method

The Hilbert-Hughes-Taylor (HH-T) time integration is an extension of the Newmark numerical method. Newmark method is usually chosen for integrating differential equations of motion [Bajer and Dyniewicz, 2012]. Newmark method was modified to HH-T method in order to improve some properties. HH-T is an implicit time integration operator, which means that the operator matrix must be inverted and a set of non linear dynamic equilibrium equations must be solved at each time increment. The advantage is the unconditional stability for linear systems.

In HH-T method is controllable the numerical damping. Generally the form that takes has a rapid growth rate at high frequencies, and a slow growth rate at low frequencies. The HH-T algorithm is the following :

$$\begin{aligned} u_{n+1} &= u_n + hv_n + h^2(1/2-\beta)a_n + h^2\beta a_{n+1} \\ v_{n+1} &= v_n + h(1-\gamma)a_n + h\gamma a_{n+1} \\ Ma_{n+1} + Cv_{i+1} + (1+\alpha)Ku_{n+1} - \alpha Ku_n &= F_{n+1} \end{aligned} \tag{3.55}$$

$u(t)$	is the displacement vector
$v(t)$	is the velocity vector
$a(t)$	is the acceleration vector

HH-T algorithm is very sensitive to the parameters chosen and it is stable just for a very narrow range of values of β, γ and α, in the case of $\alpha = 0$, it coincide with the Newmark method.

$$\begin{aligned} -\frac{1}{2} \leq \alpha &\leq 0 \\ \beta &> 0 \\ \gamma &\geq \frac{1}{2} \end{aligned} \tag{3.56}$$

The numerical damping is related to the parameter α. The solution of the algorithm is straightforward and can be found in [Bajer and Dyniewicz, 2012].

Chapter 4

Conceptual Design

The essence of conceptual design is to provide a simple, effective and safe operating method to activate and direct the drafts design process. This should be able to produce a reasonable number of alternative solutions that meet the boundary conditions and can be subjected to subsequent optimization, thus producing the final choice.

Professor Rosati Gianpaolo

4.1 Geometrical Properties

The tunnel cross-section is based on the Bjørnafjord project [Olsen et al., 2016], however in this thesis project a single tube is considered. The tube is made of reinforced concrete and it has a circular shape. A traffic deck and three separate compartments below the traffic deck are the main room. The three compartments below have different functions. The middle one is dedicated to bicycle lane and service, while the other compartments contain water ballast.

A lay by lane of 30 meters is required every 500 meters. A lay by is a transverse extension of the driving lane, required for parking during an emergency stop. The tunnel has therefore two different internal cross sectional dimensions, one in the presence of the lay by and the other in the remaining part. The transition length between one cross section and the other is of 30 meters. Moreover, a larger outer diameter is often required at the end connections due to the large shear and bending moments acting.

In the present phase the moment of inertia are considered as the ones of a perfect cylinder, neglecting the resistance of the internal deck. This is done for the sake of simplicity, in order to have an easy comparison in case of tunnels with different diameters.

The tunnel span L chosen in this thesis project is $L = 500m$. This choice is made in order to analyse a SFT that could be adopted for more common crossing length, since the majority of crossing does not exceed 500m. Being the span smaller than the minimum lay

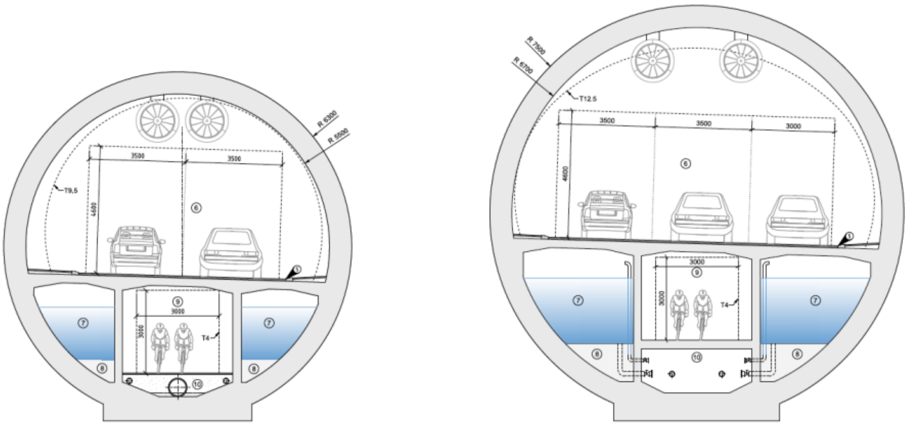

Figure 4.1: Tunnel general cross-section (left) and lay by cross-section (right), [Olsen et al., 2016]

Table 4.1: Properties of tunnel cross-section

Parameter	Unit	General section	Lay by section
Outer diameter D$_e$	m	12.6	15.0
Inner diameter D$_i$	m	11.0	13.4
Cross sectional area A$_c$	m^2	37.3	46.7
Outer area A	m^2	124.7	176.7
Moment of inertia I	m^4	519	902
Ballast compartment area	m^2	13.5	26.7
Tunnel depth	m	40	41.2

by distance, a lay by is not considered in this phase. The main goal of this chapter is to find, with a simple model, an advantageous SFT orientation. The tunnel depth reported in Table 4.1 is relative the the upper part of the cross-section.

4.1.1 Tethers

The tether typology adopted is the one reported in Fig. 2.6. The purpose of the tethers is to stabilize the the net buoyancy force, provide vertical and horizontal stiffness to the SFT. They work as a tie connection between tunnel and sea bed. The advantages of having a hollow cross-section for theters are, in agreement with [Perotti et al., 2013]:

- reach a straight configuration under the combined action of weight and buoyancy;
- bear some compressive load, while standard cables cannot.

One of the key parameters in tethers design is to have a sufficient initial pretension. In this way time varying loads and operational loads will not lead to slack in the tethers. Generally, traffic load is the governing load for tether slack criterion, according to [Olsen et al., 2016]. Moreover, tethers deserve special attention in terms of fatigue limit state, since they are steel element submerged in water, under cycling loading. Tether dimensions are mainly governed by axial stiffness. The tether is assumed for sake of simplicity as a 3 layer composite cross section. Two boundary steel layer and one concrete layer in between as in Fig. 4.2.

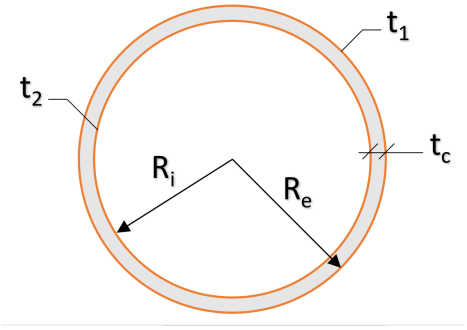

Figure 4.2: Geometrical properties of tethers

t_1, t_2	are the thicknesses of the external and internal steel layers
t_c	is the thickness of the reinforced concrete layer
R_e, R_i	are the external and internal radius

For the preliminary design phase the geometrical properties reported in table are assumed. The values were chosen in order to have a null buoyancy weight ratio of the tethers, avoiding so the catenary effect.

Table 4.2: Preliminary geometrical properties of tethers

Parameter	Unit	Value
$\mathrm{t}_1 = t_2$	mm	12
t_c	mm	44
R_e	mm	1029
R_i	mm	961
Area	mm^2	4151
External area	mm^2	$332.6*10^4$

4.2 Structural Requirements

In this thesis project are considered only structural requirement regarding the global design of the tunnel. Since no specific requirements are defined for SFTs, the same requirements that has been used in the technical report of the Bjørnafjord crossing [Olsen et al., 2016] are used. The requirements that will be considered are regarding deflections, acceleration and water tightness of the cross section.

The Norwegian public road administration has advised the limiting values for deflections reported in Table 4.3.

Table 4.3: Deflection limit state for SFTs

Alignment	Static loads	Dynamic loads
Horizontal	δ_{max} <L/200	δ_{max} <L/350
Vertical	δ_{max} <L/350	δ_{max} <L/350

The parameter L varies between the horizontal and the vertical deflection. For deflections in the horizontal direction, the parameter L can be taken as the distance between the landfalls. For the vertical direction L can be assumed equal to the distance between the supports, which means the distance between the tether connections. The parameter δ_{max} is the maximum deflection in the direction considered.

Accelerations and vibrations are evaluated with respect to user comfort. Ensuring serviceability is central to the design of bridges containing a pedestrian lines, which is present in the SFT cross section selected. The design in terms of maximum allowable accelerations is often governed by the serviceability limit state for pedestrian use [Dey and Walbridge, 2018]. An high acceleration can cause discomfort and, in particular an user could be sea sick in case of high acceleration. Horizontal, high acceleration causes unbalance of pedestrian equilibrium, while vertical oscillation rarely hinders walking. For large, slender and complex structures, the pedestrian structure interaction is complex. Here just comfort criteria regarding accelerations are considered and listed in Table 4.4.

Table 4.4: Maximum acceleration limit state to ensure pedestrian comfort

Direction	$a_{max}(m/s^2)$
Horizontal	0.3
Vertical	0.5

The bridge tube should ensure water tightness during operation and temporary conditions. The design criteria for serviceability limit state is zero crack width, and some limitations on the tensile zone. In particular the minimum depth of compression zone has to be larges than 0.25 times the cross section height [Olsen et al., 2016]. Moreover, in ultimate limit state design the reinforcement and the post tensioning cables must be limited to the elastic range.

The structural requirements for tethers, in this thesis project, are to avoid compression and to not overcome the yield limit of the steel. Compression in tethers should be avoided in order to not risk tethers slacking. For the sake of the structural model definition, materials are assumed to behave in elastic range, therefore the tethers shall not enter in plastic domain.

4.3 Materials

The materials used for the main tube are concrete grade C45/55 and reinforcing bars B500. For the tethers is used a composite cross-section made of concrete grade C45/55, reinforcing bars and steel grade S 460 NH.

Table 4.5: Material Properties, characteristic values

Parameter	Unit	Concrete C45/55	B500	S 460 NH
Elastic modulus E	GPa	36.28	210	210
Poisson ratio ν	/	0.2	0.3	0.3
Density ρ	kg/m^3	2500	7850	7850
Shear modulus G	GPa	15.12	80.77	80.77
Tensile strength f$_{ctm}$	MPa	3.8	/	560
Compressive strength f$_{ck}$	MPa	45	/	/
Yield strength f$_{yk}$	MPa	/	500	460

$$E_{concrete} = 22[f_{cm}/10]^{0.3} = 36.38GPa, \quad f_{cm} = 53MPa \tag{4.1}$$

The composite tunnel section is treated as an equivalent homogeneous one, having elastic modulus equal to the one of concrete $E_{concrete}$. The steel material S 460 NH used for tethers is suitable for high strength requirements, and it has good resistance to fatigue. The tethers are made of a composition of two materials, concrete C45/55 and steel S 460 NH. They will be considered as an equivalent material, adopting the principle of equivalent strain. Referring to the tether under tensile forces, and calling ε the strain, can be assumed

$$\varepsilon_{steel} = \varepsilon_{concrete} = \varepsilon_{equivalent} \tag{4.2}$$

Defining f as the steel volume fraction, it can be written the so called rule of mixture in equations (4.3),(4.4).

$$E_1 = fE_{steel} + (1 - f)E_{concrete} \tag{4.3}$$

$$\nu_{12} = f\nu_{steel} + (1 - f)\nu_{concrete} \tag{4.4}$$

The equivalent elastic modulus and Poisson's ratio are a good approximation for the tether loaded on the axial direction. If the stress is applied in the direction transverse to the fibers, the slab model (equation 4.5) can be applied with the steel and concrete material acting in series. In this case the stress level in the steel and concrete can be assumed equal (an idealization).

$$\frac{1}{E_2} = \frac{f}{E_{steel}} + \frac{1-f}{E_{concrete}} \tag{4.5}$$

E_1,E_2 are respectively the equivalent longitudinal and transverse elastic modulus of the composite tether cross section. Values for different volume fraction of steel are plotted in Fig. 4.3. Once determined the elastic constants of the material, the behaviour of the composite section is completely determined for any stress direction, inclined with respect to the axes of symmetry of the material.

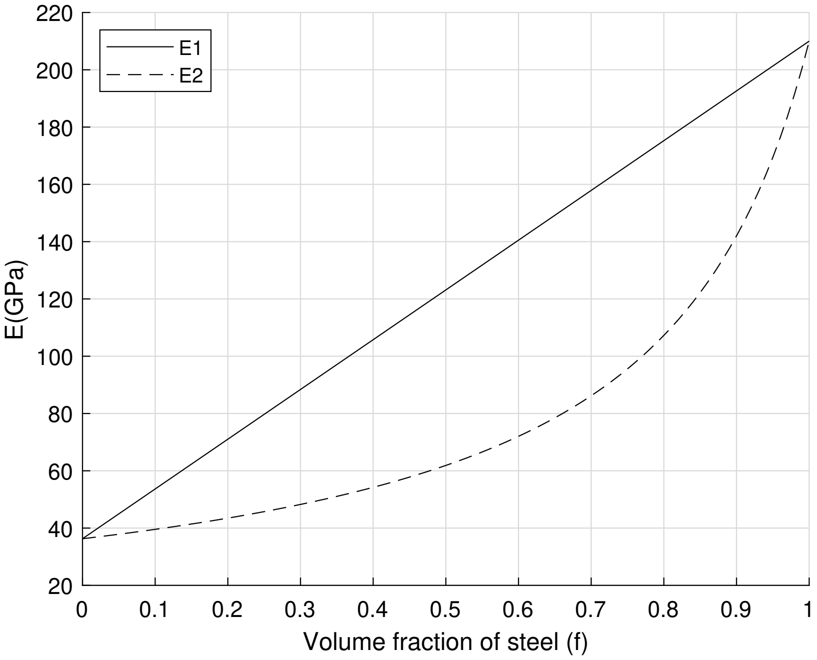

Figure 4.3: Equivalent longitudinal and transverse elastic modulus of tethers, varying the steel volume fraction

4.4 Environmental Condition

For the present chapter, only the major governing loads are considered. The main objective is to define the principal tunnel characteristics. Hence, only the operation phase during the maximum wave condition is treated. The sea bed elevation, d, is assumed constant and equal to 200 m.

4.4.1 Sea States

The significant wave height and corresponding wave period are reported in Table 4.6. The current is assumed constant along the tunnel length, even though, the current is usually stronger in the middle part of the tunnel. The wave and current direction are chosen in order to reproduce the most unfavorable loading condition. Therefore, a direction perpendicular to the tunnel in the central part is considered. Other useful parameters are reported in the table 4.7, theory and formulas can be found in the chapter 3. From the sea state conditions designs values are calculated as suggested in [Olsen et al., 2016]. The maximum individual wave event modelled as a regular Airy wave can be taken as $H_{max} = 1.9H_s$, with corresponding wave period $T_{max} = 0.9T_p$.

Table 4.6: Sea state conditions

Waves	Significant Period T_p	Significant Height H_s
Wind	5.5 - 5.5 - 7.5 - 8.5	1.9 - 2 - 2.4 - 2.8
Swell	17	0.7 - 1.1 - 2.3 - 3

The wave length is calculated with the formula (3.12), using an iterative method, implemented in Excel. The Airy wave theory is justified when the Ursell's number, (3.2), is much smaller than 1. This is fulfilled for both the wind waves and the swell waves.

Table 4.7: Sea state design values adopted in the conceptual design phase

Parameter	Unit	Value
Swell waves height $H_{s,max}$	m	3.42
Wind waves height $H_{w,max}$	m	4.37
Swell wave period $T_{s,max}$	s	15.3
Wind waves period $T_{w,max}$	s	6.3
Swell waves length L_s	m	364.6
Wind waves length L_w	m	61.9
Current velocity v	m/s	1
Ursell parameter swell waves		0.057
Ursell parameter wind waves		0.002

It is possible to notice that the deep water assumption, (3.15), can be made for both wind and swell waves. In this design phase an average height and period have been chosen, the height have been then multiplied for 1.9 and the period for 0.9.
The reduction factor, relative to the wave directionality (3.3.4), is assumed equal to 1 in the preliminary design phase.
The Jonswap spectrum for the sea state conditions in Table 4.6, is reported in Fig. 4.4.

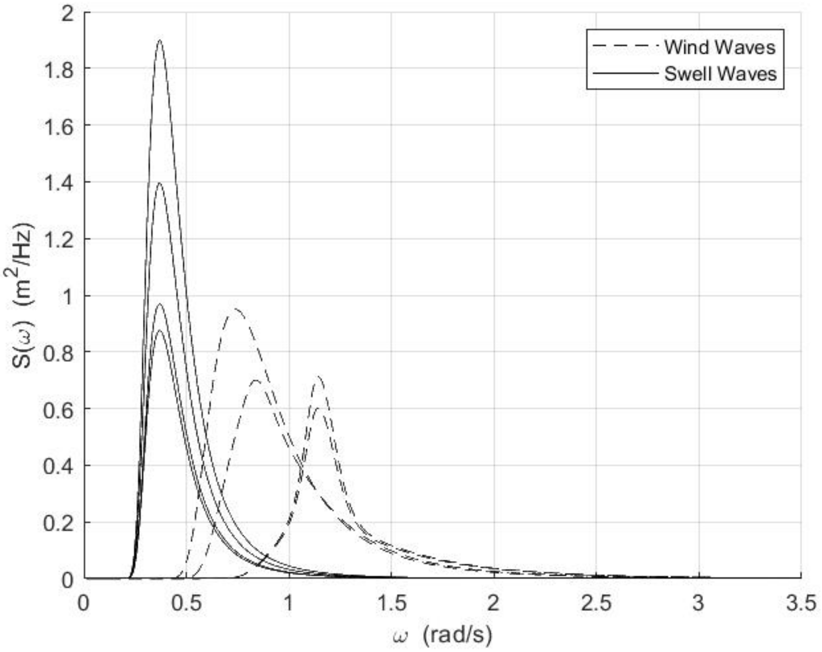

Figure 4.4: Jonswap Spectrum

4.4.2 Buoyancy and Dead Loads

In this initial phase the Submerged Floating Tunnel is designed with a BWR of 1.25, which is related to the weight of the cylinder plus the weight of the water ballast. Typically the BWR can be adjusted varying the water ballast, the tunnel diameter, and adopting light weight materials. The tunnel net force will therefore point upward, as shown in Fig. 4.5. The net buoyancy must be sufficient to provide pretension in the tethers for all loading conditions.

In order to guarantee watertightness of the tunnel, a longitudinal and hoop prestressing is considered. The pre-stress amplitude is chosen in agreement with [Olsen et al., 2016],

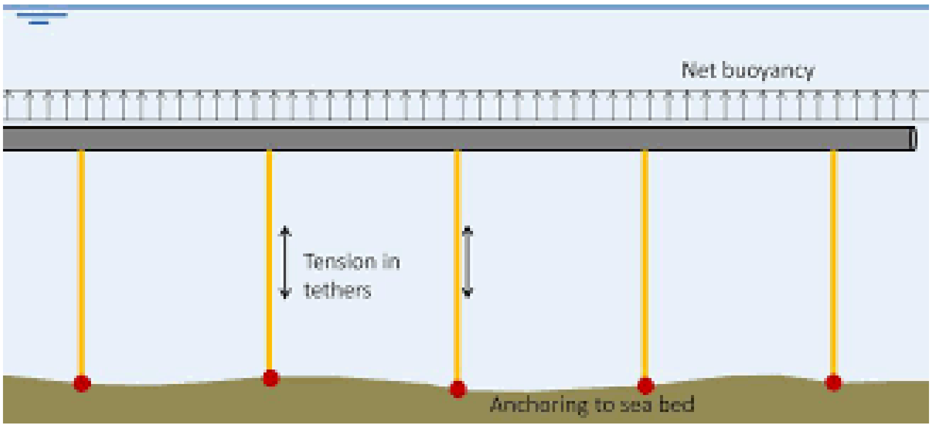

Figure 4.5: Net Buoyancy Load [Olsen et al., 2016]

Table 4.8: Self-weights

Load description	Unit	General Section	Lay by section
Concrete pipe weight	kN/m	-811	-875
Asphalt	kN/m	-19	-28.5
Permanent equipment	kN/m	-200	-200
Water ballast	kN/m	-146	-171.3
Buoyancy	kN/m	1253	1776
Buoyancy weight ratio		1.25	1.25
Net force q	kN/m	252	252

where the minimum prestressing level required for watertightness is indicted. The hoop prestress level is governed by explosion loads, whereas the longitudinal prestress is controllled by strain limitations. It is request that the tunnel cross-section remains fully compressed, as tensile forces may generate significant cracks in the concrete, allowing penetration of water.

The prestressing level required should be calculated carefully for each segment of the tunnel, however in this thesis project an average value of 10 MPa is chosen for the longitudinal direction. The presstressing will not be considered in the preliminary analithical analysis.

4.4.3 Wave and Current Forces

In general wave induced loads on tube have contributions from inertia loads and drag loads. Inertia forces are mainly due to pressure gradients and unsteady flow, while drag forces are due to flow separation. For the parameters reported in Tables 4.1 and 4.7, are illustrated in Fig. 4.6 the wave force regime for the SFT subjected to swell and wind waves. It results in Fig. 4.6 that, for both the wave load conditions, inertial forces are predominant and the Morrison equation is applicable.

Values of added mass coefficient (C_a) and drag coefficient (C_d) can be found in ([Veritas, 2002]), and they are equal to

$$C_a = 1 \qquad C_d = 1 \tag{4.6}$$

The Morison inertia force for a pipeline with fixed ends written in equation (3.18) is

$$F_m, swellwaves = 75.29kN/m \tag{4.7}$$

$$F_m, windwaves = 68.68kN/m \tag{4.8}$$

The Morison drag force equation (F_D) for a pipeline with fixed end is reported in equation (3.19) and it results,

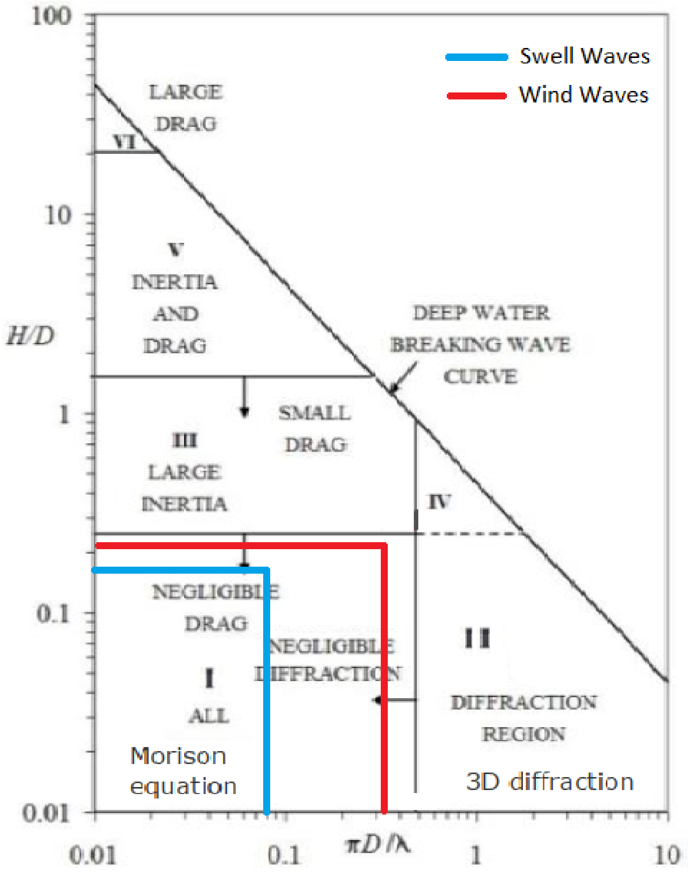

Figure 4.6: Wave force regimes related to the general section for wind and swell waves, [Olsen et al., 2016]

$$F_D = 6.48kN/m \tag{4.9}$$

It is possible to notice, in agreement with Fig. 4.6, that the inertial forces are predominant with respect to the drag force. The numerical calculations can be found in (A.1).

4.5 Alignment of SFTs

From the principle it appeared extremely important the decision of the tunnel orientation. Referring to Chapter 2, in the past years several horizontal alignments have been studied or considered. According to [Olsen et al., 2016] an arch shape reduces the maximal translation in mode 1, while an S-shape reduce the response in mode 4. This was found to give promising results and limited dynamic response in high swell conditions. However, an S-shape has a more complicate building process.

Generally, an arch shape is more efficient on carrying loads than a straight beam configuration. Moreover, thermal deformations in arch configurations produces lower axial forces than in straight beams. In order to understand the static behaviour of the SFT, varying the tunnel orientation, some hand calculations have been redacted using principle of virtual work and theory of curved beams.

4.5.1 Vertical Alignment

The vertical alignment of a SFT can be either straight or curved. All the previous projects found regarding SFTs have adopted a straight configuration. SFTs anchored by tethers, are subjected to high vertical distributed forces, especially when increasing the buoyancy weight ratio. Considering a SFTs design for road transport a maximum longitudinal slope of 5% can be adopted.

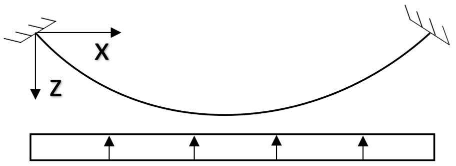

Figure 4.7: Vertical alignment scheme

Referring to Fig. 4.7, a parabolic shape is chosen and the $z(x, f)$ coordinate is described as

$$z(x) = 4f[\frac{x}{L} - (\frac{x}{L})^2] \tag{4.10}$$

The raise of the tunnel f relative to a 5% longitudinal slope, and a length $L = 500m$, is equal to $f = 6.25m$. The system in Fig. 4.7 is 3 times redundant. Using the concept of compatibility of displacement, the indeterminate structure can be split up into a primary and reactant structures. Thanks to symmetry an equivalent structure 2 times redundant can be founded. Assuming linear elastic materials, and valid the linear superposition of effects, the forces diagrams can be written as in equations (4.11),(4.12),(4.13).

$$M = M_0 + x_1 M_1 + x_2 M_2 \tag{4.11}$$

$$S = S_0 + x_1 S_1 + x_2 S_2 \tag{4.12}$$

$$N = N_0 + x_1 N_1 + x_2 N_2 \tag{4.13}$$

The subscript 0 refers to the primary structure force system while the subscripts $1, 2$ refer to the unit reactant force system. The internal forces are founded by imposing equilibrium, while the multipliers x_1, x_2 are founded by applying two times the principle of virtual work, equation (4.14).

$$\int_L (M_{1,2}\frac{M}{EI} + T_{1,2}\frac{T}{GA} + N_{1,2}\frac{N}{EA})\frac{dx}{cos(\alpha)} \tag{4.14}$$

where α is the angle between the central line and the horizontal direction. The equations are solved by hand calculations, and the results are validated by a comparison with a finite element model on ABAQUS, as shown in Figs. 4.8a and 4.8b.

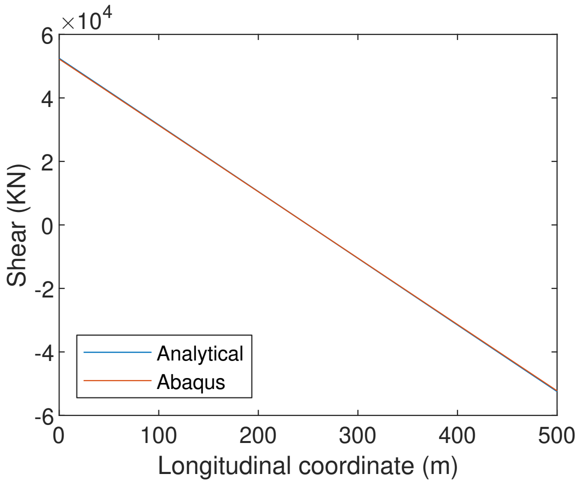

(a) Shear diagram

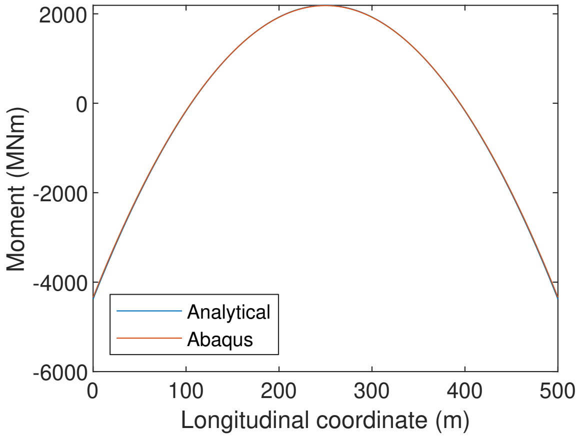

(b) Moment diagram

Figure 4.8: Comparison of shear (a) and bending moment (b) diagrams between the analytical and the 2D FEM solutions, considering only dead loads

The maximum absolute difference, between the finite element model and the analytical model is at the end sections. In particular there is a maximum difference of 0.46% in the shear diagram Fig. 4.8a and 0.9% in the bending moment diagram Fig. 4.8b.

Once, the analytical model has been validated, it can be used to find the distribution of shear and bending moment diagram, varying the arch rise. A static analysis is performed referring to the net force q reported in Table 4.8, and fixed end boundary conditions. Four configurations are compared, one straight configuration, three parabolic arches with a maximum slope of 5% ($f = 6.25m$), 4% ($f = 5m$) and 2.5% ($f = 3.125m$).

The maximum allowable slope in highway design is 5%. However, it is advisable in order to contain the emissions of polluting substances and fumes, to not exceed the 4% slope in tunnels [Ame, 2002]. The comparison in terms of shear diagram is reported in Fig. 4.9.

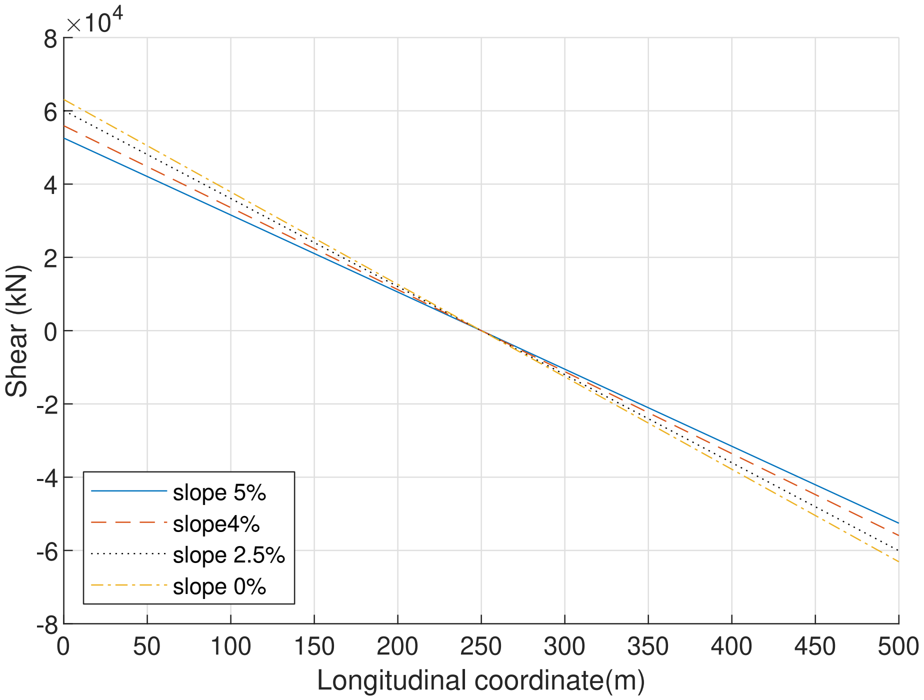

Figure 4.9: Shear distribution diagram (S_z), varying the maximum slope of the double clamped parabolic arch.

As expected, increasing the maximum allowable slope of the tunnel, and so the arch rise, lower shear resultant forces act on the tunnel. The shear diagram distribution is symmetric and the maximum absolute values are at the end sections of the arch. The shear amplitude at the end sections, regarding the straight tunnel configuration, is $6.31 \times 10^4 kN$. The maximum shear amplitude is reduced of 5% considering a slope of 2.5%. While, assuming a maximum slope of 4% and 5%, the reduction is respectively of 11% and 17%.

The bending moment distribution is symmetric, with the maximum positive bending moment at the mid span of the arch, while the maximum negative bending moment is at the end sections, Fig. 4.10. The maximum negative bending moment for the straight configuration is $-5257 MNm$. Making a comparison, at the end sections, between the straight configuration and the parabolic arch configurations, the bending moment amplitude decreases increasing the arch maximum slope. In particular there is a reduction of 4.7% with a slope of 2.5%, a reduction of 11.3% with a slope of 4% and the highest reduction of 16.6% with a slope of 5%.

The maximum positive bending moment for the straight configuration is $2629 MNm$. Observing the four curves Fig. 4.10, it can be noticed that increasing the rise of the arch the maximum positive bending moment decreases. In particular are registered reductions of 4.7%, 11.3% and 16.6%, relatively to slopes of 2.5%,4% and 5%. In percentage terms the

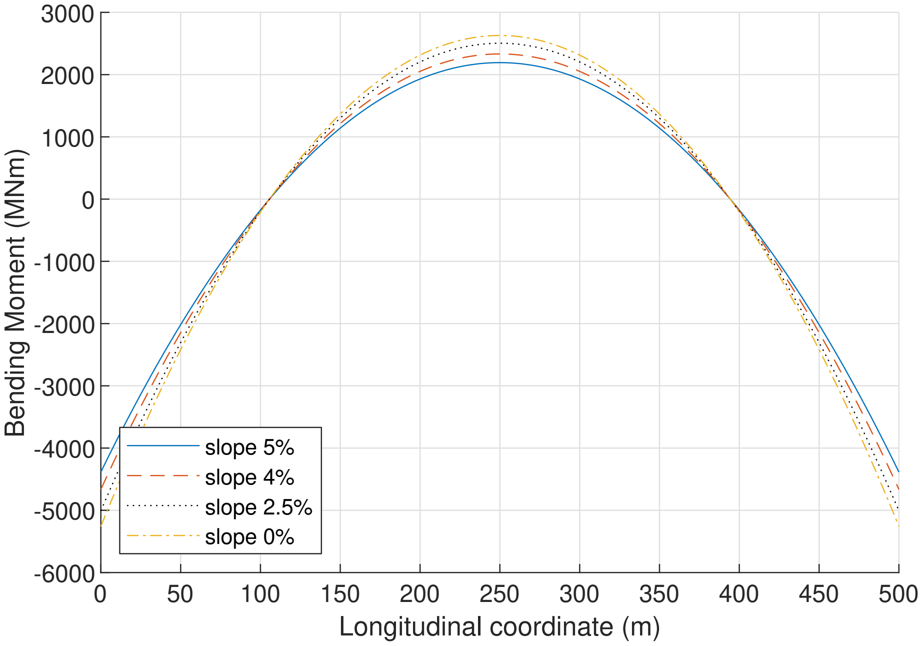

Figure 4.10: Bending moment distribution diagram (M_y), varying the maximum slope of the double clamped parabolic arch.

reduction of positive and negative bending moment are the same.

A sound compromise between the reduction of bending moment from the static analysis, and the recommendations from [Ame, 2002], leads to the adoption of a slope of 4% as illustrated in Fig. 4.11. This configuration is chosen as a preliminary vertical alignment of the SFT.

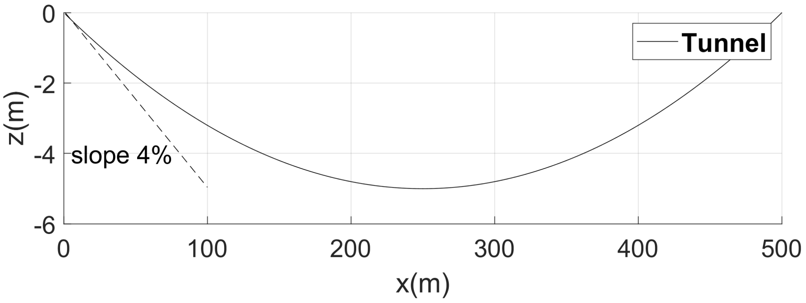

Figure 4.11: Vertical alignment tunnel with a maximum slope of 4% and a rise of $5m$.

4.5.2 Horizontal Alignment

The horizontal alignment can be either straight, with a single curvature, or a double curvature like an S-shape. Horizontally, the arch implies more flexibility in terms of thermal expansion. A reasonable lower bound for the horizontal radius of curvature, is the fulfilment of the stop sight criteria, without widening of the tunnel profile. Horizontal curves based on sight distance should be of desirable radii, rather than minimum standards to alleviate the feeling of discomfort experienced by some drivers in tunnels [Roads, 1993]. In the literature there are several proposal for the minimum radius R_{min} of curvature in tunnels design.

Comparing previous design of SFTB, it was found in [Olsen et al., 2016] a R_{min} of 3200 m, while in [Reinertsen and Group, 2012] a radius of curvature of 2681 m is used. In [Ame, 2002] a R_{min} of 762 m is recommended for tunnel design. Finally in [Bassan, 2017] an extensive study of radius of curvature has been realized. In this study it is concluded that the most severe criteria is the sight distance requirement of trucks vs passenger cars. Considering as design vehicle a truck, R_{min} ranges between 2600 m, considering a design speed of a truck of 110 km/h, and 3755 m considering a speed of 120 km/h. However, speed limit design for trucks higher of 110 km/h are unlikely to be found.

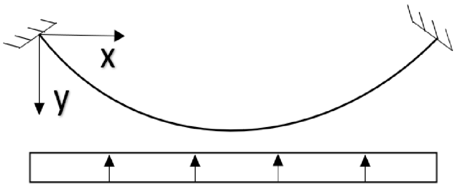

Figure 4.12: Horizontal alignment scheme.

Relatively to the reference system in Fig. 4.12, a parabolic arch for the horizontal alignment is analyzed. The $y(x)$ coordinate a function of the rise of the arch f and the x coordinate.

$$y(x) = 4f[\frac{x}{L} - (\frac{x}{L})^2] \tag{4.15}$$

Assuming superposition of effect a distributed equivalent load q_h, considering swell waves , wind waves and drag force is defined.

$$q_h = F_m + F_D = 75.29 + 68.68 + 6.48 = 150.45kN/m \tag{4.16}$$

A static analysis of the system is performed, taking into account the boundary conditions Fig. 4.12, and the distributed force (4.16). In order to determine the bending moment and shear diagrams, varying the radius of curvature, the principle of virtual work has been used equations (4.11) to (4.14).

As can be noticed in Fig. 4.13, the shear distribution is symmetrical with maxim values at the end sections. Four configurations have been compared. The maximum shear amplitude, corresponding to $R = \infty$ (straight configuration), is $3.51 \times 10^4 kN$. Adopting a radius of curvature of 4 km, there is a reduction of 23.8%, while adopting radius of curvature of 2 and 3 km, the reduction increases to 35.9% and 56.1%.

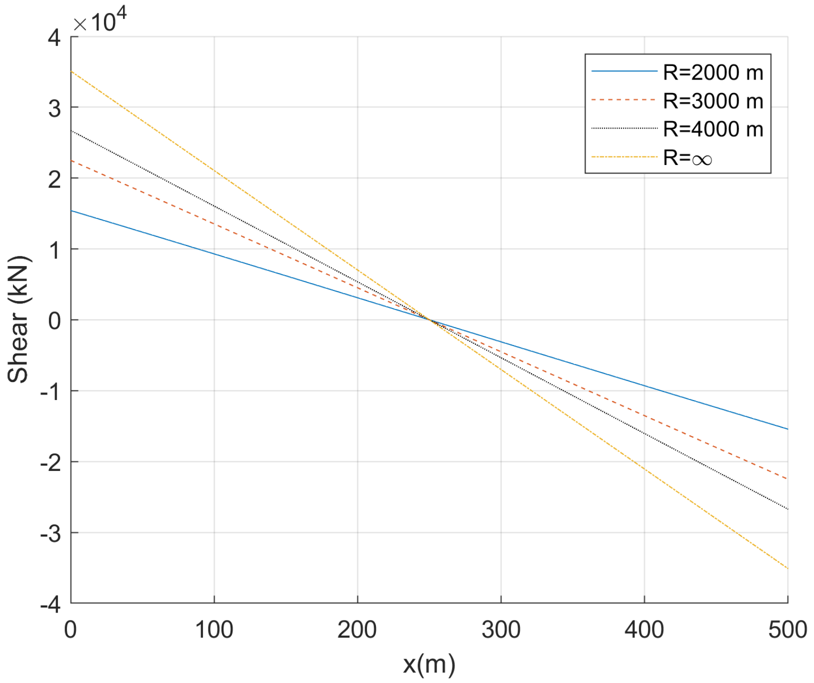

Figure 4.13: Shear distribution diagram (S_y), varying the radius of curvature R, of the double clamped parabolic arch.

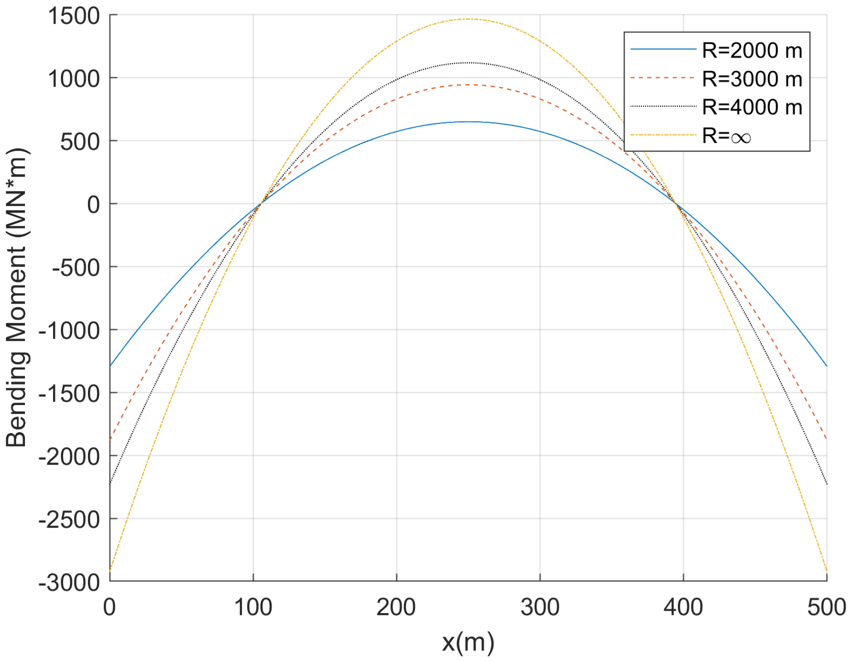

Figure 4.14: Bending moment distribution diagram (M_z), varying the radius of curvature R, of the double clamped parabolic arch.

Four configurations have been compared in terms of bending moment distribution Fig. 4.14. The maximum positive and negative bending moment related to $R = \infty$ are $1463MNm$ and $-2926MNm$. Considering radius of curvatures of 2 km, 3km and 4 km, there are reduction of maximum bending moments of 23.7%, 36.7% and 56.2%. The reductions in percentage are analogous in the end sections and in the mid span.

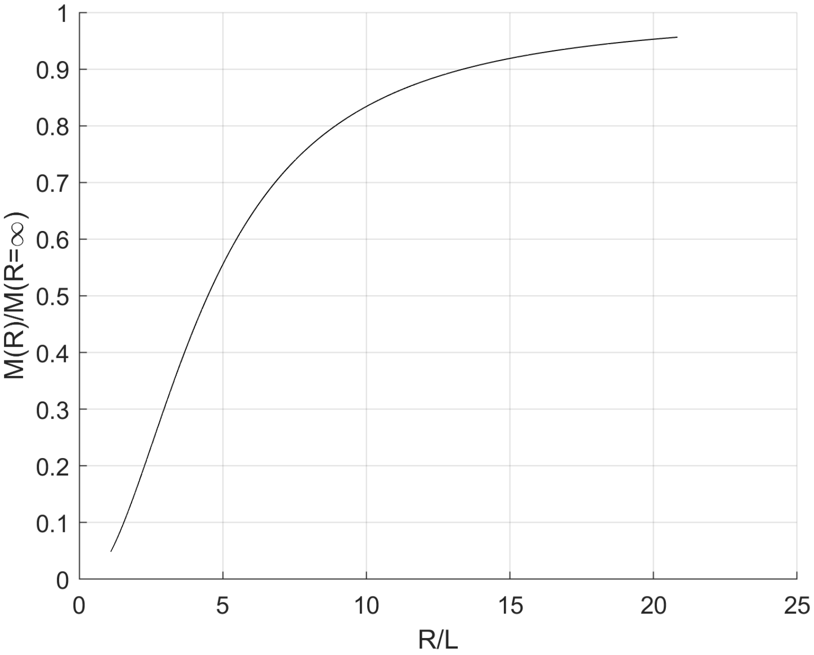

Figure 4.15: Adimensional bending moment trend at the landfall varying the ratio $\frac{R}{L}$, results from analytical static analysis

Fig. 4.15 shows the trend of bending moment at the landfalls, varying the ratio $\frac{R}{L}$. As can be seen from the graph, there is a gradual reduction of bending moment going from a ratio $\frac{R}{L} = 20$ to 7. A steeper reduction, which shows a linear trend, applies for values of $\frac{R}{L} < 7$.

Finally, taking into account :

- Previous design of SFTs;
- R_{min} considering the sight distance;
- the fact that a larger R increases the safety of the users;
- the results of the static analysis.

From these considerations, a radius of curvature $R = 3130m$ is chosen, which correspond to a tunnel rise $f = 10m$. Thanks to this choice there is a reduction of maximum bending moment and shear, compared to the straight configuration , of 34%.

4.6 Conclusions

In this chapter, the geometrical properties of the tunnel cross-section and the tethers are introduced. The materials adopted and the simplified models for composite material are carried out. The structural requirement of interest for this thesis project are explained.

The sea state conditions are described and analyzed. A conservative method for modelling the wave loading, which is naturally a stochastic process, as an individual wave event is explained. The Morison approach is adopted for calculating the drag and inertia forces action on a pipeline with fixed ends. Buoyancy and dead loads are applied as static distributed loads.

A static analytical method for investigate the SFT response is developed and compared with a 2D FEM. The comparison exhibited negligible differences between the two methods. The analytical method is employed for testing the SFT separately in the vertical and horizontal directions, varying the arch rise.

Finally, in consideration of the recommendations given by the norms and previous studies, and the results obtained with the analytical method, a suitable vertical and horizontal alignment is selected. It is so obtained, merging the results in both directions, a SFT preliminary design.

Chapter 5

Modelling of Various SFTs

In this chapter, several submerged floating tunnel are defined. The main diffrences between the various SFTs, are regarding geometrical parameters. The geometrical parameters can be the horizontal and vertical alignment, the number of tethers, the tethers inclination and general boundary conditions.

It contains also information about the SFTs modelling with the software ABAQUS. The models are tested with static, modal and dynamic response analyses for hydrodynamic loading. The simplifications made during modelling are described in each section. It is fully reported only the modelling of one tunnel. The other SFTs are modelled in a similar way, the differences are listed in each section.

5.1 Applied Software

5.1.1 Abaqus

Abaqus is a suite of commercial finite element codes, part of the SIMULIA range of products. It consist of Abaqus Standard, and Abaqus Explicit. Data input for a finite element analysis can be done either trough Abaqus/CAE interface or by scripts of Keywords [Khennane, 2013].

In this thesis project data is entered using the text editor Notepad++, and executed through the command line. Several add-on options are available in Abaqus. For offshore structure, the Abaqus/Aqua option can be used. Abaqus/Aqua contains features that are specifically designed for the analysis of beam-like structures installed underwater and subjected to loading by water and wave actions. Abaqus/Aqua is avaible just for the Abaqus keyword edition, therefore all the models in the thesis are designed through this edition. ABAQUS/Aqua analysis can be performed using the static, direct-integration dynamic and eigenfrequency extraction procedure.

5.1.2 Matlab

MATLAB (Matrix Laboratory) is a high programming language specially designed for modelling, simulations, development and algorithms, and analysis of data. Data elements are built in dimensionless array making it convenient to solve matrix and vector problems through a faster build up than languages as C or Fortran would require [Attaway, 2011]. In this thesis project, Matlab has been used to generate script for the software ABAQUS, for post-processing results, and for processing analytical methods. Graphics and array interpretation are created trough Matlab.

5.1.3 Abaqus2Matlab

Abaqus2Matlab is a novel software that connect Abaqus, a sophisticated finite element package, with Matlab, the most comprehensive program for mathematical analysis [Papazafeiropoulos et al., 2017]. The program interface between the two software, it can process and integrate plotting features of Matlab. Moreover, opens up new opportunities in results post-processing, statistical analysis and mathematical optimization, among many other possibilities. In this thesis Abaqus2Matlab is used mainly for post-processing the results.

5.2 Model Development and Geometry

Four main structural components are identified in the model.

- The tunnel tube;
- the anchoring system (tethers);
- the shore connections;
- the tether connections.

Details on modelling of each section are presented throughout this chapter. Four models are modelled and developed in this thesis. All the Abaqus models are designed in a three dimensional environment. The base model is create from the results of the conceptual design phase.

In both vertical and horizontal direction a parabolic arch shape is used equations (4.15),(4.10). The maximum vertical slope chosen is 4%, which correspond to an arch rise of 5m. The radius of curvature in the horizontal direction is $R = 3130m$, which correspond to an arch rise of 10m.

As can be seen in Fig. 5.3, one cable is inclined of 45°, and the other is vertical. The arch configuration is stiffer in one planar direction compared to the other. The tether inclination of 45° is chosen in agreement with [Yiqiang and Chunfeng, 2013].

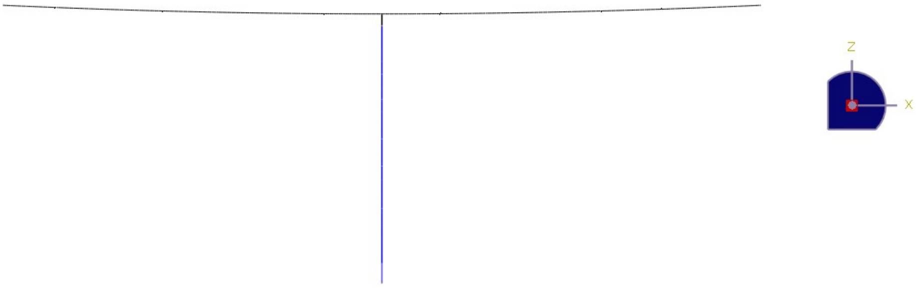

Figure 5.1: Abaqus model of the base case SFT, x-z plane view

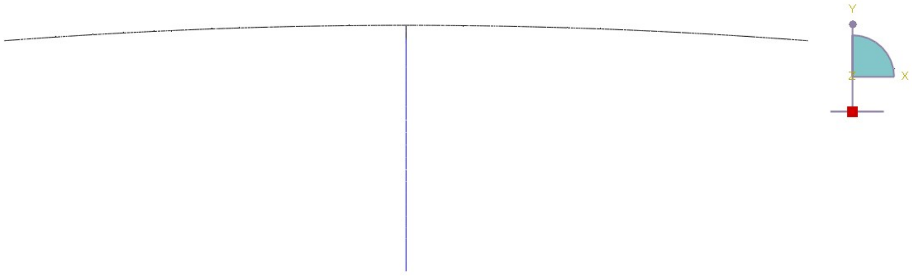

Figure 5.2: Abaqus model of the base case SFT, x-y plane view

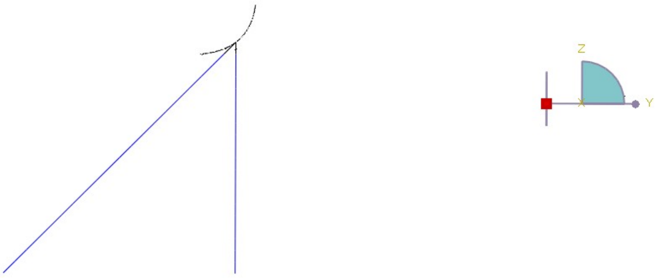

Figure 5.3: Abaqus model of the base case SFT, y-z plane view

5.2.1 Model Configurations

The model base briefly described in 5.2, is compared with other three SFT configurations. The base case has the tunnel alignment obtained during the conceptual design phase, one vertical tether and one inclined. It is chosen to fully described the base case (model C), only for the reason that is the most complex model in this thesis project. The three additional models are created with the same boundary conditions. The differences between the models are regarding, the vertical and horizontal radius of curvature, the tether number and inclination.

The first model (model A) is analogous to the base model for the tunnel part, with the difference that no tethers are present. Model A is created with the intent of analyze the importance of tethers, and if the tunnel with only abutment anchoring is feasible.
A second model (Model B) has the same tunnel orientation as the base model, and it has two vertical tethers. The two vertical tethers are connected to right and left side of the

tunnel outer section. Model B is useful to understand if the arch configuration itself has a sufficient horizontal stiffness, or if horizontal support are needed.
Finally a basic configuration (Model D) is made in order to estimate the effect of the double arch configuration on the SFT. Model D has a straight tunnel alignment and two vertical tethers at the mid span.

The water ballast distribution is considered constant, in order to have a more clear comparison between the different configurations. However, the water ballast distribution could be optimize in order to reduce the bending moment actions and shear forces due to vertical actions.

The buoyancy weight ratio (BWR), is chosen carefully for each model in order to avoid slack in the tethers. However, for tether stabilized SFTs, only BWR values that ranges between 1.2 and 1.5 are considered, in agreement with previous designs reported in section 2.1. For the tunnel anchored only in the abutment, lower values of BWR are considered. The main geometrical properties of the four models are reported in Table 5.1.

Table 5.1: Geometrical properties of models A, B, C and D

Model	A	B	C(base)	D
Main span (m)	500	500	500	500
Clearence above the tunnel (m)	40-45	40-45	40-45	40
Number of lay by	0	0	0	0
External diameter tunnel (m)	12.6	12.6	12.6	12.6
Internal diameter tunnel (m)	11	11	11	11
Tether diameter (m)	1.029	1.029	1.029	1.029
Tether thickness (m)	0.068	0.068	0.068	0.068
Number of tether	0	2	2	2
Tether inclination (°)	/	0	0&45	0
Tether-Tunnel connection	/	pinned	pulley	pinned
Tether-Ground connection	/	pinned	pinned	pinned
Horizontal radius of curvature (m)	3130	3130	3130	0
Vertical slope (%)	4	4	4	0
Horizontal arch rise (m)	10	10	10	0
Vertical arch rise (m)	5	5	5	5

The four models are illustrated in Figs. 5.5a to 5.5d, through an Abaqus rendering. The figures are intended just to have a better understanding of the tunnel configurations.

(a) Model A **(b)** Model B

(c) Model C **(d)** Model D

Figure 5.4: Rendering of models A, B. C, D in Abqaus/Aqua.

5.2.2 Abaqus Elements and Connectors

In order to create a realistic global model, a number of element and connectors is used. Abaqus/aqua environment is compatible with a reduced number of elements. The elements are used with the aim to better represent the real structural element.

The main model sections are the concrete pipe, the tethers, the pulley and the water surface. The element list and application is here listed :

SFM3D4R :	4-node quadrilateral surface element, reduced integration
MASS :	Point mass
CONN3D2 :	Connector element in space between two nodes or ground and a node
B31 :	2-node linear beam in space
SPRING1 :	Spring element between a node and ground, acting in a fixed direction

The element information has been gathered from Abaqus documentation, which is available along with Abaqus or on various websites.

Elements SFM3D4R are used to model the water surface. The water surface visualization is important in order to know the wave position with respect to the tunnel displacement during time.

MASS element are used in order to add when necessary pointless mass, in the model a pointless mass is used to describe the pulley weight.

CONN3D2 elements are used in order to model the pulley connection between the tunnel and the tethers in the base model. In particular it has been used the ”slipring” option.

B31 elements have been adopted to model the tunnel pipe and the tethers, for both cases the typology ”pipe” has been used. With beam element is not possible to reproduce exactly the cross section of Fig. 4.1. Therefore, a simplification is made adopting a circular cross section and neglecting the inner parts related stiffness and mass.

SPRING1 elements are used to simulate the abutment stiffness, defining the end section boundary stiffness of the tunnel.

5.2.3 Tether Arrangement

The tension leg arrangement and the BWR play a very important role in controlling the dynamic response of SFTs. Slack in the tethers would cause an impulsive snap load, which would endanger the SFT users. Three design measures to prevent slacking are adopted in this thesis project.

- Adopting a sufficiently large buoyancy weight ratio in order to reduce fluctuation due to wave force;
- adopting a tunnel circular cross section, which reduces rotational moment due to fluid forces;
- introduce a pulley between the tethers and the tunnel cross section.

In Fig. 5.5 is depicted the tether arrangement for models B, C and D, with the blue arrow is indicated the wave and current directions. The pulley is adopted only in model C, which is more sensitive to slacking effects than models B and D.

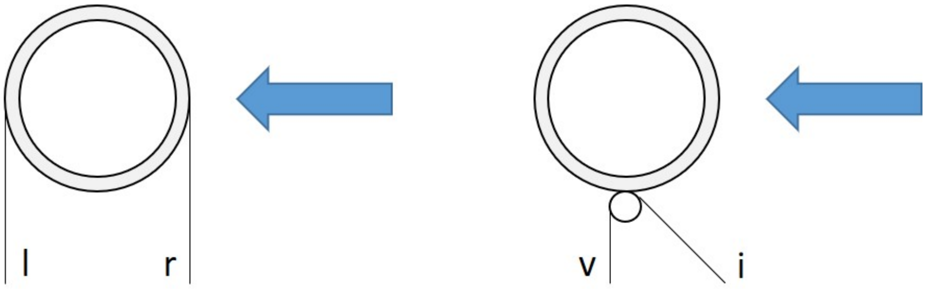

Figure 5.5: Tether arrangement for models B, D (left) and model C (right)

The labels l, r, v, i in Fig. 5.5 indicates the tether position, the mean respectively left, right, vertical and inclined.

Pulley design

When dealing with large displacements of the structure, a design feature like a pulley system can be used. Slack of tethers is likely to occur when rotational movement of the tunnel are present. The pulley system reduces the displacements of the tethers and at the same time it keeps the tethers in tension. Thanks to these feature horizontal and vertical restoring forces from the tethers to the tunnel are still present. Moreover, being reduced the displacement of the tethers, the probability of having slacking effect in the tethers is reduced.

The importance of the tunnel-tether connection is argued in the SFT design, presented for crossing Funka Bay in Japan, [Kanie, 2010]. In the Funka Bay design, a flexible and frictionless leg is installed around the tunnel in order to connect a couple of tethers. On this way the forces between the tethers are kept automatically in equilibrium. However, no detailed information about the frictionless belt installed around the tunnel cross section are given, therefore a pulley system is adopted in this thesis project.

Pulley systems are already adopted in marine environment, for instance are used to mooring floating structures or vessels. Several products are already available in the market. An European patent application of a mooring pulley tensioning system is described in [Torkjell, 2017]. The purpose of the invenction is to connect the mooring line to a tensioner, in order to keep the desired tensioning level in the mooring line during over time Fig. 5.6.

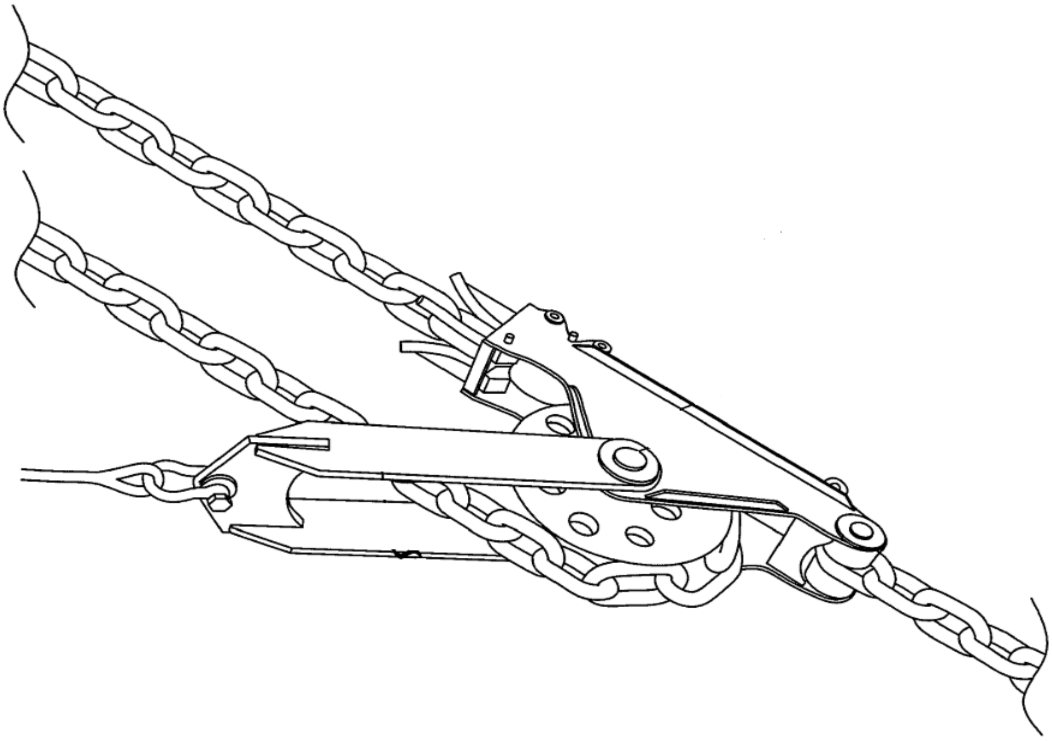

Figure 5.6: Configuration of a pulley system attached to a wire tensioner [Torkjell, 2017]

In the offshore standards DNVGL-OS-E301 [DNV GL AS, 2015], criteria, technical requirements and guidelines on design and construction of position mooring systems, can be founded. According to DNVGL-OS-E301, when a wire rope pass through a pulley, it has to be verified for a fatigue analysis considering bending effects too. Considering a nominal stress range, the failure correspond to a specific number of cycles, Fig. 5.7. For the wire it can be used either a spiral-strand, a six-strand, an open link or a stud-link.

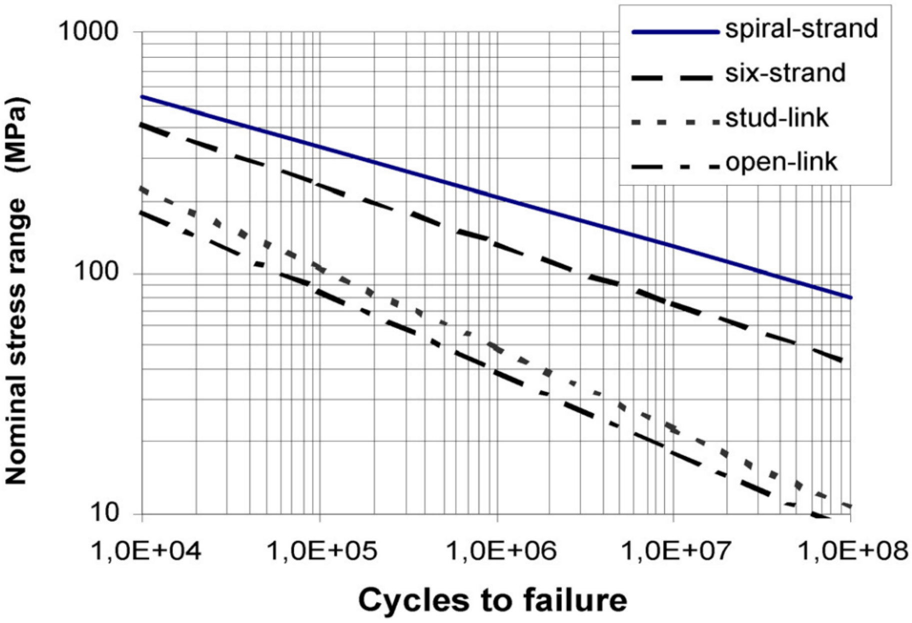

.

Figure 5.7: Number of cycles to failure for nominal stress range in sea water, related to spiral-strand, a six-strand-, an open link or a stud-link element,[DNV GL AS, 2015]

The pulley is modelled in Abaqus using SLIPRING connectors, which are part of the CONN3D2 elements. Connection type SLIPRING provides a connection between two nodes, and it offers the possibility to model material flow and stretching between two points, like belt system. SLIPRING connectors are generally used to model seat belt or pulley. The pulley mass is added to the model through MASS element, the spiral-strand mass is included in the SLIPRING distributed mass.

The pulley modelled in Abaqus, Fig. 5.8, is interposed between the tethers and the tunnnel cross section. The pulley is assumed rigidly connected to the cross section, and its radius is assumed null in the finite element model. The pulley in reality could be circular or non circular, in Abaqus it is model as an infinitesimal point.
The radius of the pulley is related to the number of complete rotations during the tunnel oscillations, this however, requires a more detailed design of the cross-section. A non circular pulley can be also used in order to reduce the number of complete rotations on itself.

The Coulomb-like frictional effect is assumed for the pulley design (5.1).

$$T_1 = T_2 e^{-\mu\alpha} \tag{5.1}$$

where:

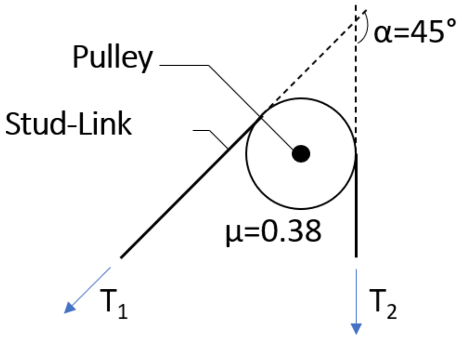

Figure 5.8: Pulley system

T_1	is the axial force in the inclined tether
T_2	is the axial force in the vertical tether
α	is the angle between the tethers
μ	is the friction coefficient

Stud-link elements can withstand only tensile forces. Therefore in the FEM the stud-link bending stiffness is set to zero. The following parameters are used for the SLIPRING elements Table 5.2.

Table 5.2: SLIPRING elements parameters used for modelling the stud-link pulley system.

Parameter	Stiffness	Weight	Friction coefficient	Angle
Unit	(N/m)	(kg/m)	(/)	(°)
Value	990×10^6	1750	0.38	45

The friction coefficient of the pulley is chosen in order to avoid rotations under the effects of static loads. In pulley design the friction coefficient can be adjusted varying the contact surface and the pulley geometry, which is typically a flat belt pulley or a V belt pulley.

5.3 ABAQUS Aqua Analysis

For beam and truss elements immersed in fluid, ABAQUS/Aqua provides capability to model buoyancy, ballast , added mass, waves and current loads. The environmental conditions to be reproduced in the model are the water depth and properties, the gravitational constant , the wave height and period and the current velocity and direction.
Non linear geometry is included in all the analysis performed.

5.3.1 Environmental Properties

ABAQUS/Aqua problems require the definition of the environmental properties of the marine environment. The marine environment properties can be divided in basic sea properties, such as sea bed elevation, or optional properties such a specific wave state.

Basic sea properties

The basic sea properties in ABAQUS/Aqua are unique for the static analysis and the modal analysis. Abaqus requires the definition of fluid properties and steady current velocity in order to define the model environment. Aqua loading require the definition of sea bed and free surface elevation , fluid density and gravitational constant. The values are reported in Table 5.3.

Table 5.3: Fluid properties

Parameter	unit	Value
Water density	(kg/m^3)	1025
Sea bed depth	(m)	-200
Free surface elevation	(m)	0
Gravitational constant	(m/s^2)	9.81

Steady currents are defined by giving the steady fluid velocity, as a function of position and elevation. The most unfavorable situation is when the current is perpendicular to the beam axis, the amplitude is assumed equal to 1 but it can be modified during the analysis by a multiplier. Current velocity and directions are reported in Table 5.4.

Table 5.4: Current velocity

Direction (/)	Velocity (m/s)	Elevation (z) (m)	Position(x,y) (m,m)
x	0	0 to -200	All
y	-1	0 to -200	All
z	0	0 to -200	All

The parameter ”All” in table 5.4 it is used to indicate that the velocity is assumed constant along all the tunnel longitudinal coordinate, and in each point of the cross section.

5.3.2 Harmonic Wave State

In order to define gravity waves, a wave theory must be specified. ABAQUS/Aqua has three built in wave theories, and offer also the possibility of a user defined wave theory. There are:

- *Airy wave theory*, is generally used when the Ursell parameter is smaller than 1, the ratio of wave height to water depth $H/d < 0.03$, and deep water assumption should be valid. Multiple train waves with different wave period and wave height can be defined, in this case the fluid particle velocities and accelerations will sum by linear superposition.

- *Stokes fifth-order wave theory*, is another deep water wave theory that is valid for relatively larger wave lengths than the previous theory. To be applicable the Ursel Parameter should be smaller than 10. Linear superposition is not valid, therefore only a single wave train can be defined.
- *Gridded wave data*, is possible to define surface elevations, particle velocities and accelerations at different points in grid, the software interpolates the values between the defined points.

In order to choose the most feasible wave theory the parameters in Table 5.5 are analyzed. As recommended by [Olsen et al., 2016], the maximum individual wave event modelled as a regular Airy or Stokes waves, can be taken as $H_{max} = 1.9H_s$ and $T_{max} = 0.9T_p$. Subscript a, b, c, d refers to different swell and wind wave combinations, typical of the Norwegian fjords, these values were provided by the Norwegian Public Road Administration. It can be noticed that all of them fulfil the Airy wave theory assumptions, which are here outlined:

Table 5.5: Design regular wave parameters

Wave type (/)	Period (T_{max}) (s)	Height (H_{max}) (m)	Length (L) (m)	Ursell p. (/)	H/d (/)	d/L (/)
Swell$_a$	15.3	1.33	364.62	0.022	0.007	0.55
Swell$_b$	15.3	2.09	364.62	0.035	0.01	0.55
Swell$_c$	15.3	4.37	364.62	0.072	0.021	0.55
Swell$_d$	15.3	5.7	364.62	0.095	0.028	0.55
Wind$_a$	4.95	3.61	38.24	$<< 1$	0.018	5.23
Wind$_b$	4.95	3,8	38.24	$<< 1$	0.019	5.23
Wind$_c$	6.75	4.56	71.11	0.002	0.023	2.81
Wind$_d$	7.65	5.32	91.34	0.005	0.027	2.19

$$\left\{\begin{array}{ll} \frac{d}{L} > \frac{1}{2} & \rightarrow deepwater \\ \frac{H}{d} < 0.03 & \\ Ursell \quad parameter << 1 & \end{array}\right\} \Rightarrow Airy \quad Wave \quad Theory \tag{5.2}$$

Since all the conditions necessary to adopt the Airy wave theory are fulfilled, this theory is adopted for all the models in this thesis project. The Airy wave theory allows linear superposition, therefore swell and wind waves can be added simultaneously to the model. The current velocity is $1m/s$ in all the load combinations considered. In the regular wave model the wave direction is assumed constant and perpendicular to the tunnel longitudinal coordinate. Thanks to this assumption and the alteration of the wave parameters, a conservative result is expected.

5.3.3 Irregular Wave State

Irregular waves analysis is used to find the maximum response of the floating structure, and have a comparison with the regular wave analysis. In order to compute a spectrum analysis, adopting for instance the Jonswap wave spectrum, an Abaqus subroutine can be used. For comparing the results with the harmonic analysis the analysis needs to run for three hours. This because the significant wave height is estimated based on the 50 year return period wave for a 3-hour sea state.

In this thesis project a simplified version of the double peak spectral model for sea waves is adopted. The full description of the method can be founded in [Torsethaugen, 1993].

The irregular wave state is analyzed in order to have a comparison with the regular wave state method adopted previously. Only the swell and wind wave combination (a) is considered, which has the following parameters: $H_s = 0.7m$, $H_w = 1.9m$, $T_s = 17s$ and $T_w = 5.5s$.

According to [Torsethaugen, 1993], the considered sea state is classified as a swell wave sea,i.e. governed by waves entering into the location from other areas.

In this analysis is also taken into account the wave energy spreading function, section 3.3.4, with a spreading parameter equal to 6. Through this function the wave direction can be randomly generated.

Simulation of single point time series

A time domain simulation is obtained by the reverse process adopted to generate the auto-spectral density, [Strømmen, 2006]. A time domain representative, $x(t)$, can then be obtained by subdividing S_x into N blocks along the frequency axis.

$$x(t) = \sum_{k=1}^{N} c_k cos(\omega_k t + \Psi_k) \tag{5.3}$$

where

$$c_k = \sqrt{S_x(\omega_k)\Delta\omega_k} \tag{5.4}$$

and where Ψ_k are arbitrary phase angles between zero and 2π.

In order to consider the wave spectrum and the wave energy spreading function and insert them in Abaqus/Aqua, the wave amplitude as a function of the wave frequency and angle is considered in the following way

$$c_k(\omega_k, \beta_j) = \sqrt{S(\omega_k)S(\beta_j)\Delta\omega_k\Delta\beta_j} \tag{5.5}$$

where $S(\omega_k)$ is the double peak wave spectrum, $S(\beta_j)$ is the wave energy spreading function. In this way, an artificial generation of a two-dimensional random process is made, additional information can be founded in [Newland, 2005a]. A random phase angle is generated in Matlab and directly added in the Abaqus script. The randomly generated wave height,period, direction and phase are inserted in Abaqus/Aqua using the linear wave Airy theory.

Statistics of narrow band processes

Many random process in civil engineering can fairly be approximated as narrow banded. The approximation is often reasonably good and it greatly simplifies statistical analysis of the process.

Assuming that $X(t)$ is a stationary process narrow-banded, the average number of crossing a value a is proportional to the period T. Generally in sea engineering the time between independent sea state is taken equal to 3h [Veritas, 2002].

If $X(t)$ is a Gaussian process the probability distribution function (PDF) of any peak value, chosen at random, exceeds a is

$$f_A(a) = \frac{a}{\sigma^2} e^{-a^2/2\sigma^2} \tag{5.6}$$

where A is the value of a peak in a narrow banded process.
If the peaks in $X(t)$ are independent and identically distributed (IID), and A_{max} is the amplitude of the maximum of all the peaks. The cumulative distribution function (CDF) of A_{max} is

$$F_{A_{max}}(a) = (F_A(a))^N \tag{5.7}$$

where N is the number of peaks, and F_A the CDF of peaks.

$$F_A(a) = \int_{-\infty}^{a} f_A(\alpha) d\alpha \tag{5.8}$$

The PDF of A_{max} can be written as

$$f_{A_{max}}(a) = N f_A(a)(F_A(a))^{N-1} \tag{5.9}$$

5.3.4 Static Analysis

In the static analysis are considered dead loads, traffic loads and buoyancy.
The dead loads are composed of weight of the concrete pipe and tethers, which is automati-

cally calculated by Abaqus once given the material properties, and the non structural mass. The non structural mass is an option included in Abaqus, and it is used to include the mass contribution from non structural features in the model. The water ballast is included in the non structural mass.

Traffic loads are modelled as equivalent static loads, in agreement with [Olsen et al., 2016], and applied as an uniformly distributed load in the tunnel center line.
The buoyancy is included in Abaqus/Aqua through a specific function for buoyancy loads. The buoyancy during the static analysis is constant and it is based on the Archimede's principle.
The prestressing is modelled through a temperature gradient. This is an approximation, but no other simple solution are available for Abaqus/Aqua. BRGADE/plus6.1, a finite element model based on Abaqus would be necessary for modelling pretension. A summary of the static loads is reported in table 5.6.

Table 5.6: Loads on static analysis in Abaqus

Parameter	Unit	Value
Concrete pipe	(kN/m)	811
Single tether	(kN/m)	21.9
Non structural mass	(kN/m)	185
Traffic Load	(kN/m)	40.5
Pretension	(MPa)	10

The wave and current actions are calculated by Abaqus adopting the Morsion equations, section 3.3.2. The input parameters required are the tunnel and tethers diameters, the inertia and drag coefficients.
The buoyancy load is set to a sufficient value in order to avoid slack in the tethers and reduce dynamic response. Models A, B, C, and D, have therefore different Buoyancy loads, which are be reported in the chapter relative to the results. The static results are will be compared between the four models in terms of deformations, internal forces and dependency on the BWR.

5.3.5 Modal Analysis

Extract the eigenvalues of the system, and so its natural frequencies is important in order to investigate possible bifurcations associated with kinematic instabilities. Abaqus offers different alternative eigenvalue solvers. The Lanczos method is well suited for solving moderate sized to big problems, when a few up to some hundred eigenvalues are desired. The theoretical background of the finite element modal analysis is explained in section 3.4.1. Lanczos algorithm is used thanks to the assumption that the system has a low damping and so the damping matrix can be neglected during the eigenvalues extraction.

The added mass, which is not negligible for submerged structures, it is considered in Abaqus/Aqua through a specific coefficient C_a, called added mass coefficient. The added mass coefficient is set equal to 1 for both the tunnel and the tethers.

Eigenfrequencies and Eigenvectors

As explained in section 3.4.1, the system is assumed undamped and the stiffness matrix positive definite. The basic equation in order to calculate the eigenfrequency and eigenvectors for the $i - mode$ is :

$$([K] - \omega_i^2[M])\{\Phi_i\} = \{0\} \tag{5.10}$$

The square root of the eigenvalues $\omega_i^2 (i = 1, 2, ..., n)$ are the natural frequencies of the system, and the eigenvectors$\{\Phi_i\}$ its mode shapes. A system has n eigenvectors and eigenvalues, where n is the number of degree of freedom. The natural frequency of interest are the ones similar to the frequency of the dynamic loads.

The amplitude of the structural response is highly influenced by its natural frequencies. Resonance and vibration on offshore structure is a common problem. Resonance occurs when dynamic forces frequencies coincide with the natural frequencies of the structure. At resonance, the forces are highly amplified and this can cause large vibrations, over the operational limit. Load frequency and amplitude, for loads such as wave loading ans vortex induced vibrations, should therefore be analyzed carefully.

In Abaqus/Aqua, by default the modal shapes are normalized with respect to displacement.

Effective Mass Participation

The effective mass paricipation is related to the modal participation factor, the underlying theory is described in section 3.4.1. The effective mass participation is performed in order to estimate how many modal shapes are relevant for the structure. Modal shapes with an higher effective mass participation are more relevant than modes with a lower effective mass participation. That is due to the fact that the effective mass is directly related to the deformation and stresses amplitude.

The number of significant modes required has to include approximately 90% of the mass participation. This is reported directly in the Abaqus/CAE message file and should be checked after each frequency analysis.

5.3.6 Damping Parameters

Abaqus builds the damping matrix [C] adopting the so called Rayleigh method, which theoretical back ground is reported in section 3.4. When a number of significant modes m has been established from the previous section 5.3.5, the Rayleigh parameters can be estimated following the procedure described in section 3.4.4.

The procedure requires that the damping ratio of the $1^{st} mode$ and the $m^{th} mode$ are assumed. In order to be on the safe side, low damping ratio amplitude are assumed and reported in (5.11).

$$\xi_1 = 0.008 \quad and \quad \xi_m = 0.02 \tag{5.11}$$

5.3.7 Dynamic Analysis

The dynamic analysis selected in Abaqus is a direct integration analysis performed trhough the HH-T method, which is reported in section 3.5.2. The numerical damping in Abaqus is controlled by the parameter α, which is limited between -0.5 and 0. The parameters γ and β are related to α, as reported in the Abaqus manual :

$$\begin{gathered} \beta = \frac{1}{4}(1-\alpha)^2 \\ \gamma = \frac{1}{2} - \alpha \end{gathered} \tag{5.12}$$

The value of $\alpha = -0.333$ provides the maximum numerical damping, while a value of $\alpha = 0$ does not provide damping. In this thesis project a value of $\alpha = 0.05$ is chosen, which provides slight numerical damping.

The deterministic dynamic analysis is performed by modelling the waves through the linear Airy wave theory. The added mass and drag coefficient are reported in section 4.4.3.

The buoyancy load require the definition of fluid density, sea bed and free surface elevation, and the gravitational constant. For beam element only the external diameter of the element is required as an input. When buoyancy loading is applied in conjuction with a gravity wave, the dynamic pressure due to the disturbance of the still surface is added to the hydrostatic pressure, to obtain the total buoyancy loading.

5.4 Sensitivity Studies and Optimization

Design sensitivity analysis plays a central role in structural optimization. Structural design sensitivity analysis concerns the relationship between design variables available, and structural responses determined. The dependence of the response measures such as displacement, stress, strain and natural frequency is implicitly defined through the governing equations of the structural system [Choi and Kim, 2005].

The purpose of sensitivity analysis is to obtain a structural optimization. Structural design problems intent is to find the most favorable design among many possible candidates. However, each candidate design must exist within a feasible design region to satisfy the problem constraints. Thus, the goal of the design optimization problem is to find a design that minimizes the cost function among all feasible designs.

In this thesis project the costs are not directly estimated, however is always considered that a reduced number of element, or lower stresses, correspond to a smaller amount of material needed. The erection phase feasibility is not considered, even thought is contemplate the fact that the implementation of a double curvature SFT is more complex than the straight configuration.

5.4.1 Buoyancy Weight Ratio

The buoyancy weight ration (BWR) changes the vibration characteristics and affect the internal forces amplitude of the SFT. Selecting an appropriate BWR value is a significant design step in the design of a SFT [Lin et al., 2018]. Previous results regarding the effect on BWR on SFT are found in section 2.5. Generally, comparing other SFT designs, the following drawbacks and advantages in increasing the BWR are expected.

Drawbacks in increasing the BWR

An higher BWR implies higher vertical distributed forces on the SFT. The buoyancy force is generally the main vertical force for tether stabilized SFTs. Higher vertical forces imply larger stresses in the tunnel and the tether, and wider vertical static displacements.
Tether foundations are typically gravity foundations for soft clays and mixed soils, and drilled piles in rock [Olsen et al., 2016]. Higher restoring forces in the tethers, and so in its foundations, requires a larger mass if gravity foundations are adopted, and a larger number of piles if pile foundations are adopted.

Advantages in increasing the BWR

Whereas the drawbacks in increasing the BWR are easier to be predicted, due to the fact that they are related to static analysis, the advantages are more related to the dynamic response of the system. Generally, an higher BWR reduces the probability of slacking in the tethers, but it also varies the natural frequencies of the system.

Several static, modal and dynamic analysis varying the BWR are performed and the results are discussed in section 6.4.1.

Tether stress

The tether initial stress is is governed by the buoyancy weight ratio (BWR). An higher tether initial pretension decreases the probability of slacking. On the other hand and higher tether pretension could lead to plastic deformations during dynamic loading. Moreover, an higher tension in the tethers requires higher restoring forces in the foundations.

Several static analysis are performed for the models B, C and D with different values of BWR. In the static analysis are considered all the static loads, and the dynamic loads are introduced through equivalent static forces through the Morison equation.

Modal analysis

Tether stabilized SFT vibration characteristics are strictly related to the buoyancy weight ratio of the tunnel. A sensitivity analysis on how the natural frequencies are influenced by the BWR, is important in order to avoid natural frequencies on the range of the dynamic actions frequencies. In this thesis project the regular wave actions considered, have a design period that varies between $4.95s$ and $15.3s$, as reported in Table 5.5.

The first four natural periods of the SFTs are analyzed, periods related to higher order modes are out of the significant wave period range. Models B, C and D are tested for BWR that ranges between 1.2 and 1.5.

5.4.2 Abutment Stiffness

The stiffness offered by the abutment connection is an interesting and necessary study in the design of a SFT. To establish a fixed end connection is generally expensive in economical terms. A suitable compromise in terms of stiffness and economical cost is expected to be in between a pin connection and a fixed connection.

In this thesis project are analyzed the global structural response and modal properties varying the stiffness at the end sections. The results are compared in terms of bending moment, displacement and natural period of the structure. The connection is not designed, being out of the scope, but only the output of different assumed stiffnesses are compared.

The translational supports at the end sections are assumed rigid and inserted in the models as pin connections. The rotational stiffnesses are modelled with rotational spring elements.

5.5 Analysis Steps

Here is reported an infographic, Fig. 5.9, which summarizes the basic steps that are followed during the development of the models.

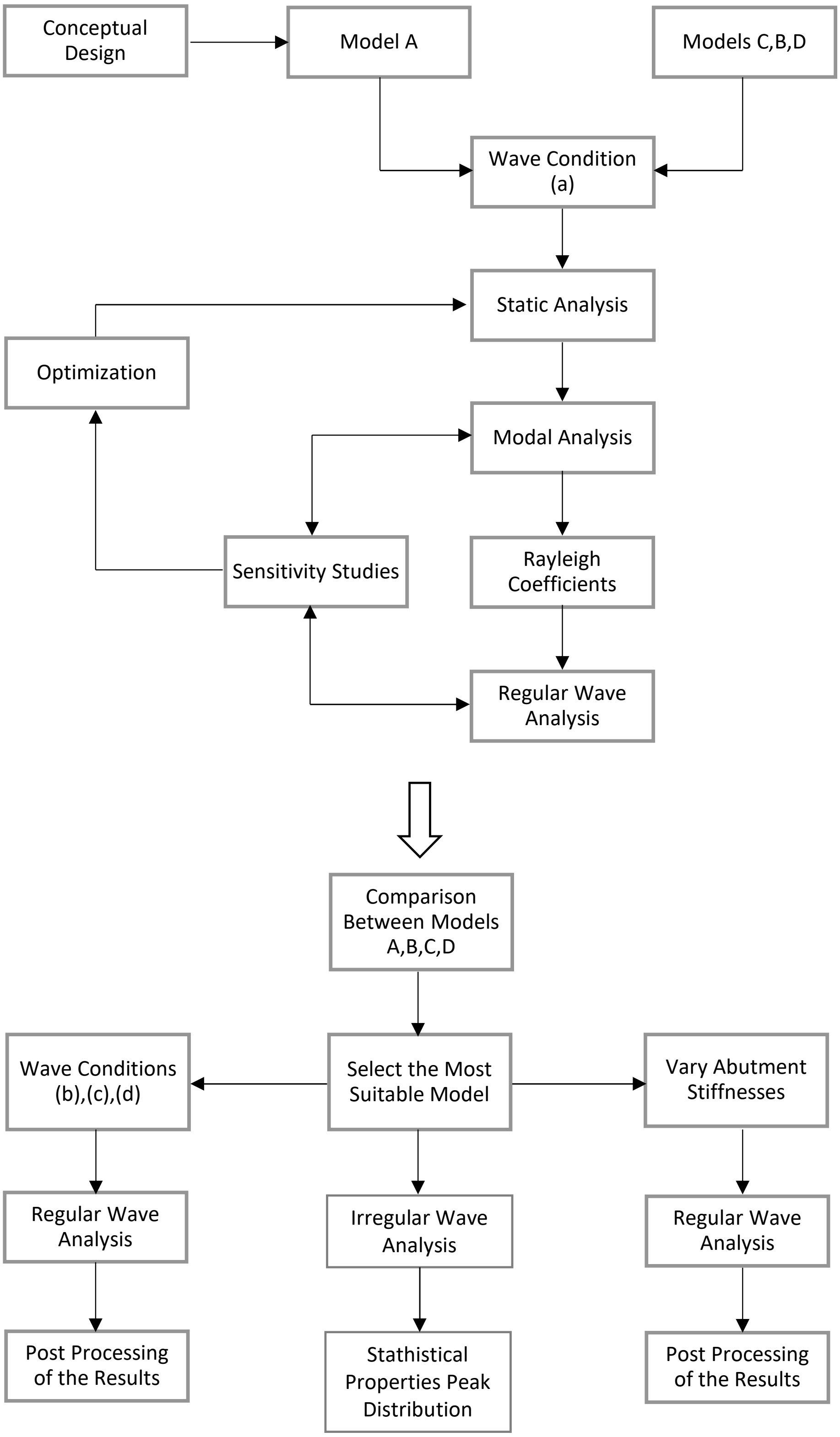

Figure 5.9: Infography of the main steps

All the informations related to each step in Fig. 5.9 were explained in detail in the previous sections. Not all the cycles of optimization are reported in this thesis project, but only the results relative to the final configurations chosen.

The optimization phase includes also the BWR parameter, an higher BWR implies higher static internal forces, but it can reduce the dynamic response. The aim is to to find a trade-off varying the BWR. The BWR in Abaqus/Aqua can be modified simply by an amplification factor. In reality this can be done for instance adopting light weight concrete or varying the water ballast volume.

The choice of the most suitable model between the four analyzed is limited to the loading conditions considered in this thesis project. Moreover, the costs and the installation process complexity for each model are not considered, even though is known that a curved tunnel shape implies higher costs than a straight SFT configuration.
The most suitable model is so found considering internal forces amplitudes, oscillations and accelerations, and the amount of material to be used. In addition is expected to fulfill the structural requirements detailed in section 4.2.

During the optimization phase, the necessary amount of tethers is selected. The constraint is to not overcome the yielding limit of steel in the tethers.
The model geometries are listed in section 5.2.1. The load combinations for the regular wave analysis are reported in Table 5.5. Static analysis, modal analysis , Rayleigh coefficient determination and dynamic analysis are described in sections 5.3.4 - 5.3.7. The end connections stiffnesses are described in section 5.4.2.

Chapter 6

Analysis Results and Description

This section presents the results from the analysis described in chapter 5. It includes results from the finite element analysis, and the analytical methods that are not included in chapter 4. The results are described and commented along each section.

The response of the static analysis is reported in terms of global displacements, rotations, bending moments. For the dynamic analysis, accelerations are also measured. In the modal analysis natural frequencies and modal shapes are illustrated. Throughout the chapter, it is commented whether the model satisfies the stated criteria in section 4.2.

All the results presented in this section are derived after many cycles of optimization as summarized in section 5.5. The design strategies adopted for each model are described mutually the results. In agreement with [Olsen et al., 2016] post-tensioning loads are not applied in the global analyses, possible restraint forces and bending moments are considered to be of no relevance for the design at this stage.

6.1 Static Analyses

The reference system convention used along all this thesis project is the one in Fig. 6.1.

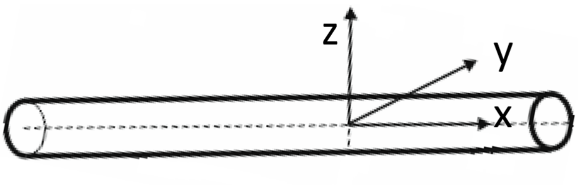

Figure 6.1: Global reference system axes direction

A global static analysis is performed in order to check the effects of the buoyancy weight ratio (BWR) in the different models, and control whether the structural requirement in section 4.2 are verified or not. The models are compared in terms of displacement and internal forces distributions. The drag and inertia forces are introduced by the Morison equation (3.3.2). A detailed analysis set up is described in section 5.3.4.

For the tether stabilize SFTs are adopted different BWR than for the tunnel configuration anchored only at the abutments. This is done in order to avoid slacking phenomena in the tethers.

6.1.1 Displacements

In this section the relative displacement in the $y-direction$ and $z-direction$ are reported. In order to have a clear comparison between the models with different alignment, the displacement are measured with respect to the undeformed configuration.

In Figs. 6.2a to 6.2d are illustrated the horizontal displacement along the longitudinal coordinate of the tunnel varying the BWR.

From Figs. 6.2a and 6.2b, it can be noticed that the horizontal displacement in the straight tunnel configuration (model D) is not influenced by the BWR, while the BWR influences the horizontal displacement in the other models with a double curvature (models A, B and C). This fact is broadly analyzed and explained in section 6.4.2, where it is concluded that mode D acts as a 2D model in the static analysis, therefore vertical actions does not influences horizontal displacements.

It is reminded that the horizontal equivalent static forces are applied in the negative $y-direction$. However models A and C displace in the positive $y-direction$ for some BWRs, as shown in Figs. 6.2a and 6.2c. This occurs since models A and C are less stiffer in the vertical direction than models C and D. This can be noticed also by the fact that horizontal displacements in models A and C are largely dependent on the BWR. It is obvious in Figs. 6.2a and 6.2c, that the static horizontal displacements are governed by vertical actions for models A and C.

On the contrary, horizontal displacements in Figs. 6.2b and 6.2d, are slightly dependent on the BWR and they displace in the applied horizontal forces direction. However model B shows larger deflection in the horizontal plane than model C, this is not in agreement with the conceptual design phase, where a 2D static analysis is performed, and it was concluded that the arch configuration is stiffer that the straight one. This occurs due to the fact that inclined elements in a 3D model show coupled displacements if the global reference system is adopted.

The larger horizontal displacement is located at mid-span for all the models. All the models satisfy the structural requirement regarding the maximum horizontal deflection allowed, which is equal to $\delta max = L/200 = 2.5m$.

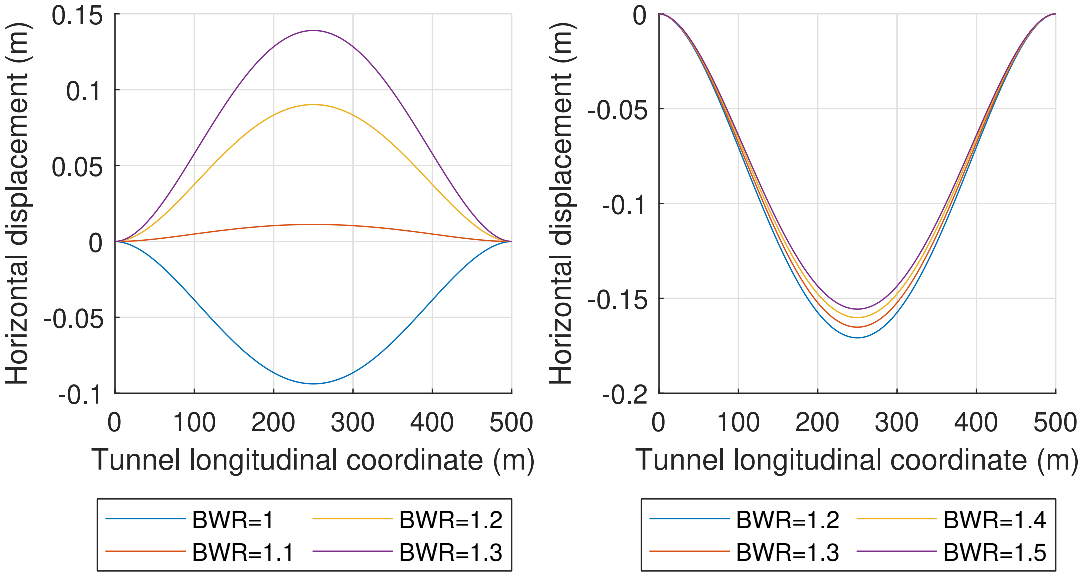

(a) Model A

(b) Model B

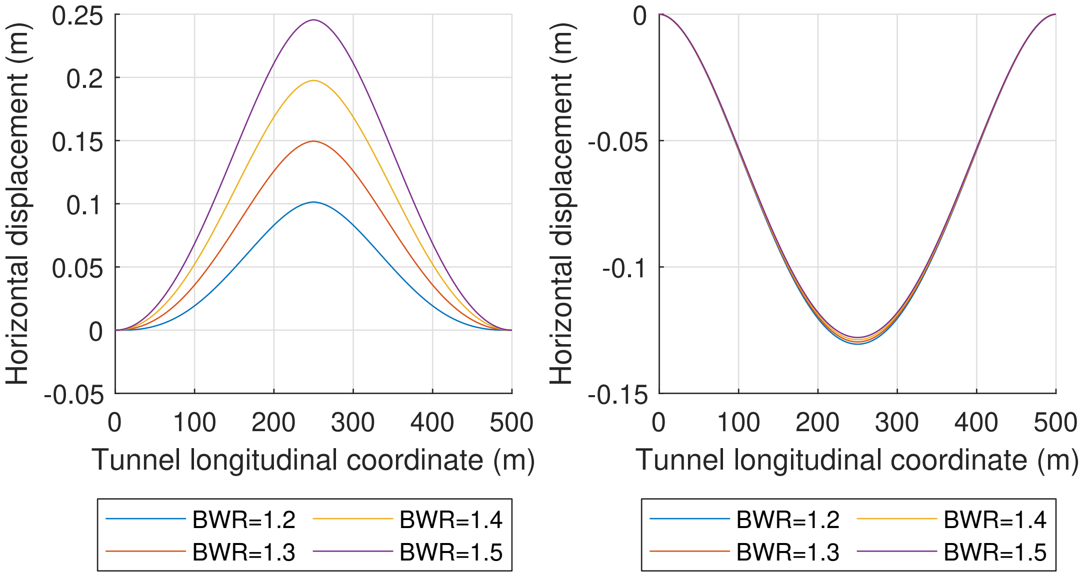

(c) Model C

(d) Model D

Figure 6.2: Horizontal displacement, models A, B, C, D, static analysis

In Figs. 6.3a to 6.3d, are reported the vertical displacements along the tunnel longitudinal coordinate, varying the BWR.

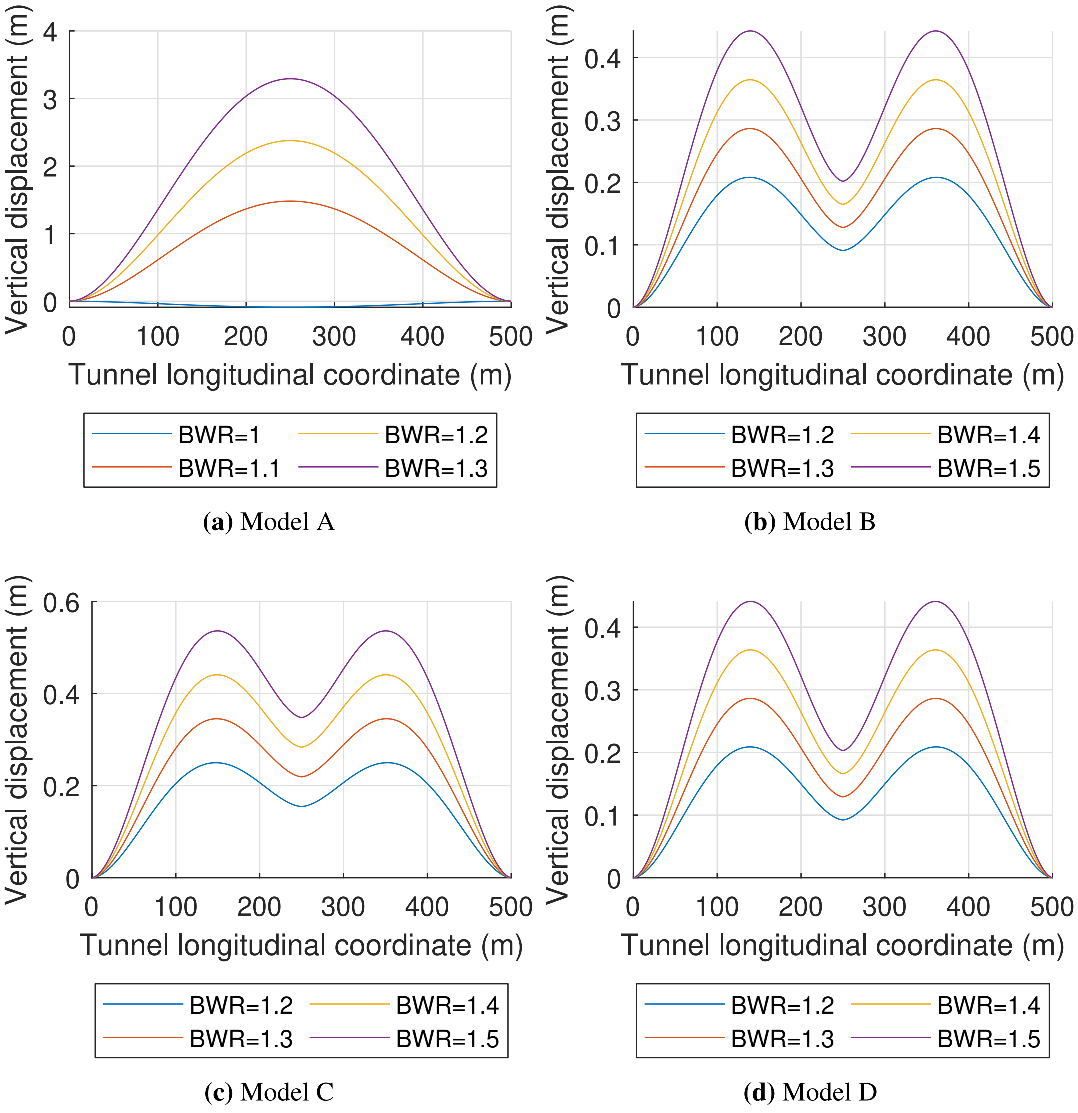

(a) Model A **(b)** Model B

(c) Model C **(d)** Model D

Figure 6.3: Vertical displacement, models A, B, C, D, static analysis

Model A, Fig. 6.3a, is the one showing larger vertical displacements, for analogous BWR, due to the fact that no additional supports are added in the tunnel span. Moreover, it can be seen in Fig. 6.3a, that for a BWR=1, the vertical displacements are negative, this is caused by the traffic load applied as an equivalent static load.

Models, B and D, Figs. 6.3c and 6.3d, have both a couple of vertical tethers at the mid-span, and they show similar displacement, even though they have a different tunnel alignment. Model C, Fig. 6.3c, has a slightly higher vertical displacement than model B. This was expected, since model C has only one vertical tether, while the other tether is inclined of 45. Model A has the larger vertical displacement at mid-span, while models B, C and D have the larger vertical displacement amplitude at quarter-span.

Finally, it can be concluded, from static analysis displacements results, that the double arch configuration does not show obvious advantages with respect to the straight configuration. However, it is not completely proper to compare the results in the same reference system, being the vertical and horizontal displacements coupled in the double arch configuration.

The maximum vertical displacement allowable, in agreement with the structural requirement is $1.43m$ for model A and $0.71m$ for models B, C and D. In model A the maximum vertical displacement is overcomed if a BWR higher than 1.1 is adopted. The maximum allowable vertical displacement criteria is fulfilled in models B, C and D, for all the BWRs tested.

6.1.2 Internal Forces and Moments

In Figs. 6.4a to 6.4d are shown the horizontal shear distributions along the $y - axis$.

The horizontal shear distribution in model A, Fig. 6.4a, is largely dependent on vertical forces, and if a BWR=1.1 is adopted the shear internal forces are remarkably reduced. The shear distribution S_y in model A tends to be linear for high BWR, while for a BWR=1 the horizontal actions are predominant and the shear distribution has an opposite trend.

In model B, Fig. 6.4b, the shear distribution is antisymmetric, slightly dependent on the BWR, with the highest amplitude at the end sections. In model C, Fig. 6.4c, the shear amplitude has a peak at the mid-span and the minimum amplitude is at the end sections. This is caused by the inclined tether ad mid-span, present in model C.

The horizontal shear distribution in model D, Fig. 6.4d, is linearly distributed, antisymmetric and independent from the BWR.

The vertical shear distributions varying the BWR, for all the models, are illustrated in Figs. 6.5a to 6.5d.

It can be noticed, in Fig. 6.5a, that in model A the vertical shear force is highly dependent on the BWR, and it tends to be negligible for a BWR=1 where the only vertical forces are due to traffic.

Models B, C and D, Figs. 6.5b to 6.5d, have a quite similar vertical shear distribution and amplitudes. In the tether stabilized models, the vertical shear distribution is antisymmetric with a discontinuity at the mid-span.

The bending moment distribution around the $y - axis$ is reported in Figs. 6.6a to 6.6d.

The bending moment distribution around the $y - axis$ in model A, Fig. 6.6a, is highly

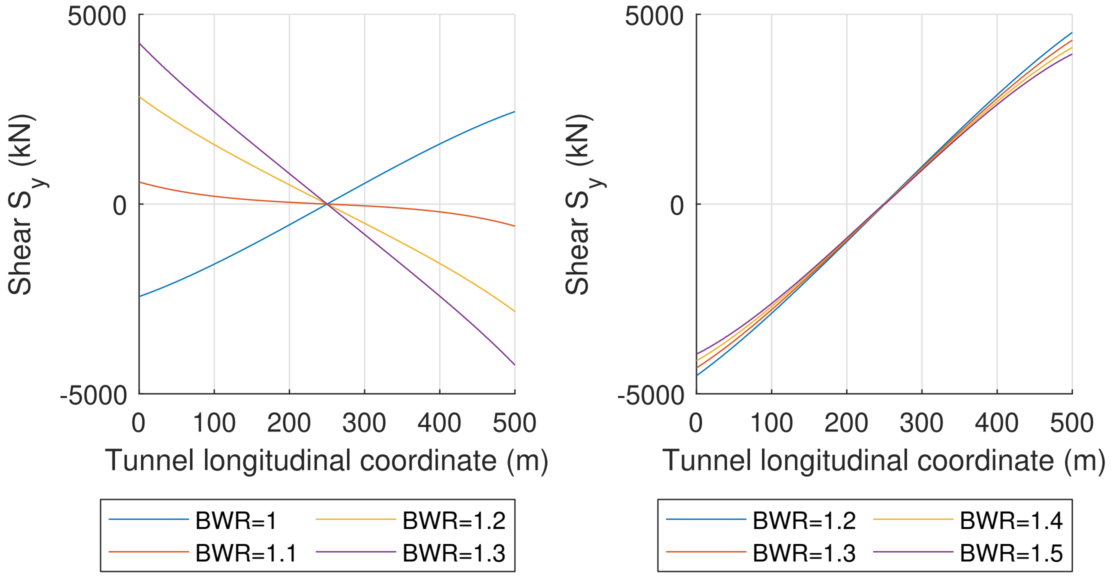

(a) Model A

(b) Model B

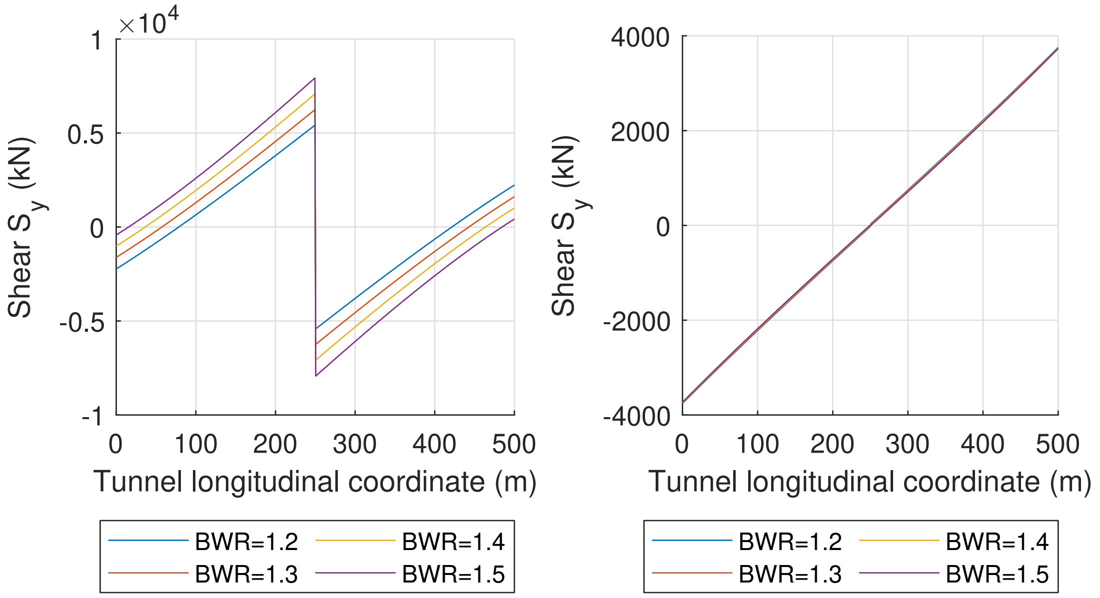

(c) Model C

(d) Model D

Figure 6.4: Horizontal shear distribution, models A, B, C, D, static analysis

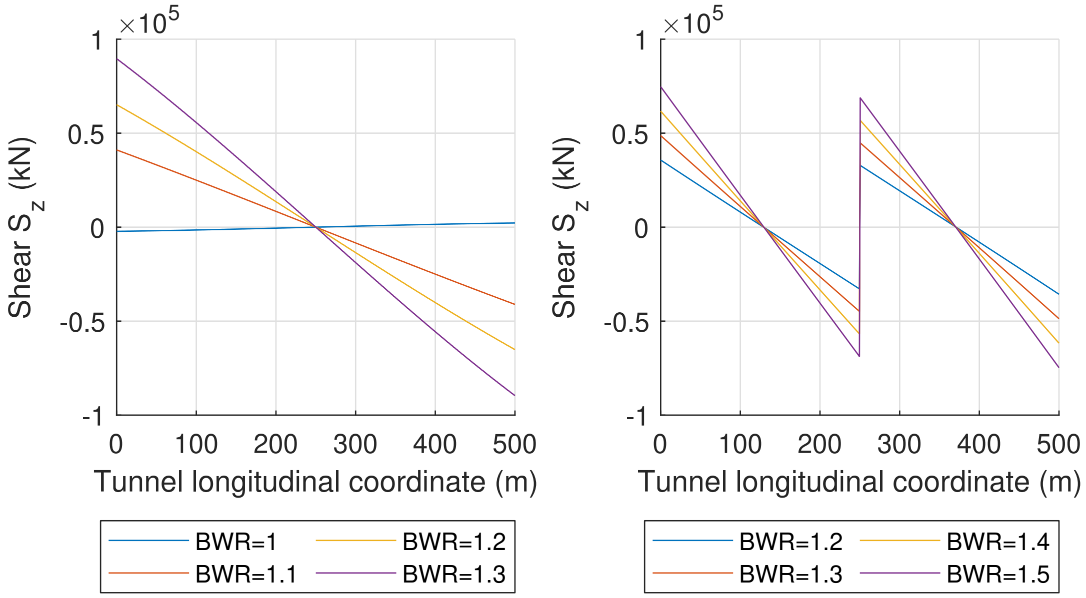

(a) Model A **(b)** Model B

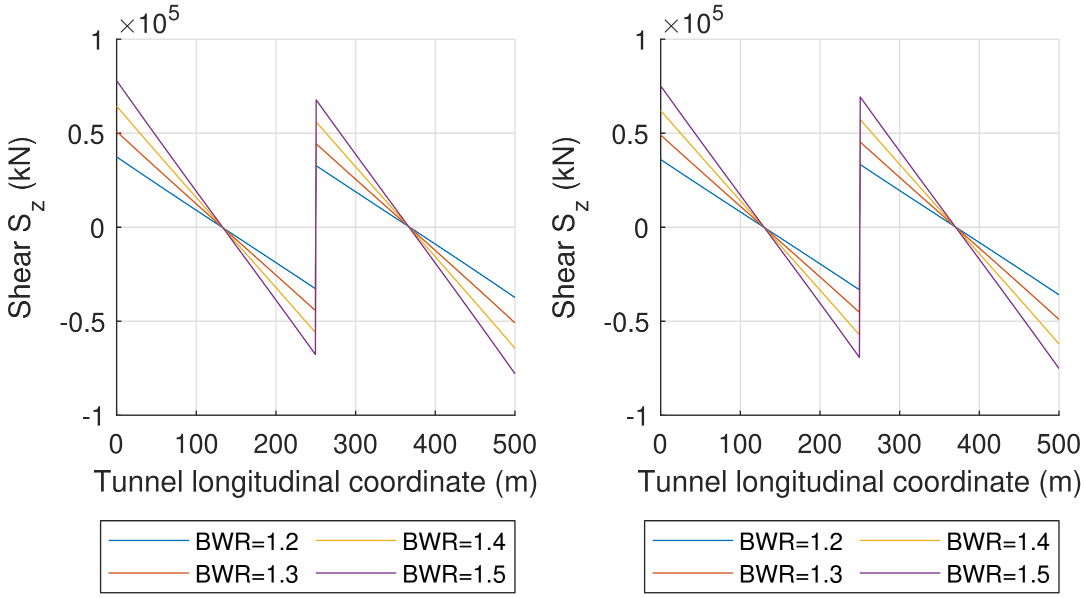

(c) Model C **(d)** Model D

Figure 6.5: Vertical shear distribution, models A, B, C, D, static analysis

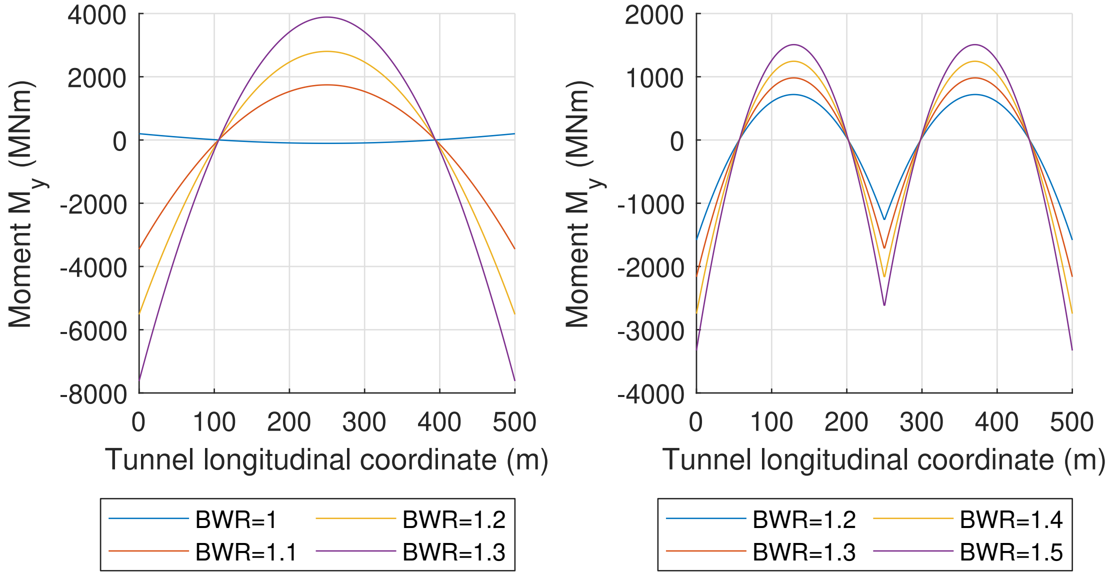

(a) Model A **(b)** Model B

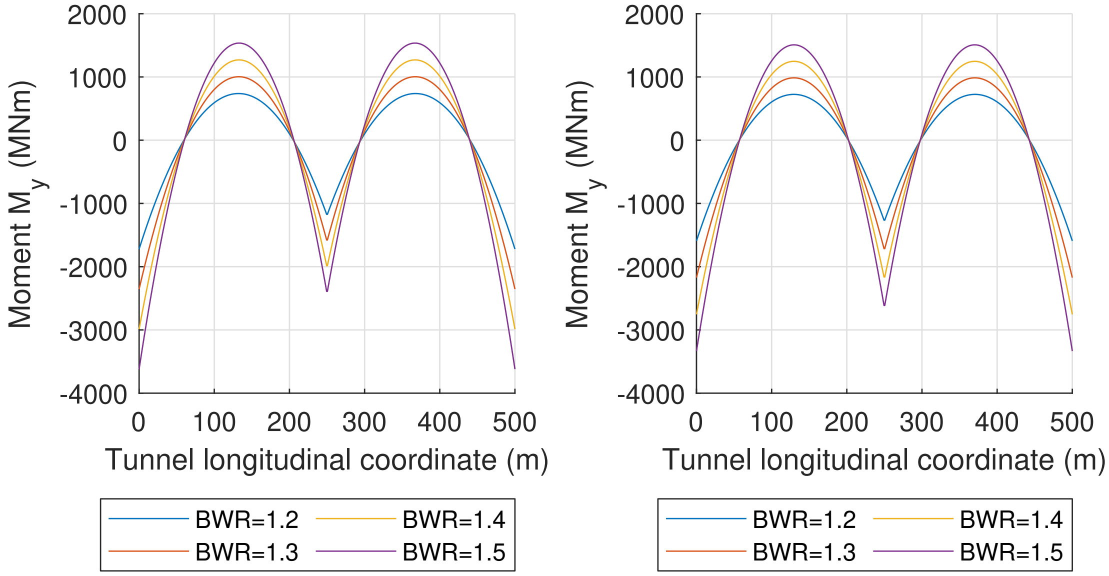

(c) Model C **(d)** Model D

Figure 6.6: Bending moment distribution around the $y - axis$, models A, B, C, D, static analysis

dependent on the BWR. In particular, at the end sections it ranges between $199MNm$ (BWR= 1) to $7622MNm$ (BWR=1.3).

In models B, C and D, Figs. 6.6b to 6.6d, the bending moment distribution is symmetric with maximum positive values at quarter-span, and minimum negative values at the end sections. The bending moment M_y amplitudes in models B, C and D are similar.

Comparing model A with models B and C, in terms of bending moment M_y, it can be noticed that the amplitude of M_y is reduced of 70% at the end sections, considering a BWR of 1.3. This explain the effect of the couple of tethers that are included at mid-span in models B and C.

The bending moment distribution around the $z-axis$ for models A, B, C and D is illustrated in Figs. 6.7a to 6.7d, four BWRs are considered for each model.

The bending moment amplitude around the $z - axis$,in model A Fig. 6.7a, is mainly governed by the BWR. The M_y amplitude is dependent on the BWR in model C Fig. 6.7c, while is slightly less dependent on the BWR in models B and D, Figs. 6.7b and 6.7d.

In model A, Fig. 6.7a, the lowest M_z amplitude is founded when a BWR=1.1 is adopted. Models B and D,Figs. 6.7b and 6.7d, have a similar bending moment distribution with an absolute amplitude bending difference of $50MN$. The M_Z distribution in model C,Fig. 6.6c, shows a discontinuity point at mid-span, where an inclined tether is placed. The inclined tether, which act as a lateral support element, reduces the M_z amplitude at the end sections and it increases M_Z at mid-span.

6.1.3 Static Analysis Conclusions

Considering the double arch tunnel configuration, which is adopted in models A, B and C. The 3D static analysis performed in Abaqus, shows large difference in terms of displacement and internal forces, if compared to the 2D analytical solution performed in the conceptual design phase. This is due to the fact that applied vertical forces causes horizontal displacements and vice versa. Three dimensional analysis is therefore of paramount importance when the tunnel configuration is parabolic in both vertical and horizontal directions.

On the other hand, considering the straight tunnel configurations,the analytical 2D model and the 3D FEM show identical results in the horizontal direction. In the vertical direction the results are not comparable due to the fact that in the FEM are introduced two vertical tethers.

The arch configuration benefits founded in the 2D static analysis are not maintained in the 3D static analysis, where the straight tunnel configuration shows overall better results. The

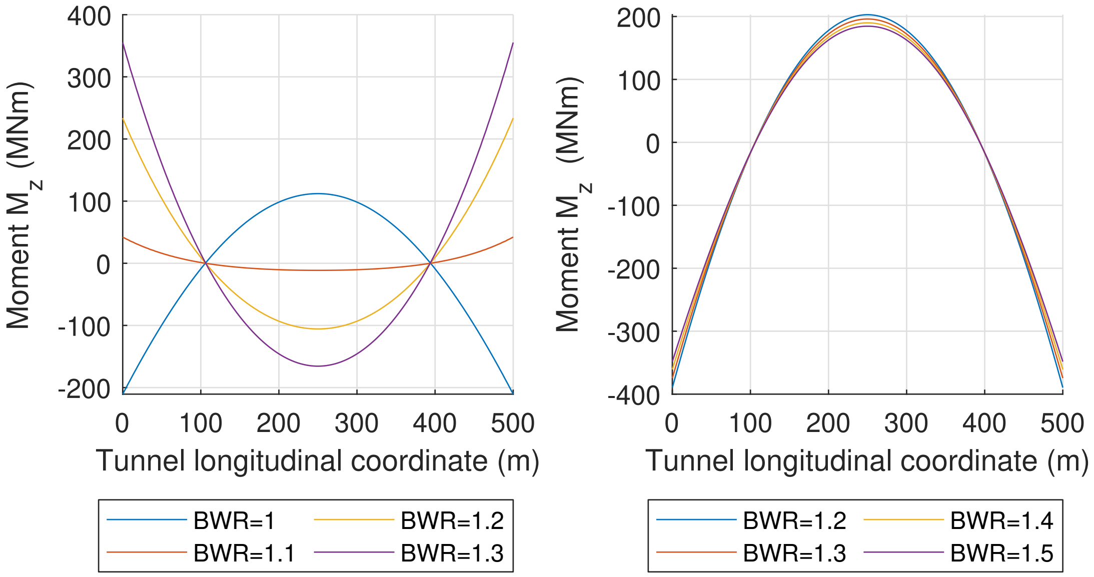

(a) Model A **(b)** Model B

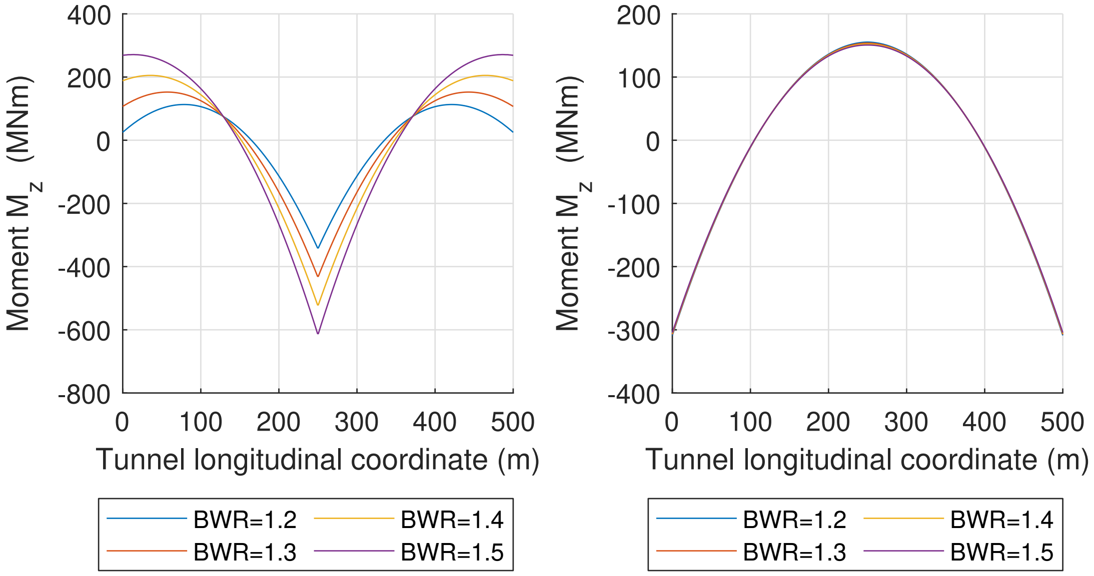

(c) Model C **(d)** Model D

Figure 6.7: Bending moment distribution around the $z-axis$, models A, B, C, D, static analysis

results are however reported for only one wave combination and four BWRs, and are hardly comparable in the same reference system.

Concluding, from the static analysis results, it can be seen that models A and C are generally more dependent on the BWR than models B and D. Moreover, the double arch configuration is less dependent on the horizontal actions than the straight tunnel configuration.

6.2 Modal Analysis

This section presents the results of the modal analysis in Abaqus/Aqua, explained in section 5.3.5, and the results obtained with the analytical method, explained in section 3.4.2. The estimated results for the Rayleigh damping coefficients are also included.

6.2.1 Simplified Method for Eigenfrequecnies

The analytical method described in section 3.4.2 is used in order to calculate the first two natural frequencies of the model. As previously reported, the method is valid only for a straight SFT configuration, therefore the method is used just for model D. The assumed first and second modal shapes ($n = 1, 2$) of equation (3.34) are printed in Figures 6.9a-6.9b.

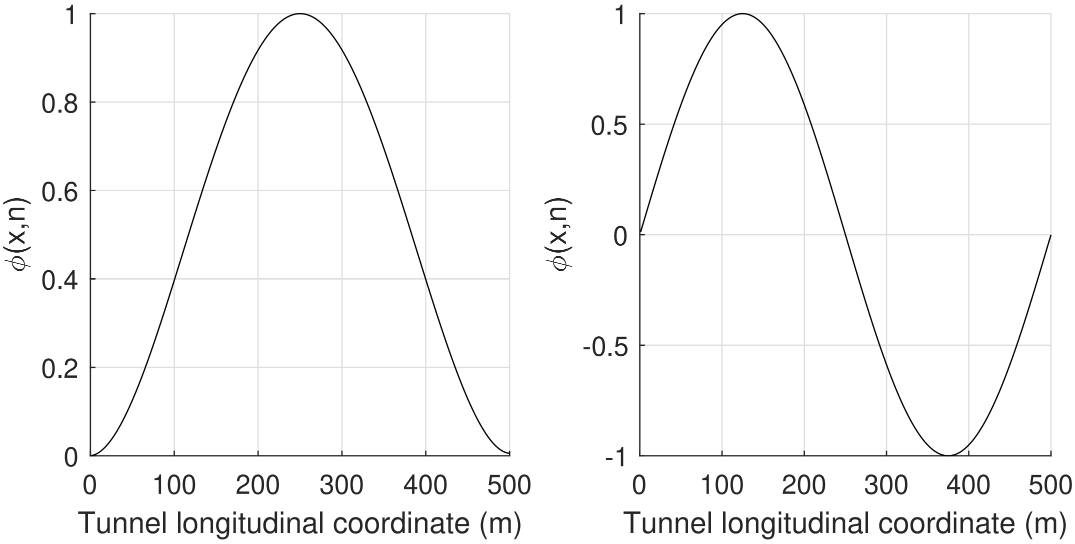

(a) 1^{st}Modal Shape **(b)** 2^{nd}Modal Shape

Figure 6.8: Assumed modal shapes for the straight SFT configuration

The analytical method, reported in a Matlab script, can be found in appendix A.2. The derived eigenfrequencies and natural periods are listed in table 6.1 .

Table 6.1: Analytical horizontal and vertical eigenfrequencies and periods for model D

Mode	Frequency (rad/s)	Period (s)
1^{st} horizontal	0.785	8.004
1^{st} vertical	1.469	4.277
2^{nd} horizontal	1.43	4.393
2^{nd} vertical	4.367	1.439

6.2.2 Modal Analysis in Abaqus

The modal analysis is preformed for each model, the analysis set up is described in section 5.3.5. The results in this section are reported for the last iteration, relative to the first cycle of the general scheme reported in Table 5.9.

All the tunnels are submerged at a depth of 40 m, and the following buoyancy weight ratios were considered during the modal analysis :

Table 6.2: Buoyancy weight ratio for models A,B,C,D during the modal analysis

	Model A	Model B	Model C	Model C
BWR	1.1	1.2	1.3	1.2

The natural frequencies and periods for all the models are reported in Tables 6.3,6.4. The symbols H and V indicates respectively horizontal and vertical modal shapes. This is reported just for the straight tunnel configuration (model D), due to the fact that the other models do not show a clear difference between vertical and horizontal modal shapes. The symbol T indicates the tether vibration dominated modes.

In this section, it is important to remember that the wave loading combination considered have a significant natural period that ranges between 5.5 to 17 second, which is terms of frequencies goes from $0.369 rad/s$ to $1.142 rad/s$. It can be noticed that model A has the first two natural periods in the wave loading range of frequencies, while the other models have just the first natural period in this range.

Considering the JONSWAP wave spectrum, it can be seen that the spectral density ranges between $0.25 rad/s$ to $2 rad/s$, therefore in model C, also the second and third mode are relevant. In Figs. 6.10a and 6.10l are reported the firsts six modal shapes in the horizontal and vertical plane. The modal shapes for models B, C and D are illustrated in Appendix B.1.

It can be noticed in Figs. 6.10a and 6.10l, that the modal shapes are generally mixed modes, and there is not a clear difference between vertical and horizontal modes. Modes number 3 and 4 are antisymmetric, while modes 1, 2, 5 and 6 are symmetric. The modal shapes are normalized with respect to the displacement, therefore the magnitude of displacement

Table 6.3: Eigenfrequencies and Eigenperiods of the first 20 modes for model A and B

	Model A		Model B	
Mode	frequency (rad/s)	period (s)	frequency (rad/s)	period (s)
1	0.806	7.796	0.996	6.308
2	1.016	6.184	2.215	2.837
3	2.214	2.838	2.285 T	2.75
4	2.215	2.837	2.297	2.735
5	4.299	1.462	2.33	2.697
6	4.312	1.457	2.725	2.306
7	7.006	0.897	2.78 T	2.26
8	7.007	0.897	2.785 T	2.256
9	10.29	0.611	4.315	1.456
10	10.293	0.61	5.752	1.092
11	13.801	0.455	5.832 T	1.077
12	14.094	0.446	5.836 T	1.077
13	14.096	0.446	6.779 T	0.927
14	18.369	0.342	6.801 T	0.924
15	18.369	0.342	7.02	0.895
16	21.352	0.294	7.025	0.894
17	23.056	0.273	10.284	0.611
18	23.063	0.272	10.91	0.576
19	27.564	0.228	11.091 T	0.567
20	28.106	0.224	11.094 T	0.566

in Figs. 6.10a and 6.10l is meaningless.

6.2.3 Effective Mass Participation

The effective mass participation values for the four models are here reported. One way of checking that a sufficient number of eigenvalues has been extracted is to check the total effective mass in each degree of freedom, which indicates the portion of mass active for each degree of freedom. The theory and the importance of the effective mass analysis are listed in section 3.4.1.

Ideally the sum of the effective masses of each mode for each direction should be at least 90% of the total mass. The mass of the constrained nodes should not be taken into account in the total mass. In Table 6.5 is listed the effective mass, which indicates the amount of mass active in each degree of freedom, for any mode. The effective mass in the $x - direction$ is

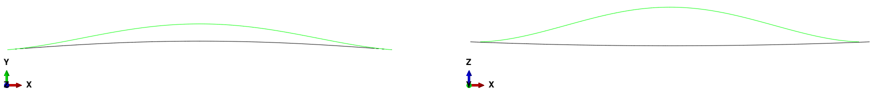

(a) Mode 1 horizontal projection **(b)** Mode 1 vertical projection

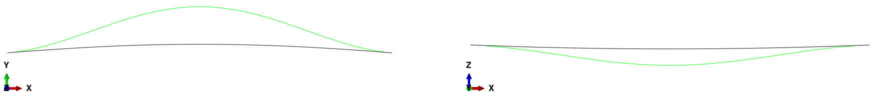

(c) Mode 2 horizontal projection **(d)** Mode 2 vertical projection

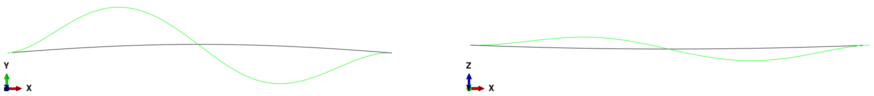

(e) Mode 3 horizontal projection **(f)** Mode 3 vertical projection

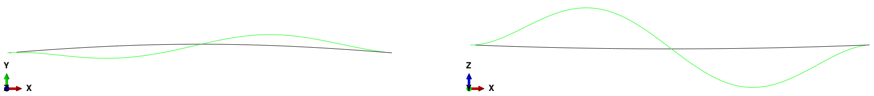

(g) Mode 4 horizontal projection **(h)** Mode 4 vertical projection

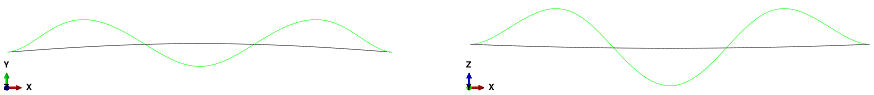

(i) Mode 5 horizontal projection **(j)** Mode 5 vertical projection

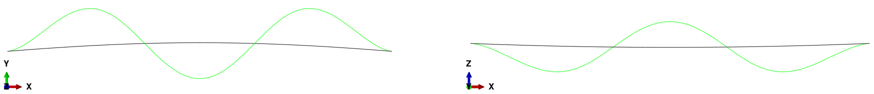

(k) Mode 6 horizontal projection **(l)** Mode 6 vertical projection

Figure 6.9: Modal shapes illustration of first 6 modes, Model A

Table 6.4: Eigenfrequencies and Eigenperiods of the first 20 modes for model C and D

	Model C		Model D	
Mode	frequency (rad/s)	period (s)	frequency (rad/s)	period (s)
1	1.023 T	6.142	0.831 H	7.561
2	1.313	4.785	2.228 V	2.82
3	1.703	3.689	2.247 H	2.796
4	2.234	2.813	2.308 T	2.722
5	2.235	2.811	2.328 T	2.699
6	2.628T	2.391	2.725 V	2.306
7	2.669	2.354	2.794 T	2.249
8	2.778T	2.262	2.805 T	2.24
9	3.143T	1.999	4.339 H	1.448
10	3.639T	1.727	5.781 V	1.087
11	4.503	1.395	5.87 T	1.07
12	5.248T	1.197	5.877 T	1.069
13	5.427	1.158	6.798 T	0.924
14	6.287	0.999	6.846 T	0.918
15	6.53T	0.962	7.067 H	0.889
16	7.029	0.894	7.074 V	0.888
17	7.029	0.894	10.346 H	0.607
18	7.871	0.798	10.970 V	0.573
19	8.782T	0.715	11.158 T	0.563
20	10.28	0.611	11.165 T	0.563

not significant since the loading is applied in directions y and z.

The added mass has to be included in the total mass of the structure, equation (3.44). The added mass with respect the cross section and the added mass coefficient previously estimated is

$$m_a = 2.210 \times 10^5 (kg/m) \tag{6.1}$$

In the models there are four end sections constrained, two tunnel pipe sections and two pinned connection between the tethers and the sea bed. The amount of tether mass constrained is negligible. As a result the amount of constrained mass is analogous in all the models and it correspond to

$$m_{constrained} = 8.271 \times 10^4 (kg) \tag{6.2}$$

The total mass to be considered in the analysis is so

$$m_{tot} = m_{structure} + m_a \times L - m_{constrained} \tag{6.3}$$

The effective mass participation obtained in Abaqus for the four models is reported in Table 6.5.

Table 6.5: Effective mass participation results from Abaqus

	Model A		Model B		Model C		Model D	
(/)	$(kg * 10^5)$							
mode	m_y	m_z	m_y	m_z	m_y	m_z	m_y	m_z
1	75	689	770	1	0	0	776	0
2	683	73	0	0	245	20	0	0
3	0	0	0	0	472	92	0	0
4	0	0	0	0	0	0	0	0
5	57	92	0	0	0	0	0	0
6	97	58	0	878	113	781	0	876
7	0	0	0	10	0	0	0	13
8	0	0	0	0	0	0	0	0
9	27	34	156	0	1	0	150	0
10	35	27	0	0	2	0	0	0
11	0	0	0	0	89	9	0	0
12	0	0	0	0	0	0	0	0
13	0	0	0	0	0	1	0	0
14	15	19	0	0	0	0	0	0
15	19	15	0	0	0	0	0	0
16	0	0	0	0	0	0	0	0
17	0	0	62	0	0	0	62	0
18	0	0	0	98	0	0	0	98
19	0	0	0	0	0	0	0	0
20	8	13	0	0	17	4	0	0
$\sum m_{x,y}$	1016	1020	988	987	939	907	988	987
$m_{structure}$	466		472		473		472	
m_{tot}	1104		1110		1112		1120	
$\frac{\sum m_{x,y}}{m_{tot}}\%$	92	93	89	89	84	82	89	89

In model A the sum of the effective masses in each direction covers more than 90% of the total mass, therefore the first twenty modes of the structure can be considered the significant modes. This is not valid for the other models, where in order to have 90% mass participation for all directions, a number of 25 significant modes is required.

The effective mass provides a measure of the energy contained within each resonant mode. A mode with a large effective mass participation factor (3.32) is usually a significant contributor to the dynamic response of a system.

For a antisymmetric mode, the center of gravity experiences no movement in the direction of symmetry. So as a percentage of effective mass participating in the mode, the solution will show zero. This can be noted in modes 3 and 4 of model A (Figs. 6.10e and 6.10g), where m_y and m_z (Table 6.5) are both null.

6.2.4 Damping Parameter

The damping parameters α and β are found with the procedure explained in section 3.4.4. They are necessary for formulate the damping matrix of the system with Rayleigh procedure.

$$[C] = \alpha[M] + \beta[K] \tag{6.4}$$

The method is a step by step method, and it requires the assumption of the damping ratios of the first and last significant modes. These are reported in section 5.3.6. The step by step procedure is reported just for model A, while for the other models just the results are herein reported.

From the previous section has been derived that the number of significant modes in model A is $m = 20$. In order to apply the procedure a number of $2.5m = 50$ modes has to be extracted, which corresponds to the full range approximation. The parameters for the three different approximations are given in Table 6.6.

Table 6.6: Damping parameters with three different approximation methods

Parameter	m$^{th}mode$	full range	average data
α	0.012445	0.01270	0.01257
β	6.9582e-04	3.0875e-04	5.0229e-04

After calculating the coefficients, the damping ratio values for each approximation are calculated and plotted together together with the linearized damping ratio, Fig. 6.10.

It is suggested in this method to select the damping curve that best approximate the linear damping trend within the significant modes. In this case, it can be notice from Fig. 6.10, that the full range approximation method is the one which best approximate the linear damping trend.

The stiffness related and mass related damping ratios curves for the full approximation

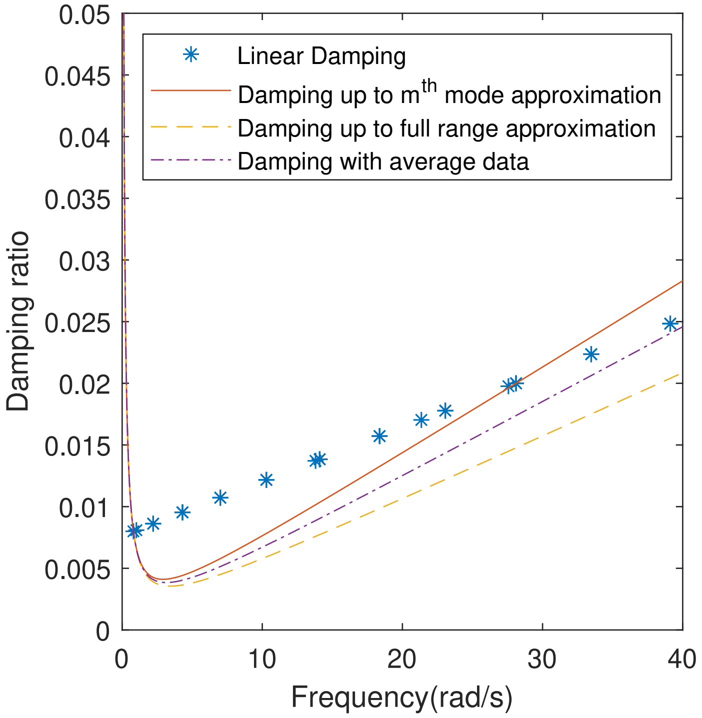

Figure 6.10: Rayleigh damping ratio with three different approximation methods, Model A

method are illustrated in Fig. 6.11.

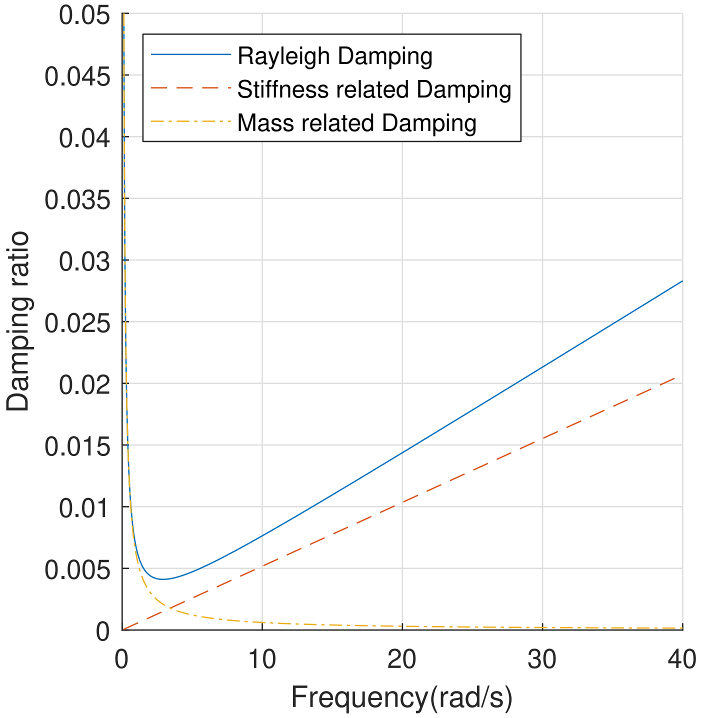

Figure 6.11: Rayleigh damping ratio curve, model A

The Rayleigh damping curve is the sum of the stiffness related damping and the mass related damping, in agreement with equation (6.4). It can be noticed, in Fig. 6.11, that in model A for low frequencies, in the range of the swell and wind waves, the system damping is mostly related to the mass of the system.

The Rayleigh damping parameters determined with the same procedure for each model are given in Table 6.7 . This values are used in the global dynamic analysis of the SFTs under harmonic and irregular wave loading.

Table 6.7: Rayleigh damping parameters for the models A, B, C and D

Parameter	Model A	Model B	Model C	Model D
α	0.01270	0.009316	0.005789	0.009063
β	0.0003088	0.006673	0.01011	0.006129

From the results given in Table 6.7, it can be noticed that the multiplier α, related to the mass, is lower than the multiplier β, related to the stiffness, for model C. Whereas for models A, B and D α is lower than β.

Although the assumption that the damping is proportional to the mass and stiffness matrices has no rigorous physical basis, in practice the damping distribution rarely is known in sufficient detail to warrant any other more complicated model. In general, this model ceases to be reliable for heavily damped systems; that is, above approximately 10% of critical damping. In the models analyzed in this thesis the damping is well below 10%, therefore the Rayleigh damping is adopted.

6.3 Regular Wave Dynamic Analysis

In this section the results from the harmonic wave analysis described in sections 3.5 and 5.3.7 are included. In order to compute a conservative harmonic wave analysis, comparable with an irregular wave analysis, the wave significant period is reduced by 10% and the wave height is increased by 90%. Moreover, the wave direction is assumed constant and perpendicular to the tunnel longitudinal axis. The design wave properties, used for the harmonic wave state are reported in section 5.3.2.

The purpose of this analysis is to verify whether the response fulfill the structural requirements 4.2, and compare the responses of the different models. The time series responses are reported for some significant tunnel sections, and tables with maximum and minimum values are present in each section. An analysis period of $150s$ turned out to be sufficiently long for all the models.

The buoyancy weight ratio values coincide with the ones adopted during the modal analysis. The models are herein compared in terms of displacement, accelerations, bending moment and tether axial forces.

The dynamic problem analyzed is non linear, then theoretically steady state response might not occur. However, the the structures analyzed in this thesis are weakly non linear, therefore a steady condition can be observed in the response plots.

6.3.1 Displacements

Tunnels responses in terms of vertical (z), transversal (y) displacements are herein reported. Two locations along the tunnel axis have been considered, the tunnel mid-span and the quarter -span. The structure is symmetric, under symmetric loading, therefore just one point is examined at quarter-span.

Horizontal displacement

The horizontal displacements time series at mid-span ($x = 0.5L$) and quarter-span ($x = 0.25L$), for models A, B, C and D are illustrated in Figs. 6.12a to 6.12d. The red triangles, in the time series, indicate the maximum absolute values.

It can be noticed in Figs. 6.12a to 6.12d, that very smooth time series are obtained for all the models. Clearly narrow banded, dominated by harmonic components with period approximately between $15 - 16s$, which correspond with the swell waves period.

The response can be fairly assumed steady state in models B, C and D after $60s$, while in model A it can be assumed steady state after $90s$. This assumptions can be made because the dynamic problem is weakly non linear. The double arch configuration Figs. 6.12a to 6.12c, shows smaller oscillation amplitudes than the straight configuration Fig. 6.12d, even in the case where no tether are used Fig. 6.12a.

In model C, Fig. 6.12c, thanks to the inclined tether, the structure oscillates always in the positive $y - direction$, even thought the wave loading and currents are applied on the negative $y - direction$.

Comparing model B with model A, it can be concluded that the vertical tethers, for a double curvature configuration, do not reduces the horizontal displacements. In particular, the horizontal displacements in model B are reduced at quarter-span but amplified at mid-span.

In Table 6.8 are reported the maximum and minimum horizontal displacements, obtained during the harmonic wave analysis for the four models.

It can be noticed in Table 6.8, that all the models satisfy the structural requirement regarding the maximum horizontal displacement allowable. However, other wave load combinations should be considered. The aim of this section is to compare the four models under the same actions.

Model D is the one with the highest absolute displacement both at mid-span and quarter-span. Model C has smaller relative displacement at quarter-span than the other models, and model A shows the smallest relative displacement at mid-span in Table 6.8.

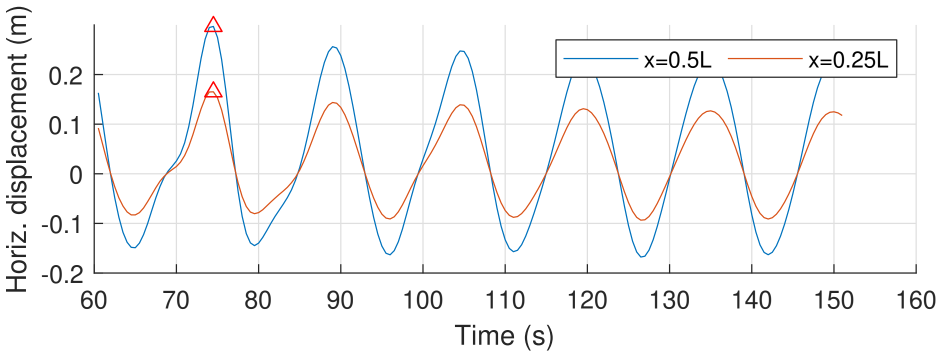

(a) Model A

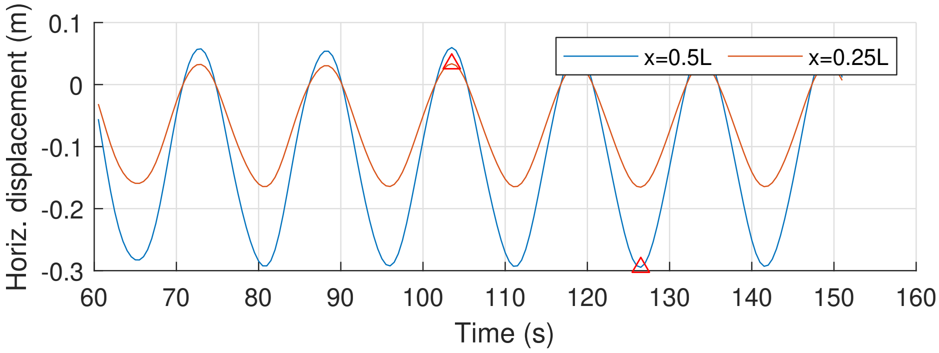

(b) Model B

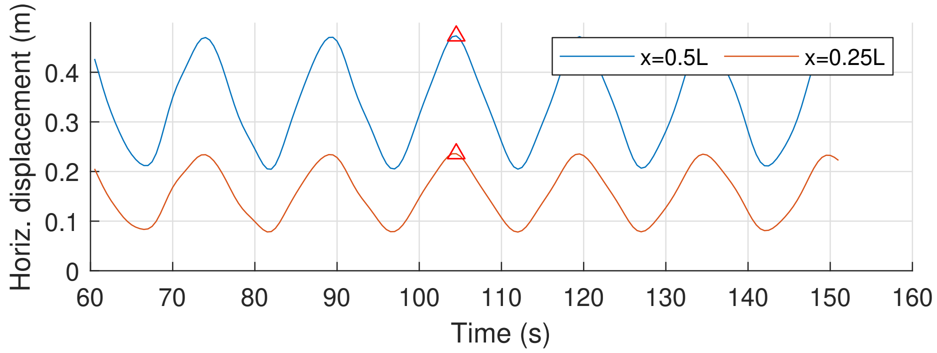

(c) Model C

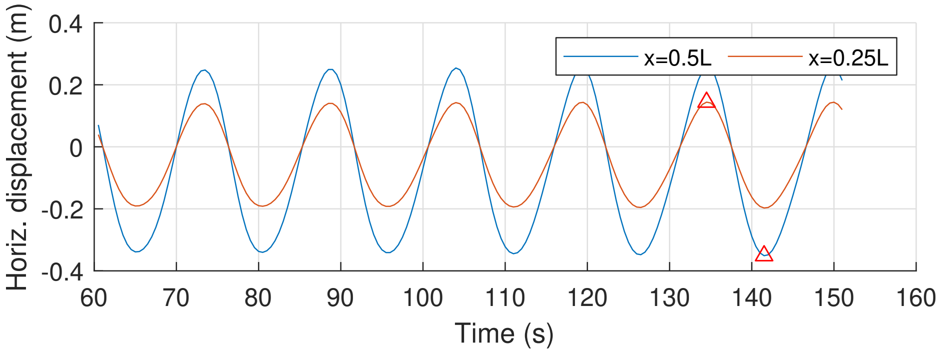

(d) Model D

Figure 6.12: Horizontal displacements time series at mid-span and quarter-span, models A, B, C and D, harmonic wave analysis

Table 6.8: Maximum and minimum horizontal displacements results. Harmonic wave analysis, load combination (a), models A, B, C, D

Model	A		B		C		D	
Position	min (m)	max (m)	min (m)	max (m)	min (m)	max (m)	min (m)	max (m)
x=0.25L	-0.09	0.17	-0.17	0.03	0.08	0.24	-0.2	0.14
x=0.5L	-0.17	0.3	-0.29	0.06	0.2	0.47	-0.35	0.26
δ_{Lim}	1.43		1.43		1.43		1.43	
Verified	yes	yes	yes	yes	yes	yes	yes	yes

Vertical displacements

The vertical displacement response for the four models under harmonic wave loading is shown in Figs. 6.13a to 6.13d.

Model A, which has no tethers, is the one showing the largest vertical displacements. Models B and D, both with a couple of vertical tethers, show very similar vertical displacements. Therefore there are no advantages in terms of vertical displacements in adopting a double arch configuration, with respect to the wave actions considered.

In Table 6.9 are listed the maximum and minimum vertical displacements, for all the models, under the wave load combination (a).

Table 6.9: Maximum and minimum vertical displacements results. Dynamic analysis, load combination (a), models A, B, C, D

Model	A		B		C		D	
Position	min (m)	max (m)	min (m)	max (m)	min (m)	max (m)	min (m)	max (m)
x=0.25L	0.43	0.99	0.15	0.21	0.45	0.6	0.15	0.21
x=0.5L	0.75	1.76	0.07	0.09	0.58	0.8	0.06	0.09
δ_{Lim}	1.43		0.71		0.71		0.71	
Verified	yes	no	yes	yes	yes	no	yes	yes

It emerges from the maximum absolute valued recorded during the time series, that models A and C do not satisfy the structural requirements. Models B and D have similar maximum and minimum displacements, and both satisfy the structural requirements.

Discrete Fourier Transform of Displacements

The theoretical background regarding the discrete Fourier transform (DFT), is reported in section 3.5.1. Frequency analysis of the response provides valuable information about structural vibration. The fast Fourier transform has been used, which is a computationally opti-

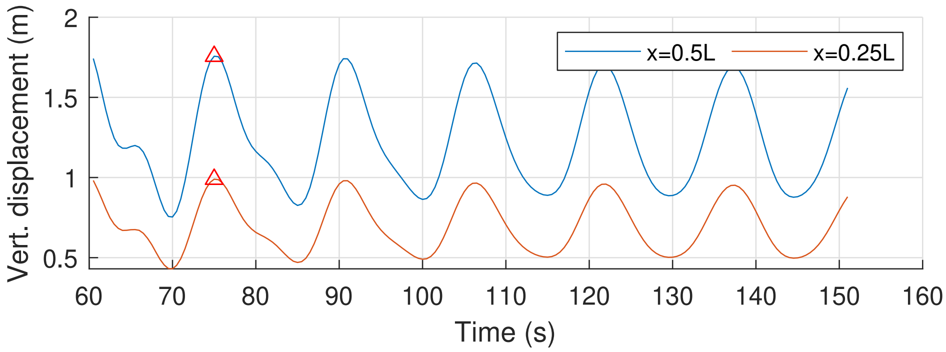

(a) Model A

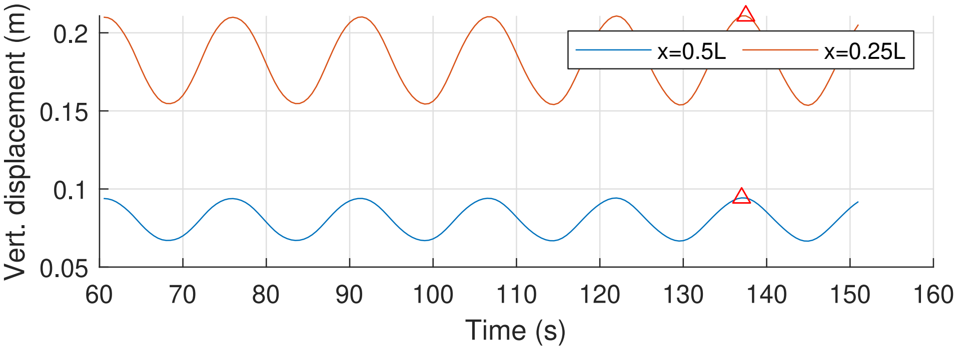

(b) Model B

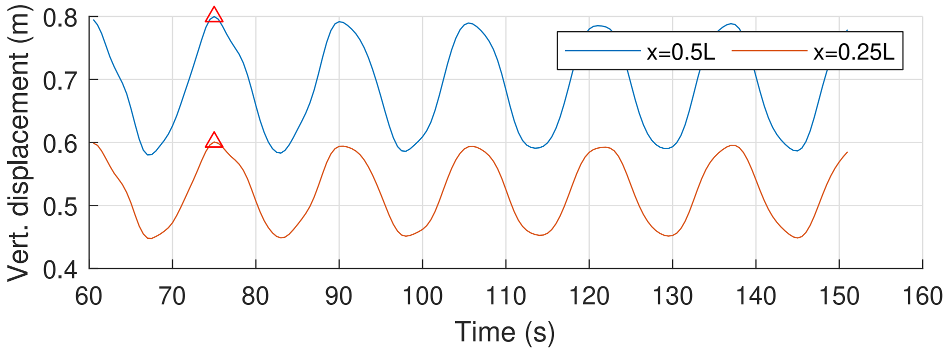

(c) Model C

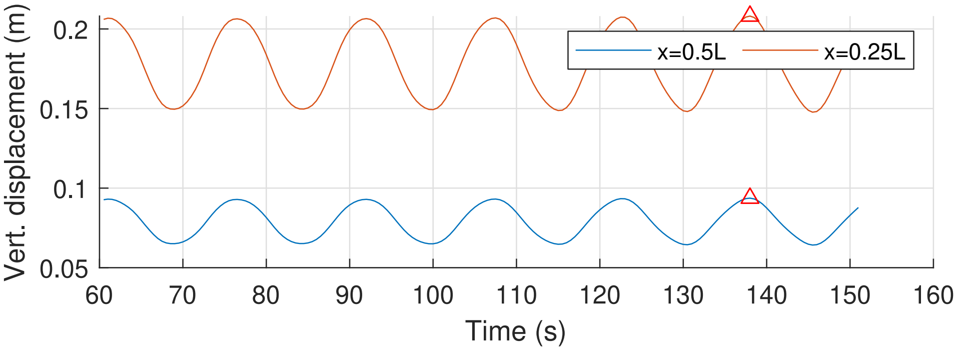

(d) Model D

Figure 6.13: Vertical displacements time series at mid-span and quarter-span, models A, B, C and D, harmonic wave analysis

mized version of the discrete Fourier transform.

The DFTs of the horizontal structural response at mid-span are illustrated in Figs. 6.14a to 6.14d, for all the models. It is reported only the absolute value, which is symmetric with respect the zero axis. On the left side are indicated with ω_w and ω_s respectively the wind and swell waves significant frequencies. On the right side are reported through vertical black lines the natural frequencies of the structure considered.

The frequency resolution of the DFT computed is

$$\Delta\omega = \frac{2\pi}{T} = 0.0418 rad/s \tag{6.5}$$

The smoothness of the DFT curve depend on the length of the discrete time series. The maximum frequency encaptured in the DFT is the so called Nyquist frequency

$$\omega_{max} = \frac{1}{2\Delta t} 2\pi = 62.83 rad/s \tag{6.6}$$

In the DFT the peak at zero frequency is the peak related to the static actions acting on the system.

From Fig. 6.14a, it is possible to notice that the horizontal structural response of model A is governed by the static action and the swell waves, while in a smaller extent by the first natural frequency. The same considerations hold for model B Fig. 6.14b and C Fig. 6.14d, with the only difference than in model B the static action is the most significant. In model C, Fig. 6.14c, the horizontal response is governed mainly by the static actions and less by the swell wave actions.

The DFT of the vertical displacement at mid-span for the four models ir reported n Figs. 6.15a to 6.15d. The vertical displacement in models B and D, is directly related to the tether elongation.

The vertical response of model A, Fig. 6.15a , is governed mainly by the static action and in a smaller extent by the swell waves frequency and the first resonant mode. In Fig. 6.15b, it can be noticed that model B vertical displacement is controlled by the swell wave action, and in a similar extent by the static action. In models C and D, Figs. 6.15c and 6.15d, the dynamic actions have a small influence on the vertical displacement at mid-span.

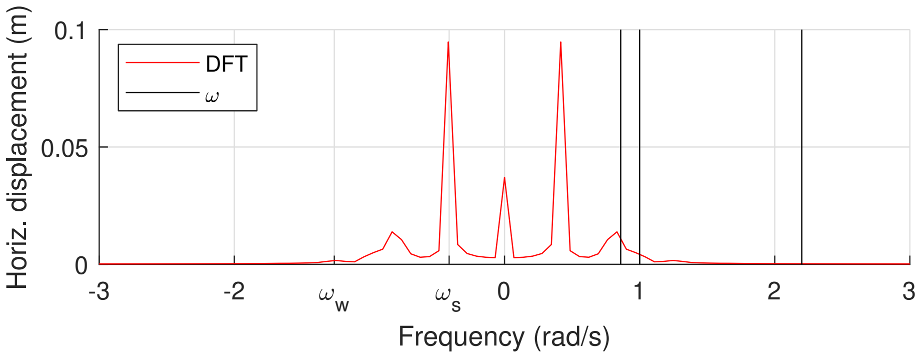

(a) Model A

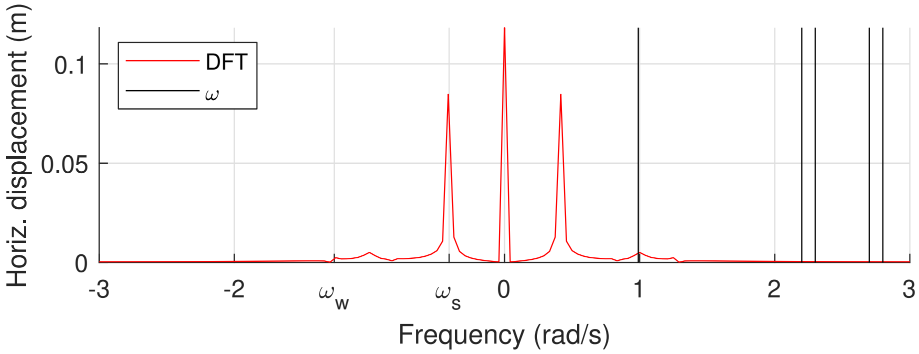

(b) Model B

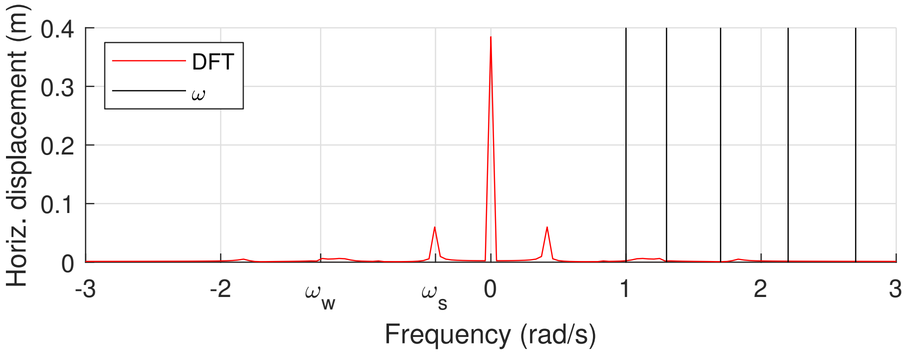

(c) Model C

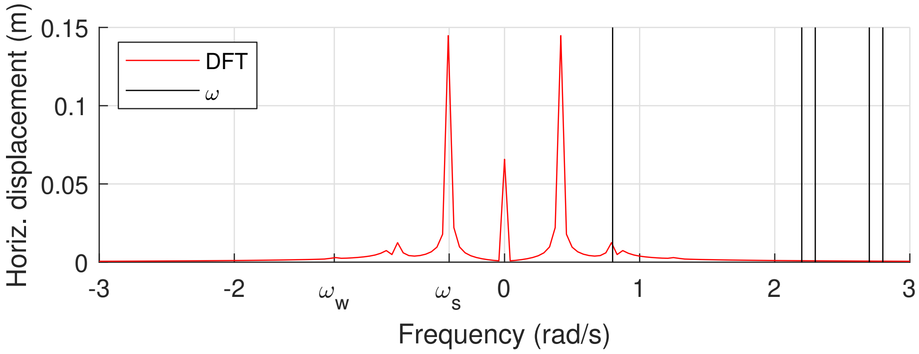

(d) Model D

Figure 6.14: DFT of the horizontal displacements at mid-span for models A, B, C, D

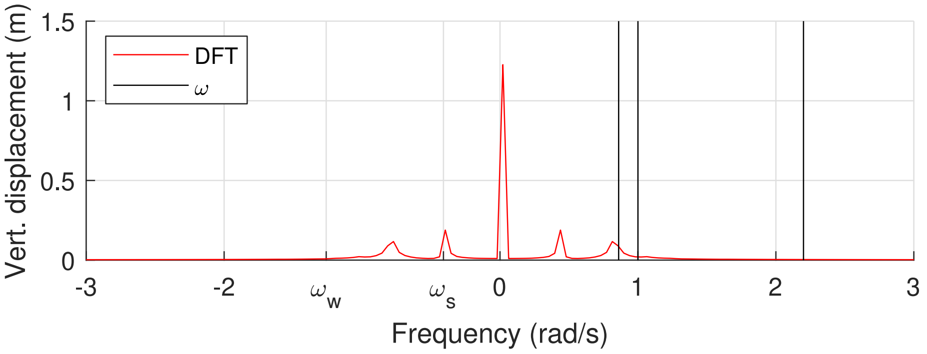

(a) Model A

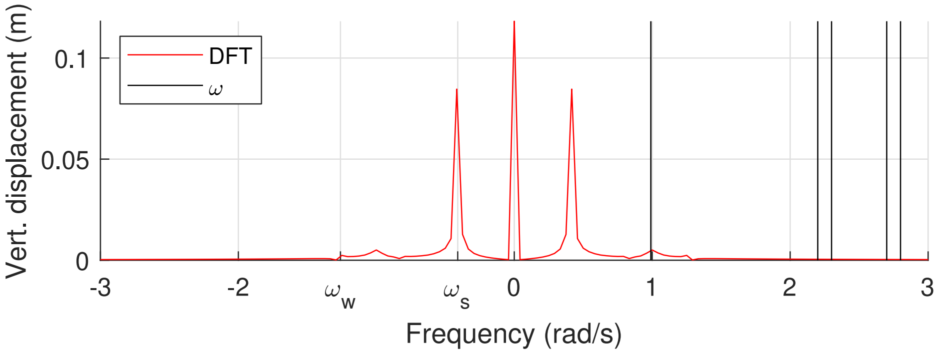

(b) Model B

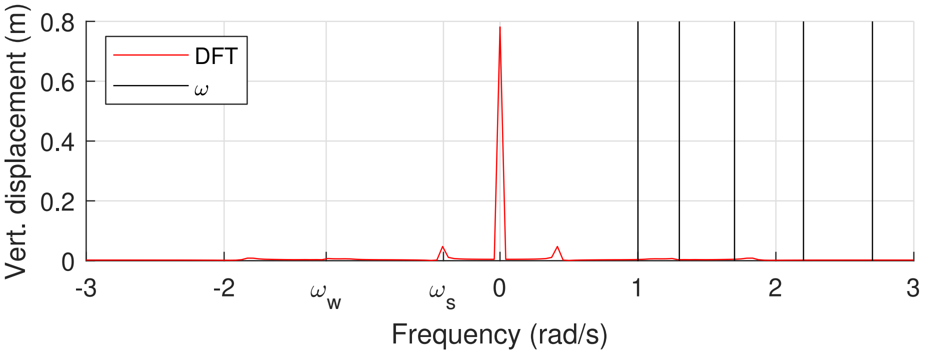

(c) Model C

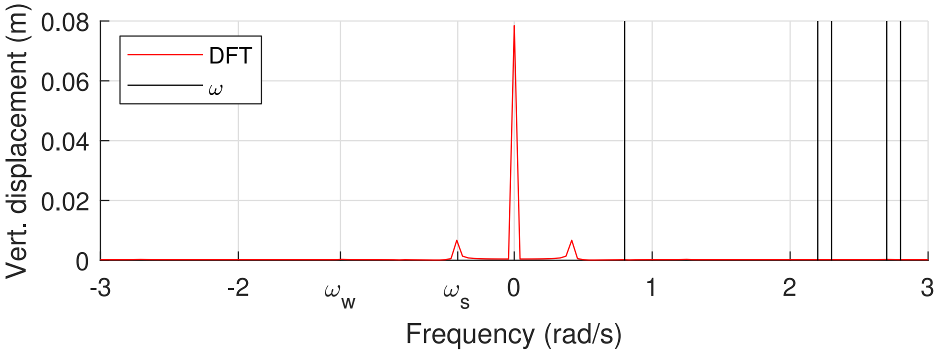

(d) Model D

Figure 6.15: DFT of the vertical displacements at mid-span for models A, B, C, D

6.3.2 Accelerations

Tunnel responses in terms of vertical (z) and transversal (y) accelerations are herein reported. Two locations along the tunnel longitudinal axis have been examined, the mid-span($x = 0.5L$) and the quarter-span ($x = 0.25L$).

Horizontal accelerations

The horizontal discrete accelerations time series at mid-span and quarter.span, for models A, B, C and D are illustrated in Figs. 6.16a to 6.16d. The red triangle, in the figures, indicates the maximum absolute value.

It can be noticed in Figs. 6.16a to 6.16d, that the horizontal acceleration time series are broad banded, and with higher amplitudes at mid-span than at quarter-spam. This outcome can be explained by considering the high lateral stiffness offered by the restraint at the shore connection.

The response in terms of horizontal accelerations tends to be steady state after $60s$ in models B and D, and after $90s$ in models A and C. The horizontal acceleration at mid-span and quarter-span are in phase.

In Table 6.10 are reported the maximum and minimum horizontal accelerations at quarter-span and mid-span, for models A, B, C and D.

Table 6.10: Maximum and minimum horizontal acceleration results. Dynamic analysis, load combination (a), models A, B, C, D

Model	A		B		C		D	
Position	min (m/s^2)	max (m/s^2)	min (m/s^2)	max (m/s^2)	min (m/s^2)	max (m/s^2)	min (m/s^2)	max (m/s^2)
x=0.25L	-0.05	0.03	-0.02	0.02	-0.02	0.02	-0.04	0.03
x=0.5L	-0.1	0.07	-0.04	0.04	-0.04	0.04	-0.07	0.05
a_{Lim}	0.3							
Verified	yes	yes	yes	yes	yes	yes	yes	yes

As listed in Table 6.10, all the models tested satisfy the structural requirement regarding the maximum horizontal acceleration, when wave combination (a) is considered. According to Table 6.10, model A is the one with the highest horizontal acceleration amplitude. Therefore it can be concluded that by adding tethers in the structure, the horizontal accelerations are reduced.

Models B and C have similar horizontal accelerations, this implies that, under the wave combination considered, the inclined tether does not reduce the horizontal accelerations.

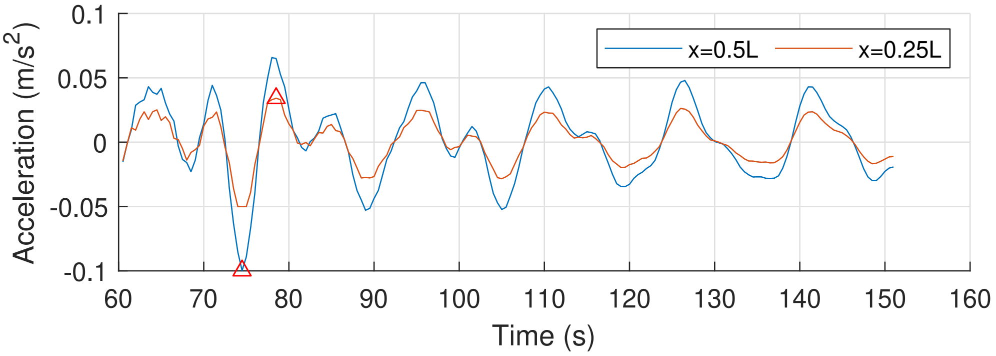

(a) Model A

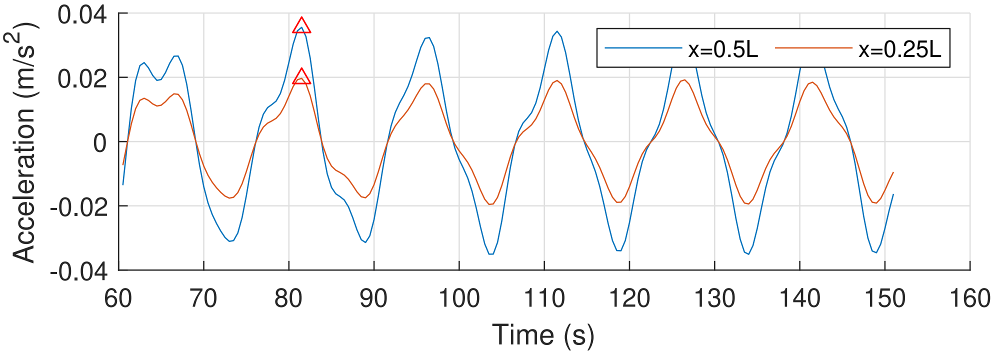

(b) Model B

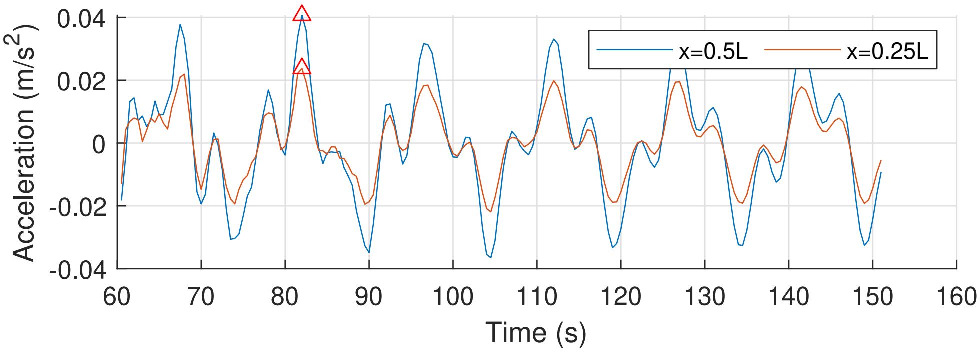

(c) Model C

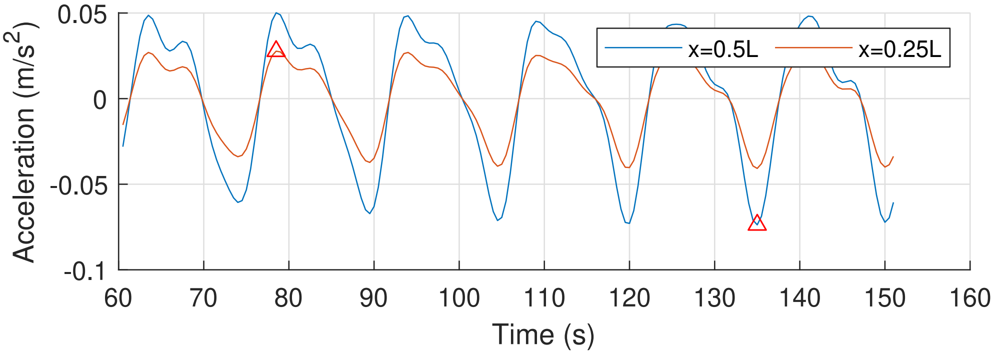

(d) Model D

Figure 6.16: Horizontal acceleration response at mid-span and quarter-span. Models A, B, C, D, load combination (a)

Model B has lower horizontal accelerations than model D, this means that the double arch configuration can reduce the horizontal accelerations with respect a straight configuration of the tunnel.

Vertical accelerations

In Figs. 6.17a to 6.17d are illustrated the vertical accelerations at mid-span and quarter-span, for the four models under the wave load combination (a).

It can be noticed in Figs. 6.17a to 6.17d that the structural response in terms of vertical accelerations is broad banded and does not become steady state within the considered period. A larger period of the analysis would lead to a more accurate result in terms of extreme values. However the values are well below the structural requirement limitation, a longer analysis will be performed for the irregular wave loading.

In Table 6.11 are listed the maximum and minimum vertical accelerations at mid-span and quarter-span for the four models.

Table 6.11: Maximum and minimum vertical acceleration results. Dynamic analysis, load combination (a), models A, B, C, D

Model	A		B		C		D	
Position	min (m/s^2)	max (m/s^2)	min (m/s^2)	max (m/s^2)	min (m/s^2)	max (m/s^2)	min (m/s^2)	max (m/s^2)
x=0.25L	-0.1	0.1	-0.01	0.01	-0.03	0.03	-0.01	0.01
x=0.5L	-0.16	0.17	0	0	-0.03	0.04	0	0
a_{Lim}	0.5							
Verified	yes	yes	yes	yes	yes	yes	yes	yes

As indicated in Table 6.11, all the models satisfy the structural requirement regarding maximum vertical acceleration allowable.

Model A shows larger vertical accelerations than model B and C, and model C has higher accelerations than model B. This indicates that increasing the number of vertical tethers the vertical accelerations are reduced, and a couple of vertical tether shows better results than a couple composed by an inclined and a vertical tethers.
Model B and model D show similar results, therefore the double arch configuration does not reduce the vertical accelerations.

Discrete Fourier Transform of Accelerations

The theoretical background regarding the discrete Fourier transform (DFT) is reported in section 3.5.1. The frequency analysis is performed in order to derive additional information regarding the structural response. The frequency resolution is analogous to the one adopted

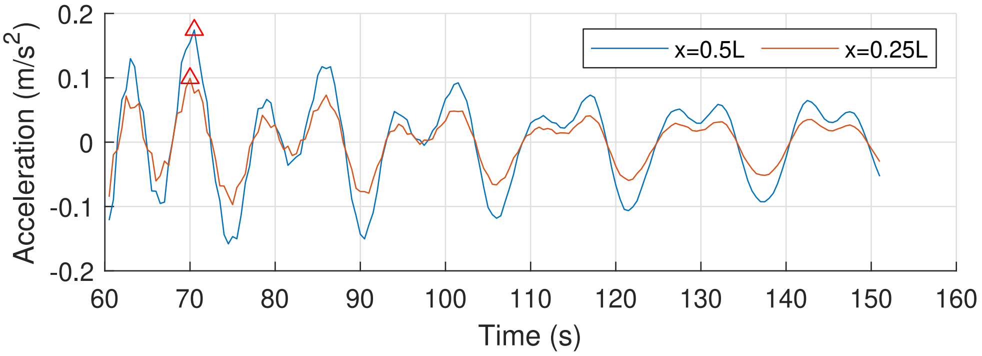

(a) Model A

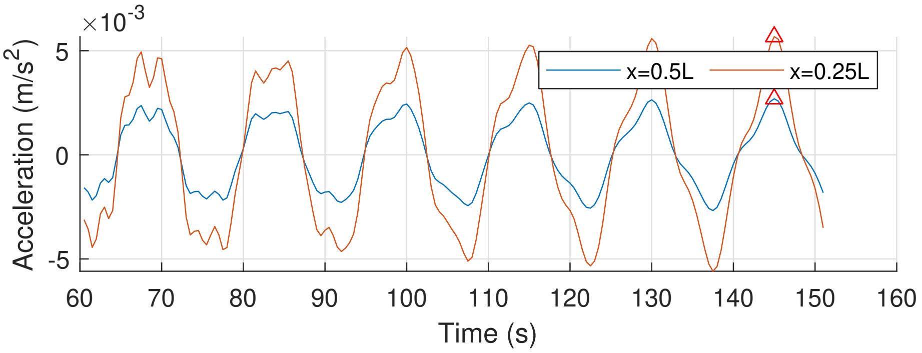

(b) Model B

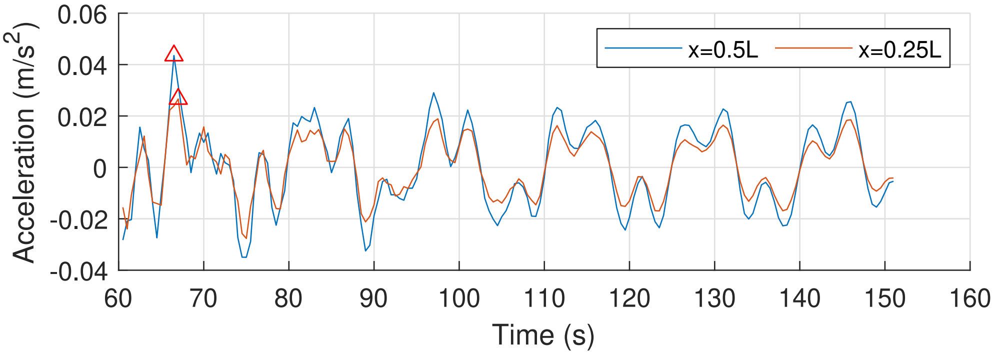

(c) Model C

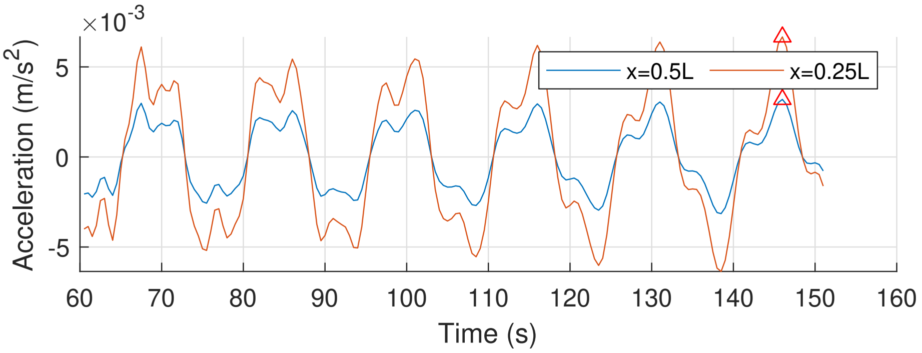

(d) Model D

Figure 6.17: Vertical acceleration response at mid-span and quarter-span. Models A, B, C, D, load combination (a)

for the DFT of displacements 6.3.1.

The DFTs of the horizontal structural accelerations at mid-span are illustrated in Figs. 6.18a to 6.18d, the vertical in Figs. 6.19a to 6.19d. On the left side are indicated with ω_w and ω_s respectively the wind and swell waves significant frequencies. On the right side are reported through vertical black lines the natural frequencies of the structure considered.

It can be noticed in Figs. 6.18a to 6.18d and 6.19a to 6.19d, that the DFTs spreads over a broad range of frequencies in both horizontal and vertical directions, therefore it might not be approximate narrow banded.

It can be first noticed that the structural response in term of accelerations is excited also by the wind waves, which did not influence the response in term of displacements. From Figs. 6.18a to 6.18d it can be seen that that the swell waves generally governs the horizontal accelerations, however large peaks are also present due to the coincidence of the wind waves frequency with the resonance frequencies.

In Figs. 6.18a, 6.18c, 6.19a and 6.19c are present large peaks induced by the the proximity between the natural frequencies of the system with the wind waves significant frequency, being close to resonance the wind waves effects are highly amplified.

In models B and D, Figs. 6.18b, 6.18d, 6.19b and 6.19d, the response in terms of acceleration is so governed by swell waves.

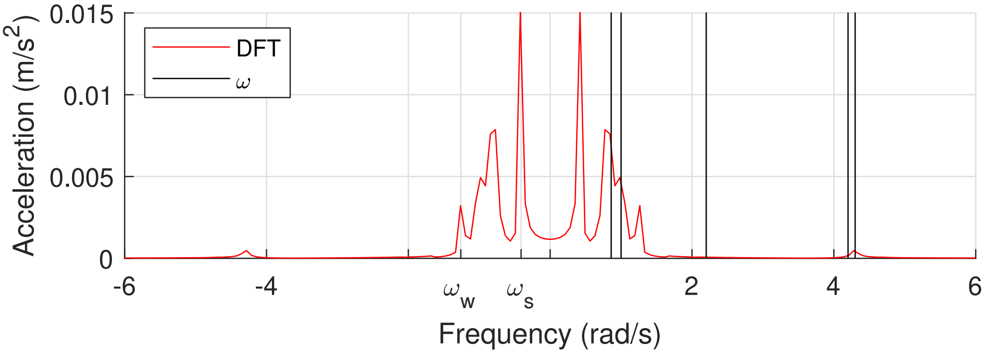

(a) Model A

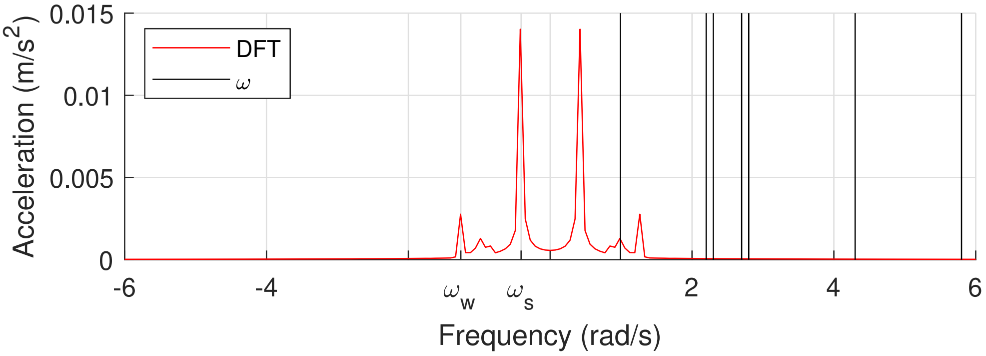

(b) Model B

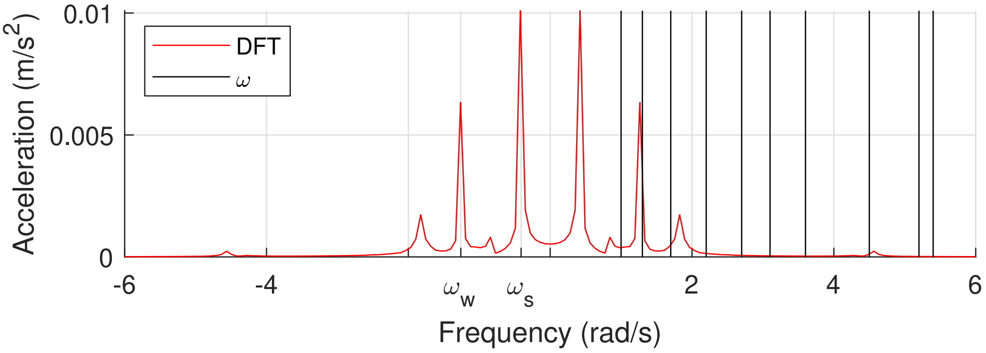

(c) Model C

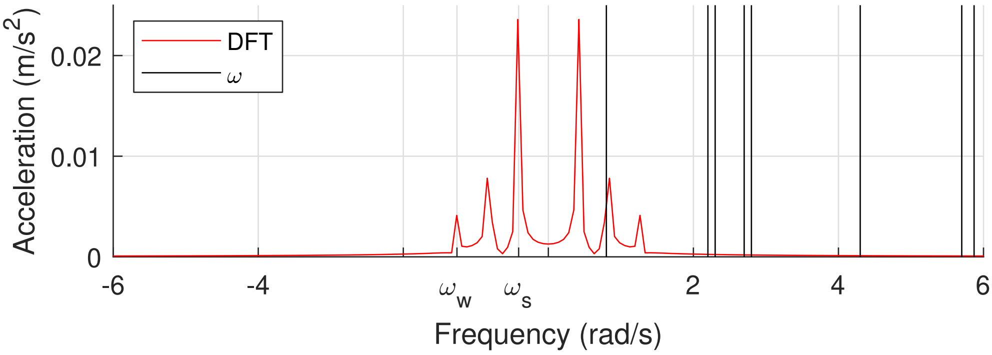

(d) Model D

Figure 6.18: DFT of the horizontal accelerations at mid-span for models A, B, C, D

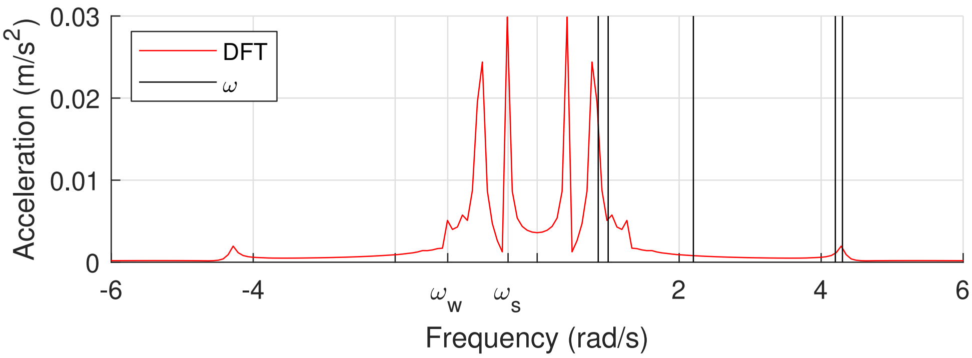

(a) Model A

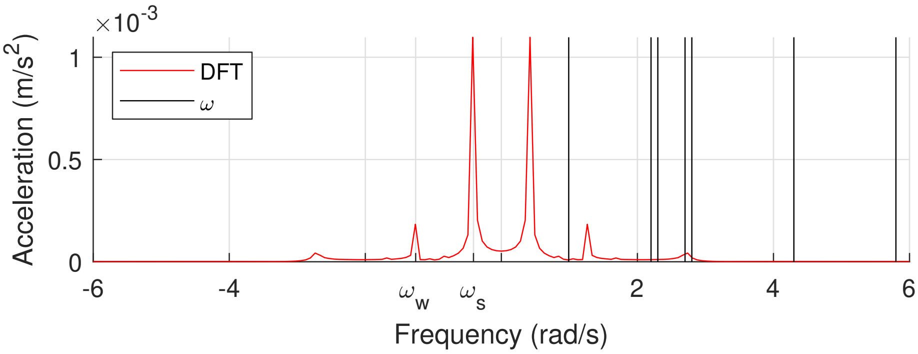

(b) Model B

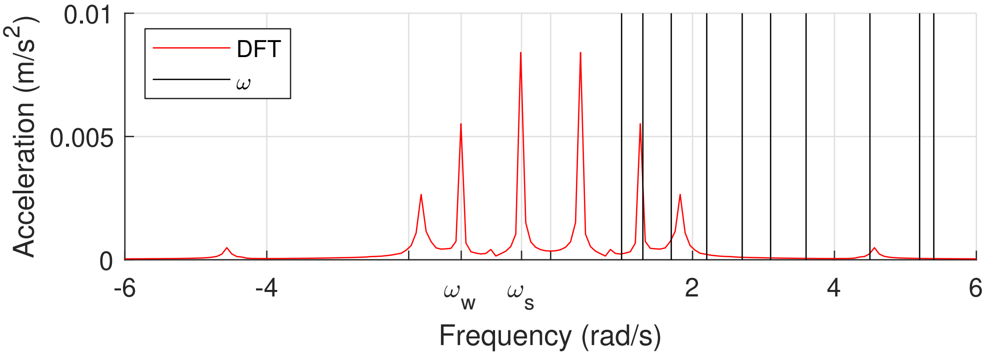

(c) Model C

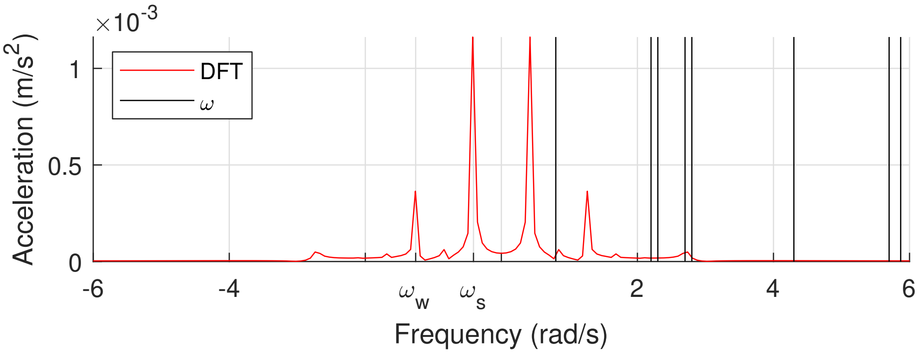

(d) Model D

Figure 6.19: DFT of the vertical accelerations at mid-span for models A, B, C, D

6.3.3 Internal Forces and Moments

In this section models A, B, C and D are compared in terms of bending moment and axial force in the tether. The results are derived by several regular waves dynamic analysis of $150s$.

Bending moments

The bending moment envelope derived from the dynamic analysis was founded to be analogous to the static analysis bending moment distribution, just amplified. Therefore, only the maximum and minimum bending moment around the $y - axis$ and $z - axis$ are herein reported in Table 6.12.

The maximum negative and positive bending moments amplitude around both axis are located at the end sections, the mid-span and quarter-span.

Table 6.12: Maximum positive and negative bending moments, model A, B, C and D, regular wave dynamic analysis

Model	Type of analysis	Bending moment (MNm)					
		M_y			M_z		
		(-)	(+)	Δ	(-)	(+)	Δ
A	*static*	-3451	1743		-11	42	
	dynamic	-4691	2589	$+26\%$	-716	1224	$+96\%$
B	*static*	-1581	719		-390	203	
	dynamic	-1634	741	$+3\%$	-718	386	$+47\%$
C	*static*	-2355	1002		-431	152	
	dynamic	-3752	1086	$+37\%$	-986	985	$+85\%$
D	*static*	-1592	724		-309	155	
	dynamic	-1624	738	$+2\%$	-867	680	$+77\%$

In Table 6.12 is also indicated by Δ the maximum increment in percentage between the static and the dynamic analysis. It can be noticed that models B and D have a smaller increment than models A and C.

Considering the bending moment around the $y - axis$, models B and D have similar amplitudes, while models A and C have a maximum absolute M_y more than twice than models B and D.

The bending moment M_z is generally lower than M_y, but it is more dependent on the dynamic effects, so it could be higher for other loading conditions. According to table 6.12, model B is the one having smaller bending moment M_z amplitude and increment.

Tether Axial Forces

The tethers response is directly related to the displacement at mid-span of the SFTs for models B and D. Regarding model C the tether axial forces are dependent on the kinematic friction of the pulley, and on the tunnel displacement. It is also interesting to analyze the relative displacement between the inclined and the vertical tether in model C.

It is represented in Fig. 6.20 the maximum axial force registered in the tethers during a regular wave dynamic analysis of $150s$.

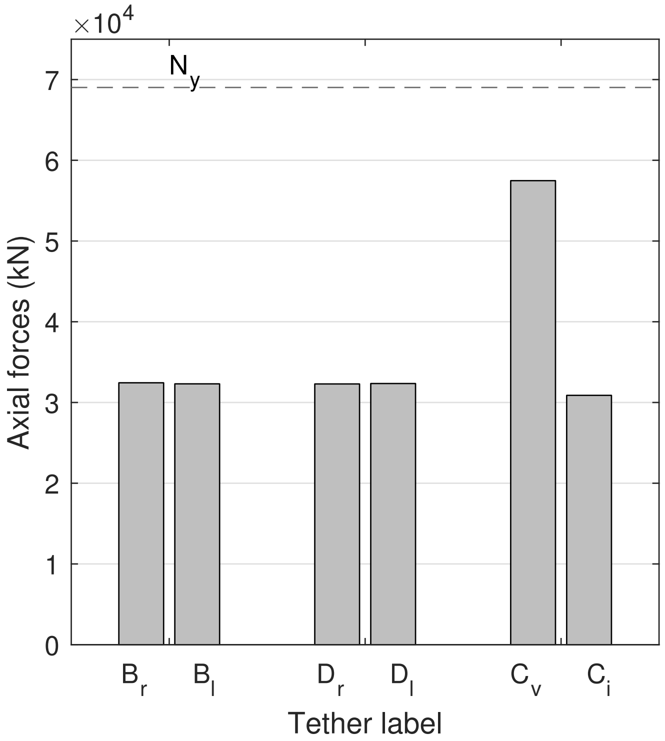

Figure 6.20: Maximum axial forces in the tethers, models B, C and D, regular wave dynamic analysis

N_y	is the yielding axial force;
B_r, B_l	are respectively the right side and left side tether in model B;
D_r, D_l	are respectively the right side and left side tether in model D;
C_v, C_l	are respectively the vertical and horizontal tether in model C.

It can be noticed in Fig. 6.20, that all the tethers remain in the elastic domain, since the yielding axial force is not crossed. Models B and C have an analogous maximum vertical displacement, as reported in Table 6.9, therefore since permanent deformations due to plastic effects are not presents in the model, the tether axial force is expected to be analogous. This is in agreement with Fig. 6.20. The difference between the axial force in the inclined tether and the vertical tether in model C, Fig. 6.20, is the force due to the kinematic friction in the pulley.

Tether arrangement for models B, C and D with respect the current and wave direction is illustrated in Fig. 5.5. The current and wave forces are applied on the negative $y-direction$, therefore, as it was expected, the tether placed in the right side of the tunnel cross section is subjected to higher tensile forces.

In Fig. 6.21 it is illustrated the relative displacement between the vertical and inclined tether in model C. The displacement is measure along the tether center line.

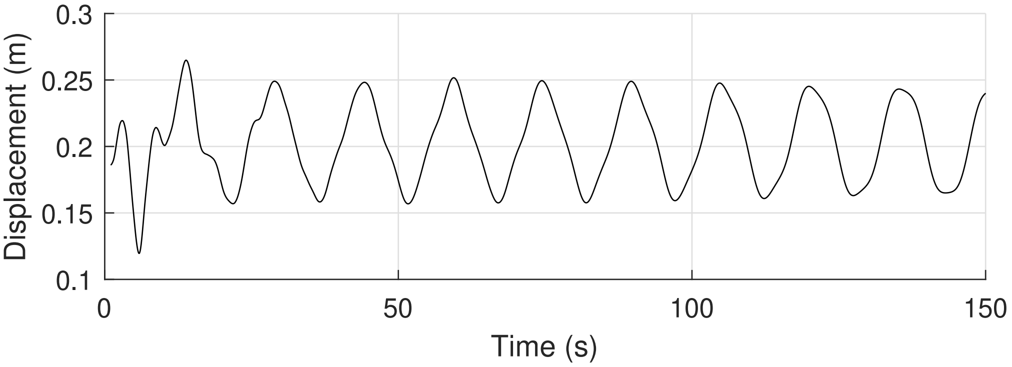

Figure 6.21: Relative displacement between inclined and vertical tether, model C

It ca be seen in Fig. 6.21 that the maximum relative displacement between the upper parts of the two tethers is 0.27 m. This correspond to one-fifteenth of a full rotation of the circular pulley, considering a radius of the pulley of 0.3 m.

6.4 Sensitivity Study

In this section are reported the results of various sensitivity study analysis. The analysis set up and the preliminary considerations are founded in section 5.4.

The intent of the sensitivity study is to find a favorable design among several candidates. The effects of varying the BWR, the wave loading condition and the rotational stiffnesses at the abutments are here analyzed and commented.

6.4.1 Varying BWR

As previously extensively explained in section 5.4.1, the BWR in SFTs is a fundamental parameter. The advantages and drawbacks expected on increasing the BWR are also listed in 5.4.1. In this section the BWR effects are analyzed in terms of tethers stress and natural period of the structure.

Tether Stress

The tether initial stress is governed by the BWR, and it influences the natural periods of the structure, in agreement with the theoretical method for eigenfrequencies 3.4.2, where is stated that an higher tether initial stress increases the structural generalized stiffness.

In Figs. 6.21c, 6.22a and 6.22b are illustrated the tether stresses varying the BWR for the models B, C and D. It is important to remind that plastic deformations due to wave loading are not allowed, and that an higher tether initial stress implies an higher restoring forces in the foundations.

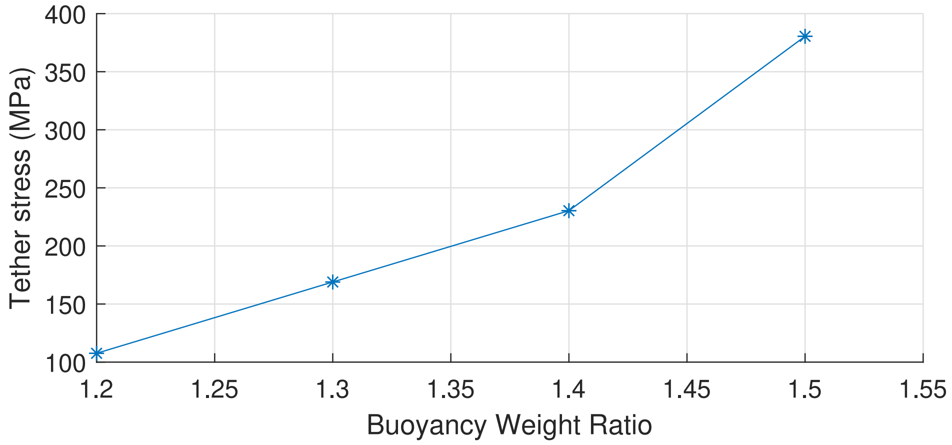

(a) Model B

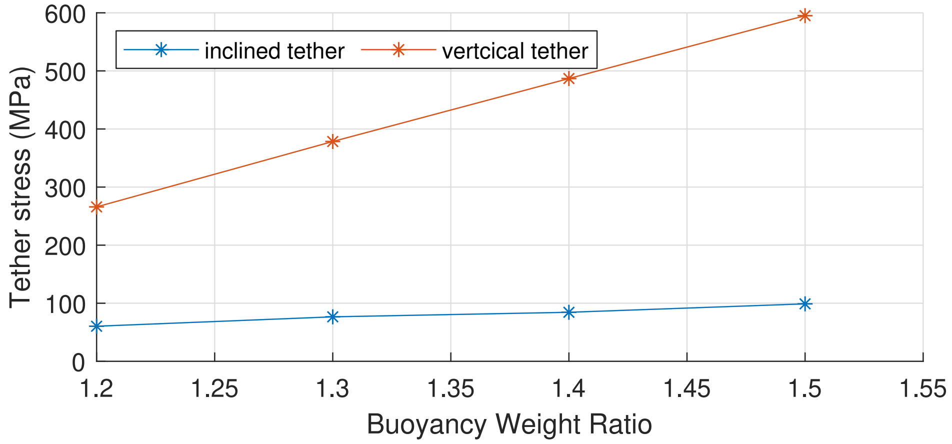

(b) Model C

It can be noticed comparing model B with model D, in Figs. 6.21c and 6.22a, that the tether stress is more influenced by the BWR in the double arch configuration (model B) than in the straight tunnel configuration (model D). In Fig. 6.22b it can be seen that the inclined tether is only slightly affected by the BWR.

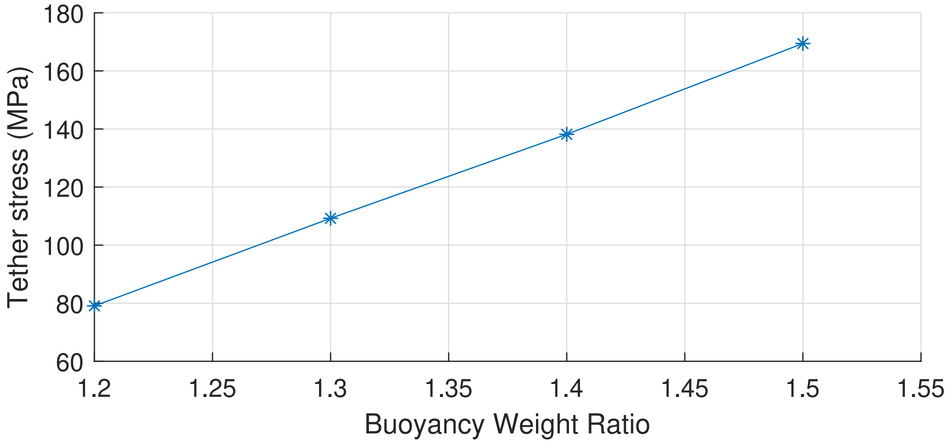

(c) Model D

Figure 6.21: Tether stress varying the buoyancy weight ratio. Model B (a), Model C (b), Model D (c)

Modal Analysis

The buoyancy weight ratio (BWR) of the structure is strictly related with the level of pretension in the tether. The tension in the tethers influences the natural frequency of the whole structure, as shown in equation (3.40). However, according to the empirical method described in section 3.4.2, it influences only sway modes. Calculated natural periods for the first four modes, varying the buoyancy weight ratio are founded in Figs. 6.22a to 6.22d. The line of reasoning behind this study is described in section 5.4.1. Only the first four natural modes are analyzed due to the fact that are the ones with frequencies in proximity of the wave loading range of frequencies.

In Fig. 6.22a can be seen that the first natural period of model C is highly influenced by the BWR, if compared to the first natural period of models C and D. The reason for this result is that the first mode of model C is a tether natural mode, as reported in Table 6.4. Models C and B show a smaller first natural frequency than models D for all the BWRs considered.

The Fig. 6.22b shows that models B and D have a similar second natural period, which is independent on the BWR. The second natural period in model C is linearly dependent on the BWR and it decreases of half a second between a BWR of 1.2 to one of 1.5.

The third natural frequency is only slightly influenced by the BWR in model B, while it is practically constant in models C and D as illustrated in Fig. 6.22c. In models B for a BWR corresponding to 1.2 the third natural frequency is a tether natural mode.

In Fig. 6.22d it is depicted that the fourth global natural period of model C is independent on the BWR, while the fourth period of models B and D decreases for higher values of BWR.

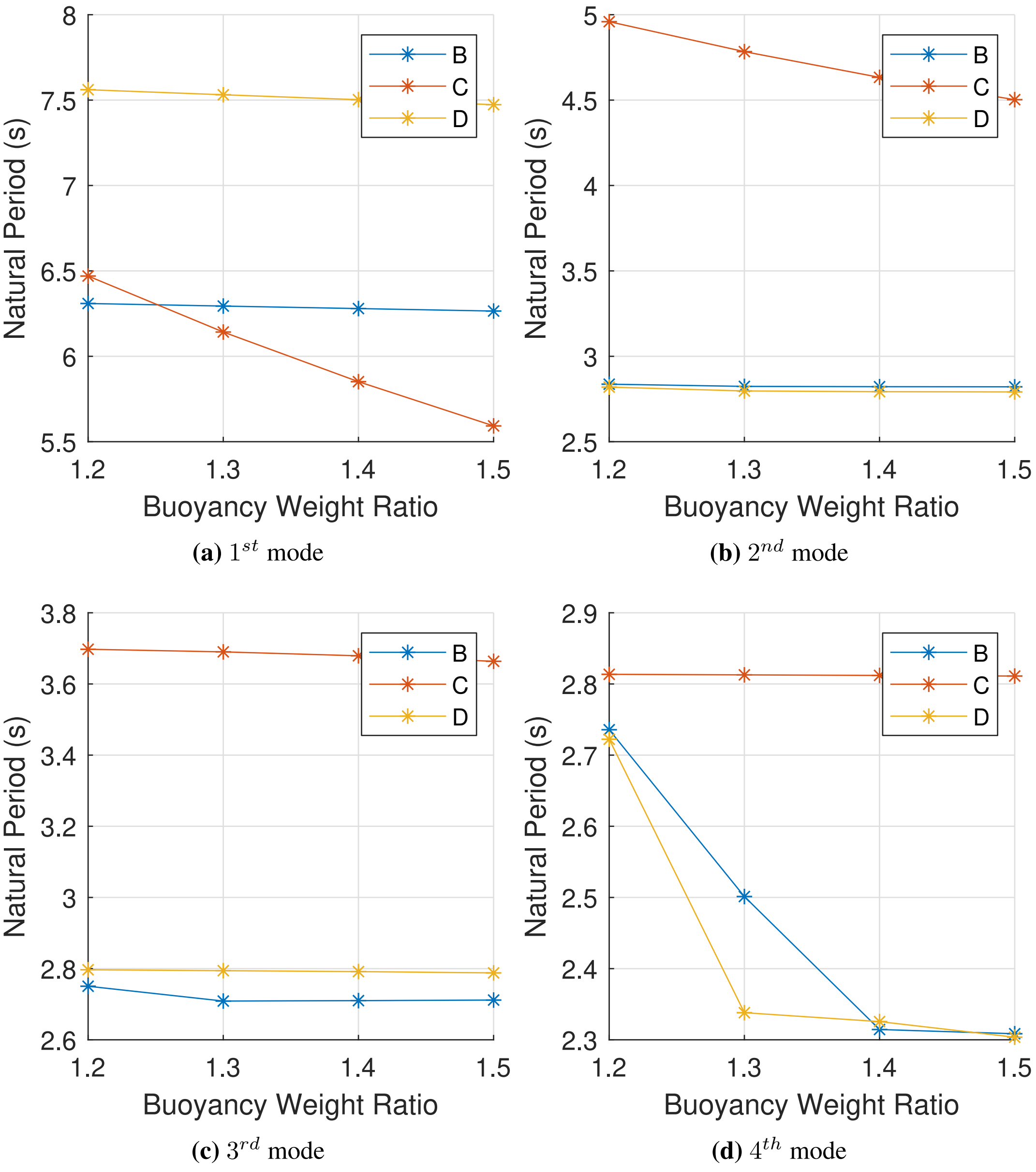

(a) 1^{st} mode **(b)** 2^{nd} mode

(c) 3^{rd} mode **(d)** 4^{th} mode

Figure 6.22: SFTs models B,C,D. First (a), second (b) , third (c) and fourth (d) SFT's natural periods varying the buoyancy weight ratio

6.4.2 Calm Sea Condition

This sensitivity analysis is useful in order to have a better comprehension of the results in section 6.1. A $BWR = 1.2$ is assumed for both the models. Under calm water conditions the current velocity and the wave height are set to zero, the only horizontal forces are the water pressure forces, but they are self balanced. The analysis is performed considering only permanent forces, which includes dead load and buoyancy load. It can be notice in Fig. 6.23a, that the horizontal displacement of the straight tunnel configuration (model D)

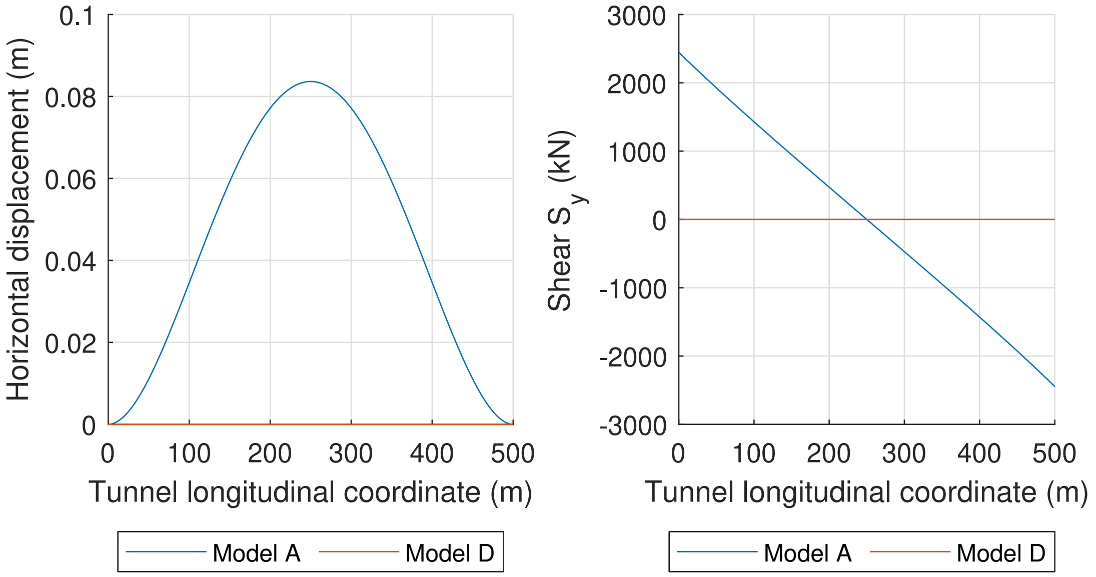

(a) Horizontal displacement **(b)** Shear along $y - axis$

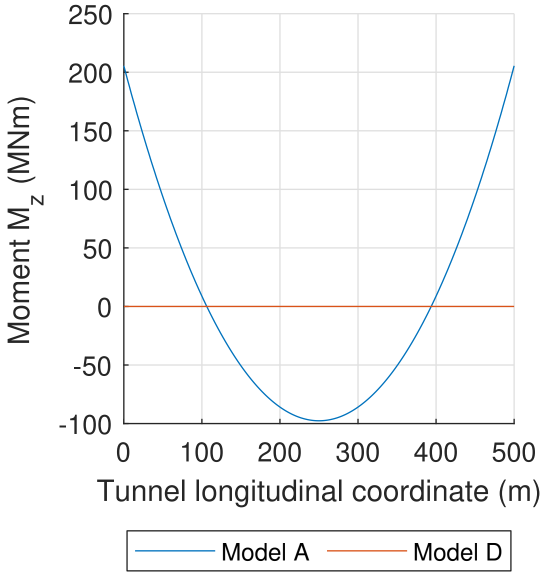

(c) Bending moment around $z - axis$

Figure 6.23: SFTs models A and D. Horizontal displacement (a), horizontal shear force (b), horizontal bending moment comparison, during Calm Sea Conditions

is null, while the displacement of the double curved configuration (model A) is maximum at the mid-span.

Comparing models A in calm water conditions Fig. 6.23a with model A under severe state conditions Fig. 6.2a. It can be seen, that for the same BWR, the maximum horizontal displacement is only $0.6cm$ lower in calm sea conditions than in severe sea state conditions.

From this results can be empathized that in model D horizontal displacement are not coupled with vertical forces, while this is not the case for model A. Moreover if the horizontal displacements are considered relatively to the initial deformed configuration they result smaller in model A than in model D, in agreement with the two dimensional analytical model.

Fig. 6.23b, representing the horizontal sectional forces along the tunnel length, shows that in model D they are always zero, while they are asymmetrical distributed in model A. Examining model A under different load conditions, the maximum shear S_y is $386kN$ lower in calm sea conditions, Fig. 6.23b, than under the severe state conditions,Fig. 6.4a.

Fig. 6.23c illustrates the bending moment distribution M_z, in agreement with the previous results the bending moment in model D is null, while in model A it has a parabolic distribution. In model A the bending moment is $28MN$ lower in the case of calm sea conditions,Fig. 6.23c, than under severe state conditions Fig. 6.7a.

From this sensitivity study is found that model D acts as a 2D model under static actions, in other words vertical actions does not cause horizontal internal forces or displacements. This is not the case in model A, where horizontal displacements and internal forces are more dependent on vertical actions than horizontal actions. Concluding it is complex to compare model A and D adopting the same reference system, due to the fact that model A has an initial horizontal deformation due to permanent forces, mainly due to buoyancy.

6.4.3 Other Load Combination on Model B

In this section model B is tested under other wave loading conditions. For sake of simplicity a regular wave deterministic analysis is performed, and the significant wave period and wave height are respectively reduced of 10% and increased of 90%. The results are compared in terms of displacement, bending moment and tether axial force. Only dynamic analysis with geometric non-linearity are performed in this section.

The different load combinations are described and analyzed in Table 5.5. In this sections are repeated the wave design periods and heights, reported in Table 6.13.

Figs. 6.24 to 6.28 allow an easy comparison among the different regular wave load combinations applied on model B.

The maximum displacement envelopes due to hydrodynamic loads are illustrated in

Table 6.13: Design significant wave period and height for load combinations (a), (b) and (c)

Load combination	Swell wave		Wind wave	
	period (s)	height(m)	period (s)	height(m)
(b)	15.3	2.09	4.95	3.8
(c)	15.3	4.37	6.75	4.56
(d)	15.3	5.7	7.65	5.32

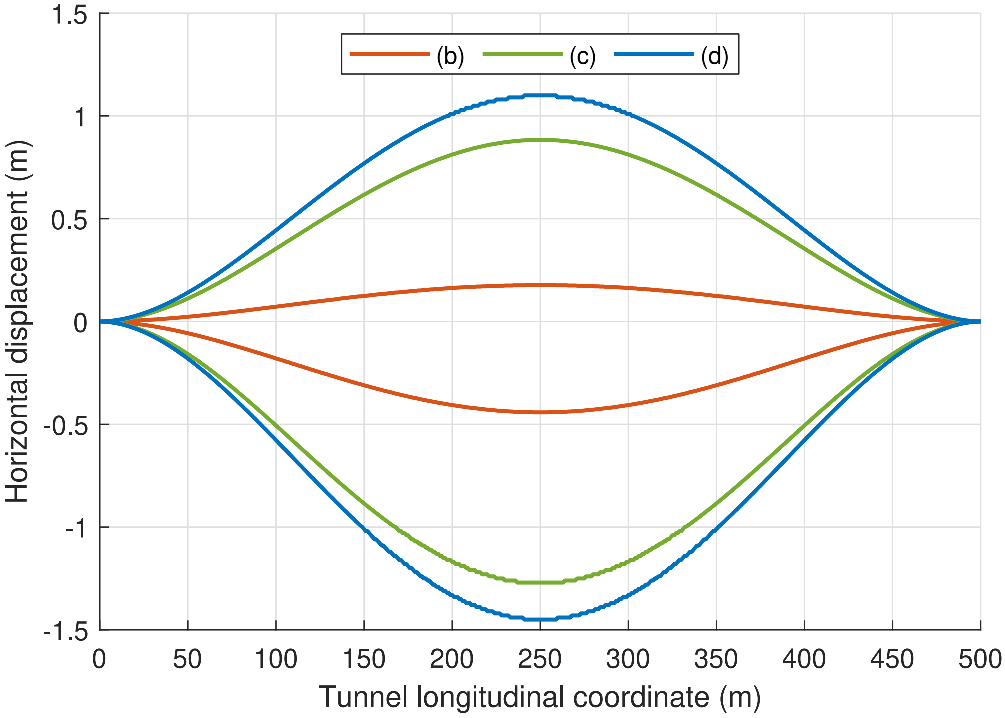

Figure 6.24: Maximum and minimum envelopes of horizontal displacement for three different wave load combination, model B,regular wave dynamic analysis

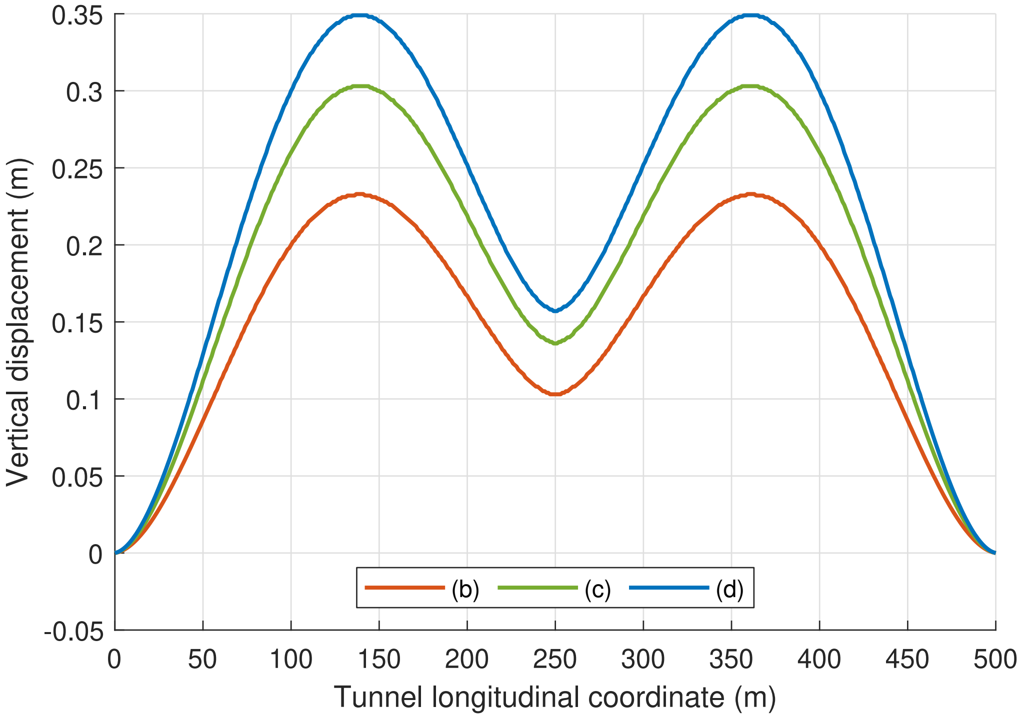

Figure 6.25: Maximum and minimum envelopes of vertical displacement for three different wave load combination, model B,regular wave dynamic analysis

Figs. 6.24 and 6.25. It can be clearly noticed that the wave combination (d) is the most critical. The horizontal structural response is largely influenced by the wave combination, in particular at mid-span there is an increment of 70% comparing the combinations (b) and (d).

The vertical displacement is less dependent on the wave loading than the horizontal displacement, in fact the maximum increment from (b) to (d) in Fig. 6.25 is 33%.

It can finally be concluded that model B satisfy the structural requirement limitations regarding the maximum deflection for all the wave combinations adopted.

The maximum and minimum envelopes of bending moments derived from a regular waves dynamic analysis are illustrated in Figs. 6.26 and 6.27.

It is possible to notice that, for all the combination, the minimum negative M_y is at the end sections, while the maximum positive at the quarter-spans. The bending moment around the $y-axis$ increments of approximately 34%, both at the end sections and quarter-spans, going from (b) to (d).

With regard to the bending moment distribution M_z, Fig. 6.27 shows that M_z can be positive or negative along all the tunnel length. Moreover, there is an increment of 63% going from (b) to (c), and an increment of 13% from (c) to (d).

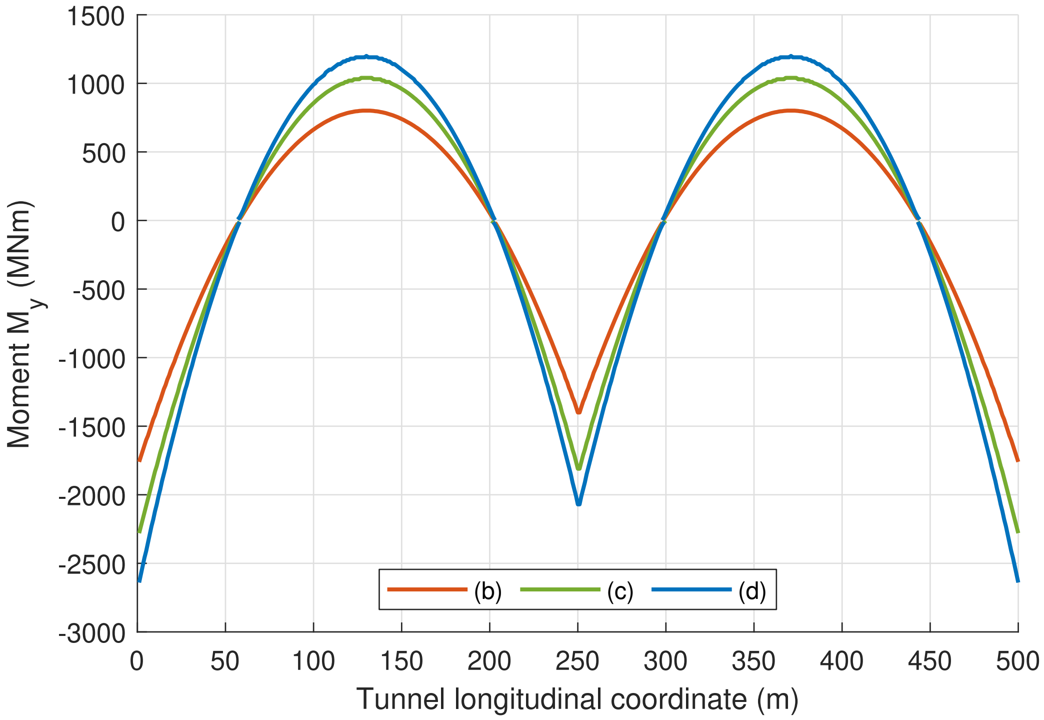

Figure 6.26: Maximum and minimum envelopes of bending moment about y-axis (M_y) for three different wave load combination, model B,regular wave dynamic analysis

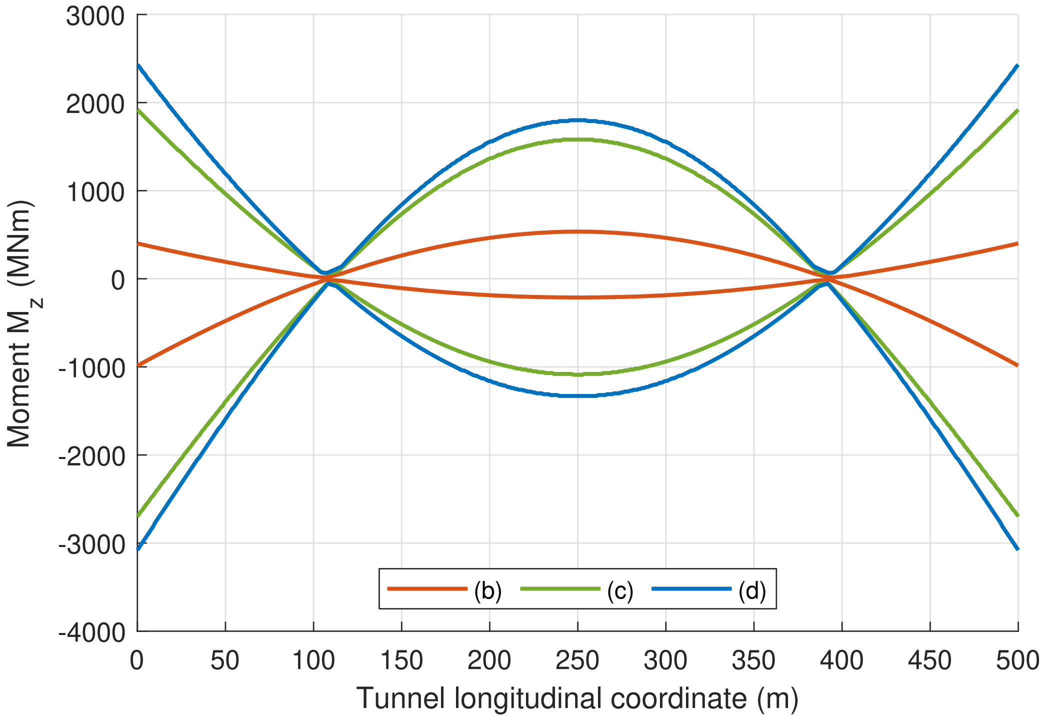

Figure 6.27: Maximum and minimum envelopes of bending moment about z-axis (M_y) for three different wave load combination, model B, regular wave dynamic analysis

The maximum tether axial forces registered in model B under the regular wave combinations (b), (c) and (d), is shown in Fig. 6.28.

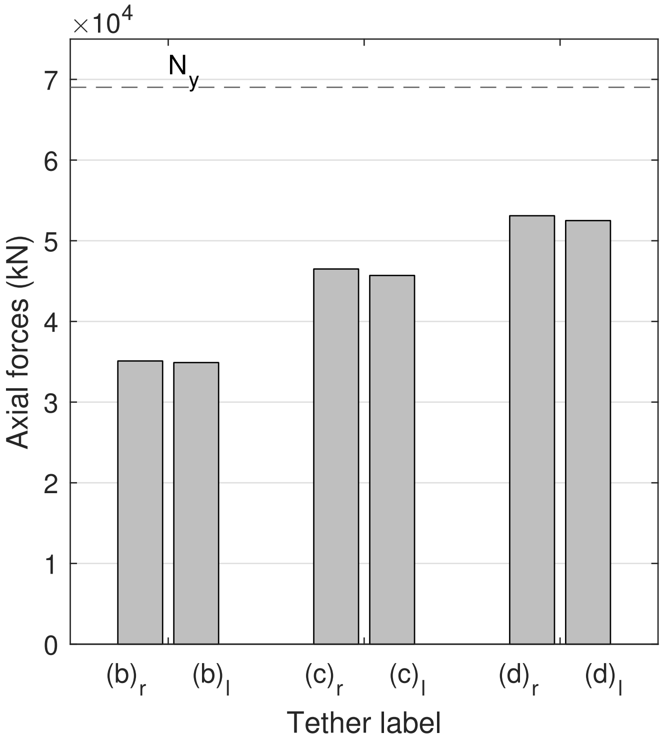

Figure 6.28: Maximum tether axial forces in model B, under three different wave load combination, regular wave dynamic analysis

N_y	is the yielding axial force;
$(b)_r, (b)_l$	are respectively the right side and left side tether, regular wave combination (b);
$(c)_r, (c)_l$	are respectively the right side and left side tether, regular wave combination (c);
$(d)_r, (d)_l$	are respectively the right side and left side tether, regular wave combination (d);

It can be seen in Fig. 6.28 that the tethers remain in the elastic domain under all the regular wave combinations considered. Overall it can be seen a clear upward trend from case (b) to case (d).

6.4.4 Effect of Rotational Stiffness at the Abutments

This section contains the results from the sensitivity study regarding the rotational stiffness at the end sections in model B, under the regular wave load combination (a). As explained in section 5.4.2 , the stiffness offered by the abutments is an interesting and necessary study in the design of a SFT.

The results are here compared in terms of displacements, bending moments, natural period of the structure and axial force in the tethers. Several regular wave dynamic analysis with a period of $150s$ have been performed. For each dynamic analysis the maximum and minimum value of the parameter concerned have been extract, and reported, in Figs. 6.29 to 6.33, together with the corresponding rotational stiffness at the abutments K_ϕ.

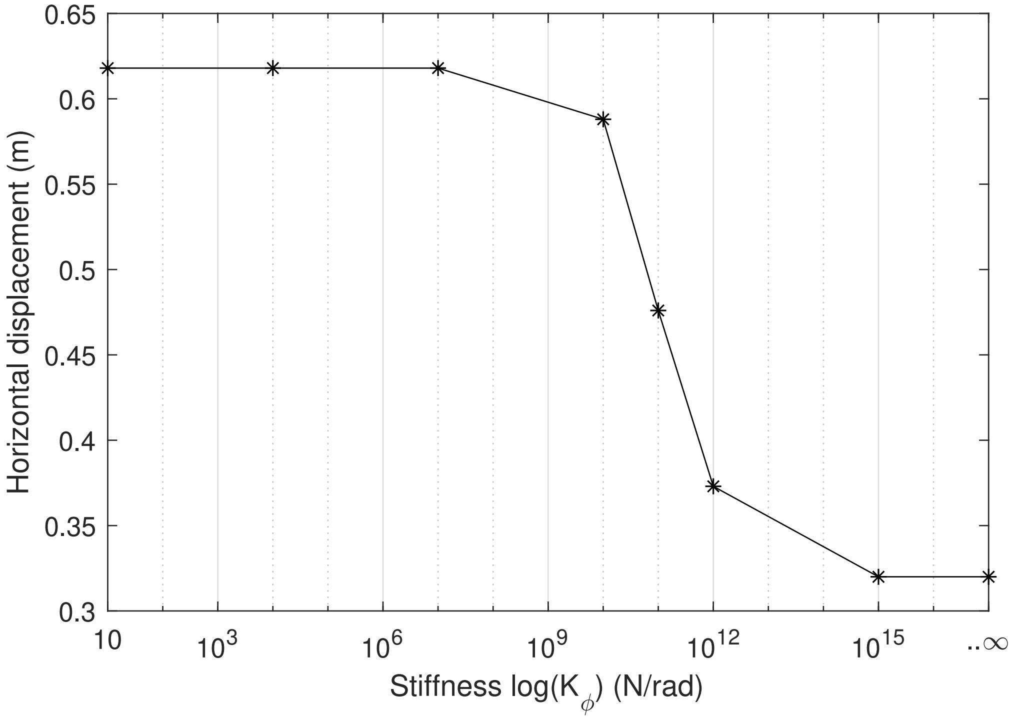

Figure 6.29: Horizontal displacement varying the rotational stiffness at the end sections, regular wave dynamic analysis (a), model B

It can be noticed in Fig. 6.29 that for K_ϕ going from 10^{10} to 10^{12} the horizontal displacement decreases dramatically, while for higher and lower values of stiffness is relatively constant. A similar trend is shown for the vertical displacement Fig. 6.30.

For both the horizontal and vertical displacements the amplitude increases of approximately 50% if a pinned connection is adopted instead of a fixed connection. However the structural requirements regarding the maximum allowed displacements are still fulfilled if a pin connection is adopted.

The maximum and minimum bending moment envelopes varying the end connection rotational stiffnesses are illustrated in Figs. 6.31 and 6.32.

It can be seen in Figs. 6.31 and 6.32 that the positive bending moment decreases if it increases K_ϕ, while the absolute amplitude of the negative bending moment decreases until a certain valued of K_ϕ, after which it increases again.

It is important to specify that the maximum and minimum values reported in the graph are taken from different positions along the tunnel longitudinal length. For this reason there is not an unique trend varying k_ϕ. Consequently a proper value of K_ϕ should be chosen in order to overall minimize maximum positive and negative bending moment around y and z axis. From Figs. 6.31 and 6.32 it results that an optimal value of K_ϕ is in the range 10^{10} to

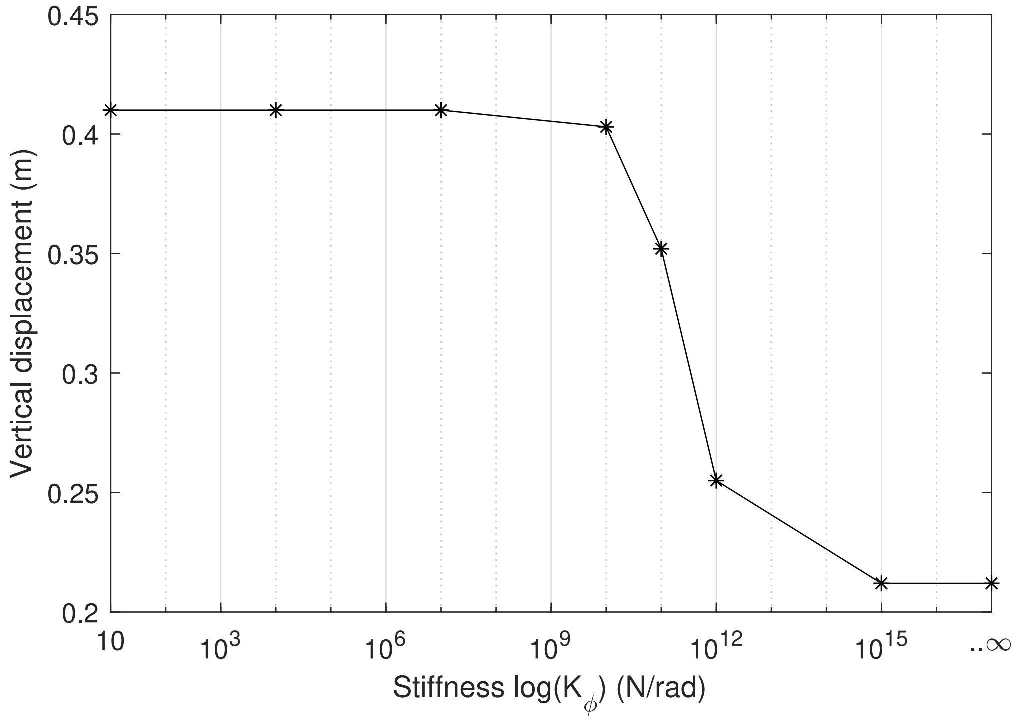

Figure 6.30: Vertical displacement varying the rotational stiffness at the end sections, regular wave dynamic analysis (a), model B

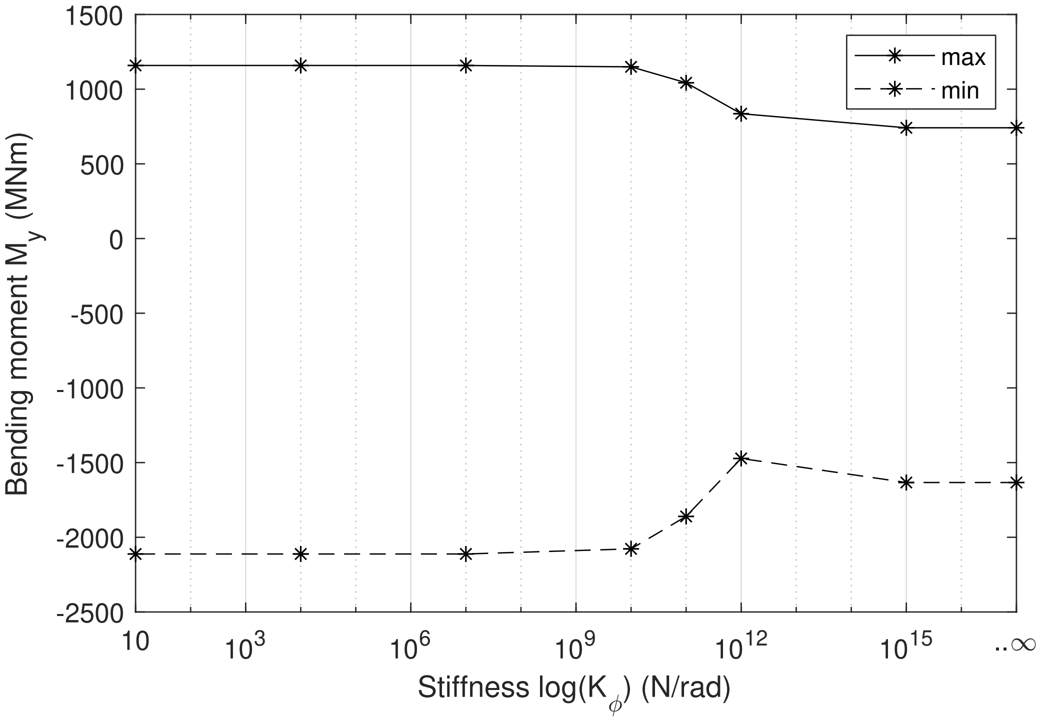

Figure 6.31: Bending moment around the $y-axis$ varying the rotational stiffness at the end sections, regular wave dynamic analysis (a), model B

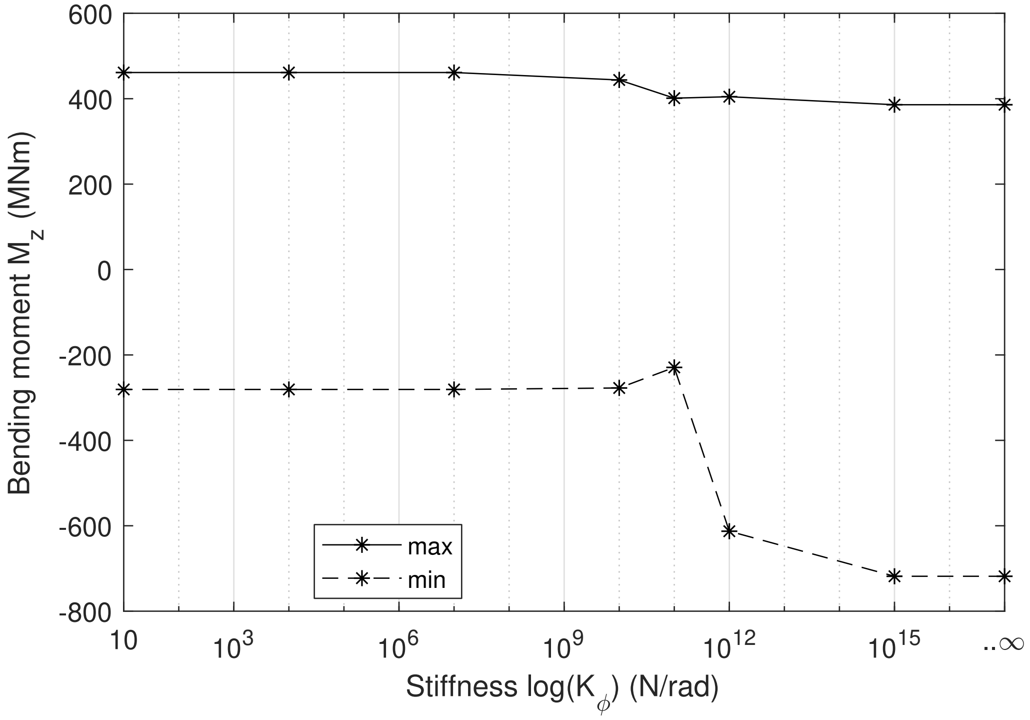

Figure 6.32: Bending moment around the $z - axis$ varying the rotational stiffness at the end sections, regular wave dynamic analysis (a), model B

10^{12} N/rad.

The tether axial force is an essential parameter to be controlled when the rotational stiffness at the end sections is reduced, the results are shown in Fig. 6.33.

From Fig. 6.33 is clear that the tether is subjected to higher loadings if K_ϕ is reduced. The line of maximum gradient is founded to be for values of K_ϕ in between 10^{10} and 10^{12}.

After all, the analysis results confirm that for rotational stiffnesses lower than $10^7 N/rad$, the end connection can be assumed as a pin connection. For rotational stiffnesses higher than $10^{15} N/rad$, the end connection can be considered a fixed connection.

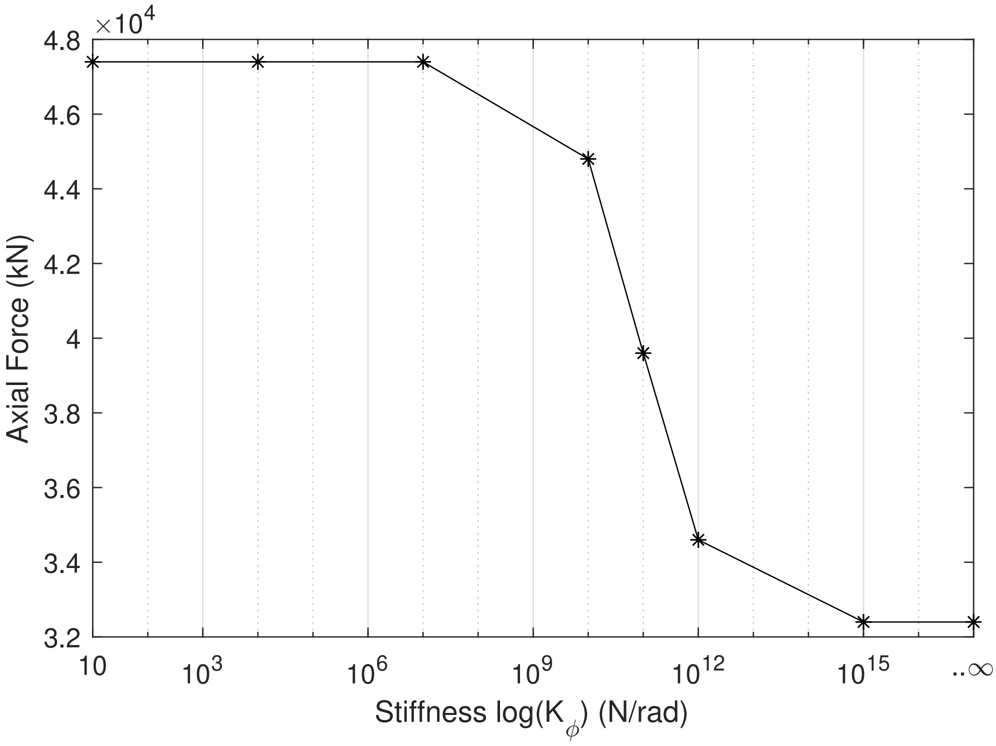

Figure 6.33: Tether axial force varying the rotational stiffness at the end sections, regular wave dynamic analysis (a), model B

6.5 Irregular Wave Analysis

This section contains the results of a dynamic analysis, section 5.3.7, when an irregular wave state is adopted, section 5.3.3. In order to consider simultaneously wind waves and swell waves, a double peak wave spectrum is adopted and illustrated in Fig. 6.34. The wave spectrum parameters are reported in section 5.3.3.

In order to consider also the wave energy spreading function, Fig. 3.1, a multi-dimensional spectral analysis is needed. The multi-dimensional spectrum is reported in Fig. 6.35.

Artificial generation of a two-dimensional random process can be founded in [Newland, 2005a], and it is shortly summarized in section 5.3.3. The randomly generated wave height, period, direction and phase are inserted in Abaqus/Aqua using the linear wave Airy theory.

The aim of performing an irregular wave analysis is to compare the results obtained with the modified regular wave analysis. In particular is compared model B under the wave state condition (a).

6.5.1 Displacements

In this section are reported the horizontal and vertical displacement responses in the most critical position along the longitudinal axis. The highest horizontal displacement are founded to be at mid-span, while the highest vertical displacement are located at quarter-span. This

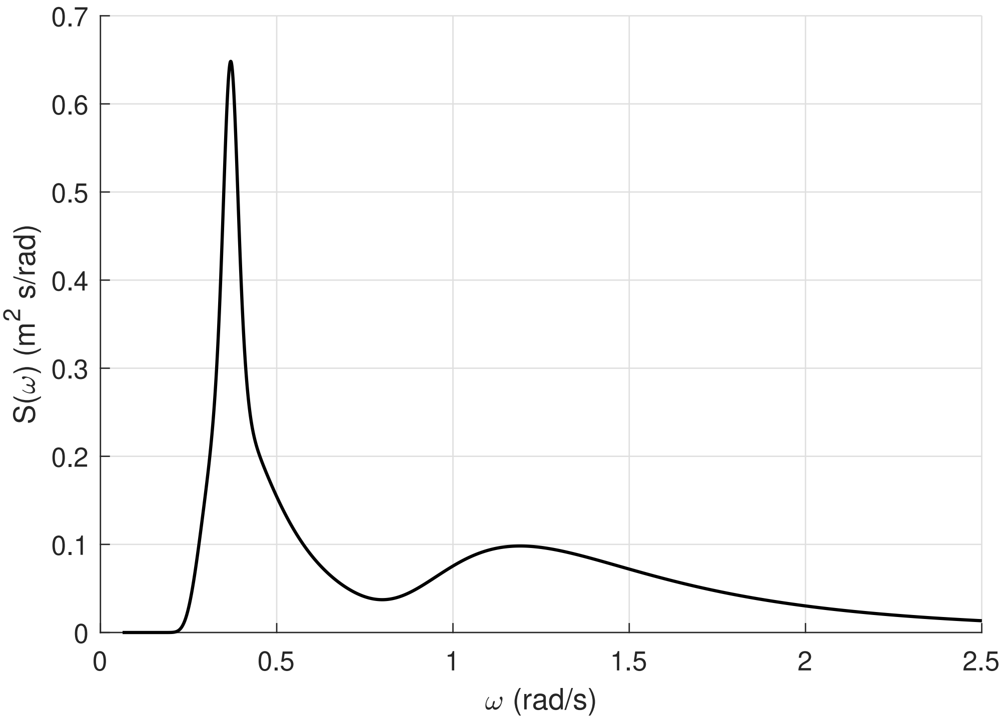

Figure 6.34: Torsethaugen double peak wave spectrum of load condition (a),[Torsethaugen, 1993]

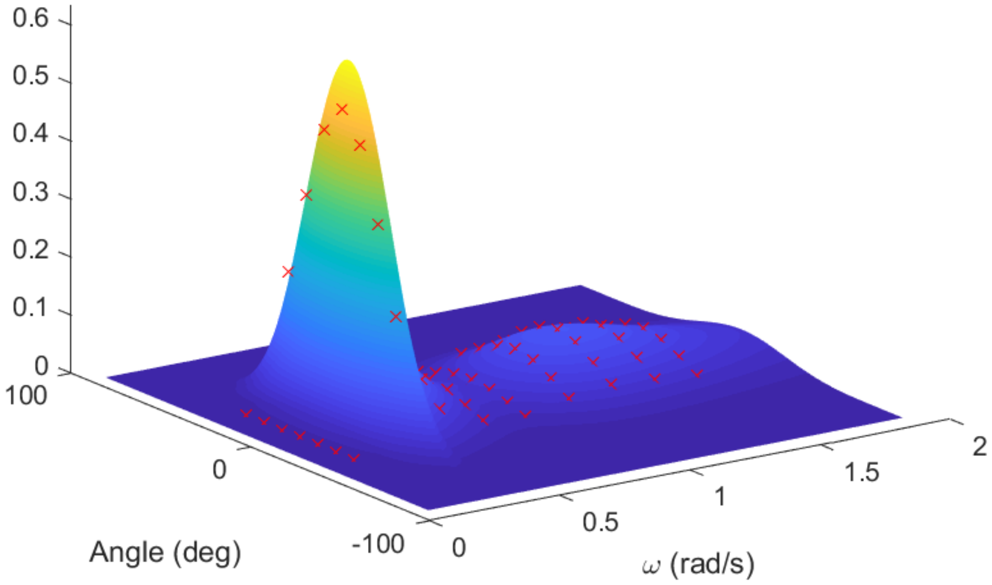

Figure 6.35: Surface spectrum considering the Torsethaugen double peak wave spectrum and the wave energy spreading function

was expected due to the presence of a couple of vertical tethers at mid-span.

The time series responses are shown in Figs. 6.36a and 6.36b, with a red triangle is indicated the highest absolute value.

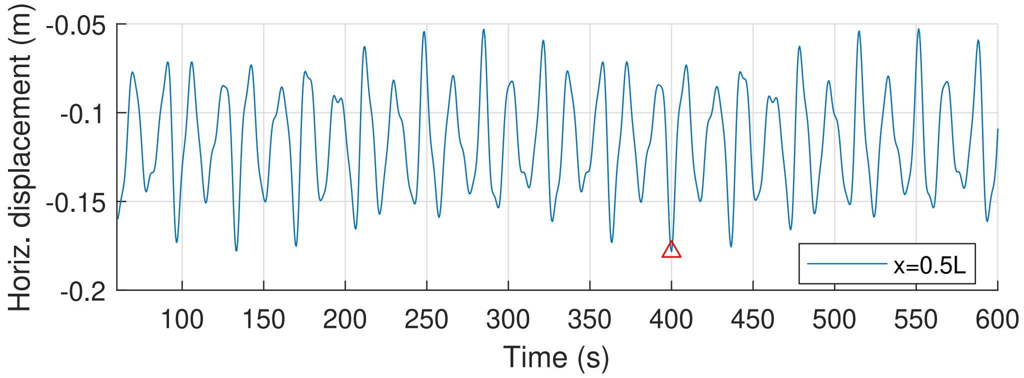

(a) Horizontal displacement at mid-span

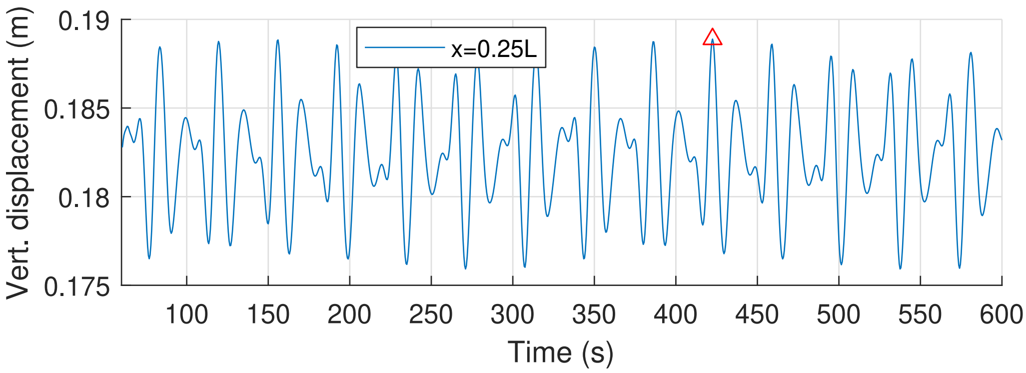

(b) Vertical displacement at quarter-span

Figure 6.36: Horizontal displacement at mid-span (a), and vertical displacement at quarter-span (b), irregular wave dynamic analysis, model B

A longer analysis period would be preferred, as it can be seen in Figs. 6.36a and 6.36b, that the response is not perfectly steady state. In fact in ocean engineering the time between independent sea state is taken equal to $3h$ [Veritas, 2002].

The spectral densities of the horizontal and vertical displacements, previously illustrated in Figs. 6.36a and 6.36b, is reported in Figs. 6.37a and 6.37b. The random response of the displacement has been normalized, so that the mean value of the process is zero, in order to obtain a more clear spectral density representation.

In the spectral densities, that as known are symmetric, are reported in the left side the significant wave frequency ω_w and ω_s, while in the right side of the graph are indicated with vertical lines the natural frequencies of the system.

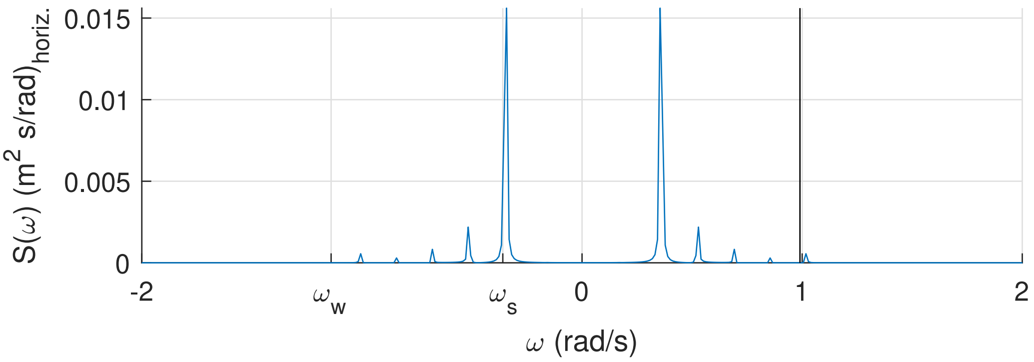

(a) Spectral density horizontal displacement at mid-span

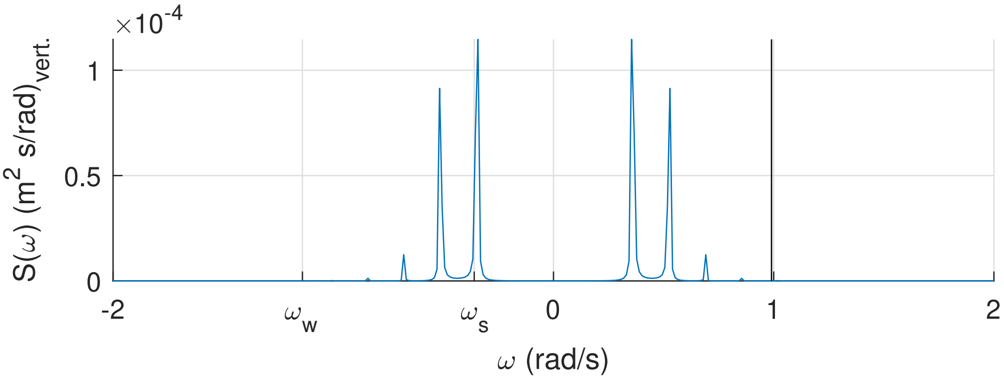

(b) Spectral density vertical displacement at quarter-span

Figure 6.37: Spectral densities of horizontal displacement at mid-span (a), and vertical displacement at quarter-span (b), irregular wave dynamic analysis, model B

It can be noticed in Figs. 6.37a and 6.37b that the tunnel response is mainly governed by the wave loading, and slightly by the first resonance mode, but only regarding the horizontal displacement.

Generally, in order to assume a process narrow-banded has to be fulfilled the following

$$\Delta\omega << \omega_{mid} \tag{6.7}$$

where $\Delta\omega$ is the range of frequencies of the response in the spectral density and ω_{mid} is the mid-point of that range.

Regarding the spectral density of the horizontal displacement at mid-span Fig. 6.37a, equation (6.7) become

$$\Delta\omega = 0.0256 << 0.36(rad/s) = \omega_{mid} \tag{6.8}$$

According to (6.8), the process can be assumed narrow-banded. This can be seen also in Fig. 6.36a where only few double peaks between an upcrossing and a subsequent downcrossing are present.

Considering the spectral density of the horizontal displacement at mid-span Fig. 6.37b, equation (6.7) become

$$\Delta\omega = 0.15 < 0.42(rad/s) = \omega_{mid} \tag{6.9}$$

Although the difference is not huge, the process can be fairly assumed narrow-banded.

Finally, both the horizontal and vertical displacement responses can be assumed narrow-banded. Therefore the statistical properties of the peaks and the extreme values of the structural response are studied. The Rayleigh distribution of peaks for a Gaussian narrow band process is adopted. The PDF computed with Rayleigh has low density for small and large peaks and a maximum density in correspondence of the standard deviation.

The PDFs of peaks and maxima for the horizontal and vertical structural responses are illustrated in Figs. 6.38a and 6.38b. In the figure is also marked as a comparison the maximum peak value obtained during the modified regular wave analysis, to which is subtracted the static displacement.

$f_A(a)$	is the PDF for the peak values
$f_{Amax}(a)$	is the PDF for the maximum of the peak values
$peakR.W.A$	is the maximum peak value obtained from the modified regular wave analysis.

It can be seen in Figs. 6.38a and 6.38b that the vertical peaks are around one order of magnitude lower than the horizontal one. Moreover, in both cases the PDF of the maximum of peak values tends to zero at values close to the maximum peak previously obtained in the

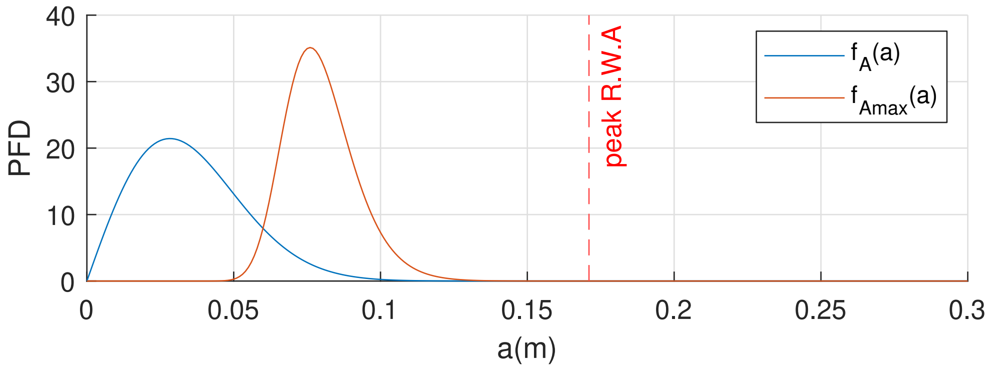

(a) Horizontal displacement at mid-span

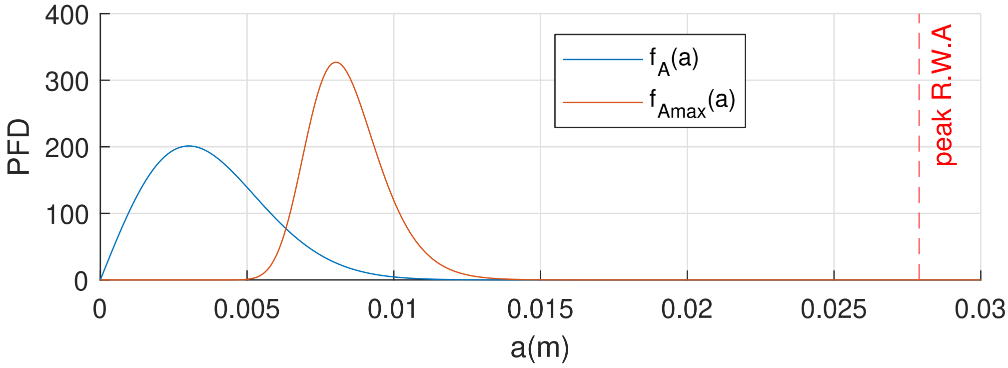

(b) Vertical displacement at quarter-span

Figure 6.38: PDF for the peak values and the maximum of peak values of the structural displacements, model B, irregular wave state

modified regular wave analysis. This result signify that the modified regular wave analysis is highly conservative. It can be recalled that in the modified R.W.A. the wave height are increased of 90%, the wave period reduced of 10%, and the wave direction is perpendicular to the tunnel longitudinal axis.

From $f_{Amax}(a)$ Figs. 6.38a and 6.38b it can be derived the expected value of A_{max} by calculating the following integral

$$E(A_{max}) = \int_0^\infty a f_{Amax}(a) da \tag{6.10}$$

It results that for the horizontal displacement the expected value of A_{max} is $0.08m$, while for the vertical displacement is $0.008m$. The static displacements are respectively $0.12m$ in the horizontal direction, and $0.18m$ in the vertical direction.

6.5.2 Accelerations

In this section are reported the results in terms of accelerations during an irregular wave analysis of model B. The accelerations are divided in horizontal and vertical directions.

In Figs. 6.39a and 6.39b the acceleration time series are reported at mid-span for the horizontal direction and at quarter-span for the vertical direction.

It can be clearly seen in Figs. 6.39a and 6.39b that the acceleration response is broad banded. For completeness the spectral densities of the vertical and horizontal accelerations are reported in Figs. 6.40a and 6.40b.

It is clear in Fig. 6.40a that the acceleration response is not a narrow-banded process. The distribution of peaks for general broad banded processes would require the exact number of peaks per unit of time. However, the expressions needed for analyzing the statistical properties of peaks, are of very limited practical use as they are difficult if not impossible to calculate [Newland, 2005b].

More rigorous wave analysis should be performed in the the design checks for extremes values. However this is out of scope in this thesis project, which focuses on different design concepts.

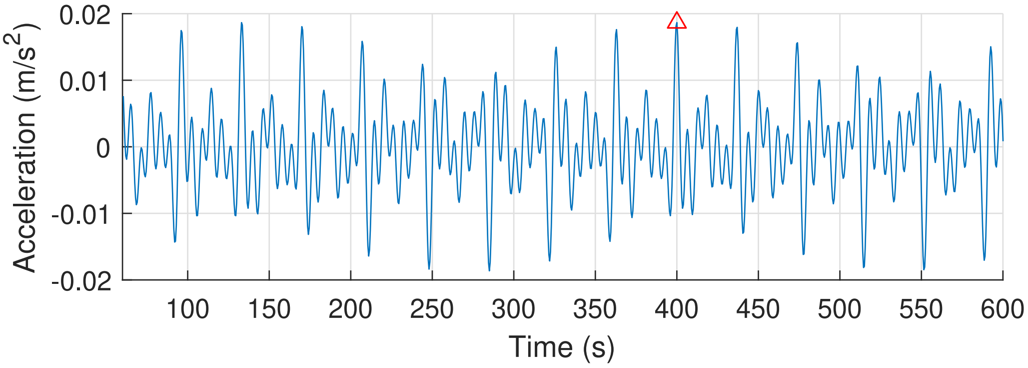

(a) Horizontal acceleration at mid-span

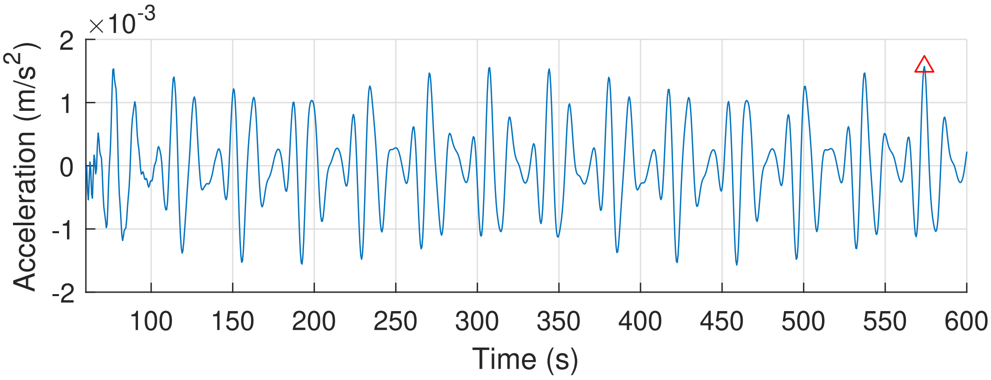

(b) Vertical acceleration at quarter-span

Figure 6.39: Horizontal acceleration at mid-span (a), and vertical acceleration at quarter-span (b), irregular wave dynamic analysis, model B

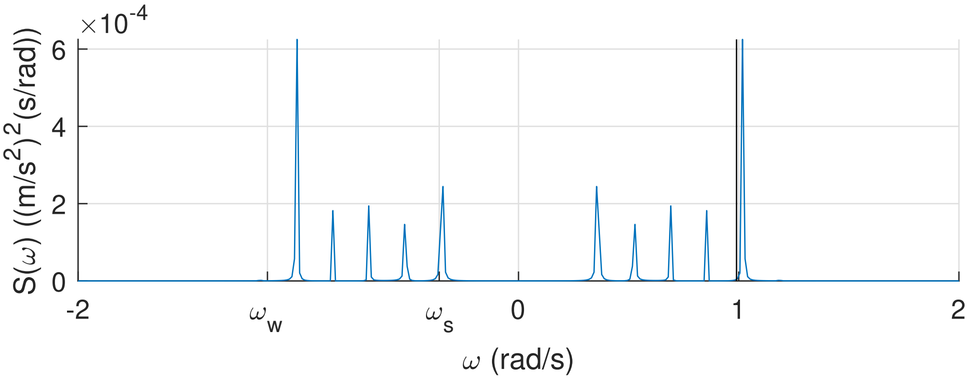

(a) Spectral densities of horizontal acceleration at mid-span

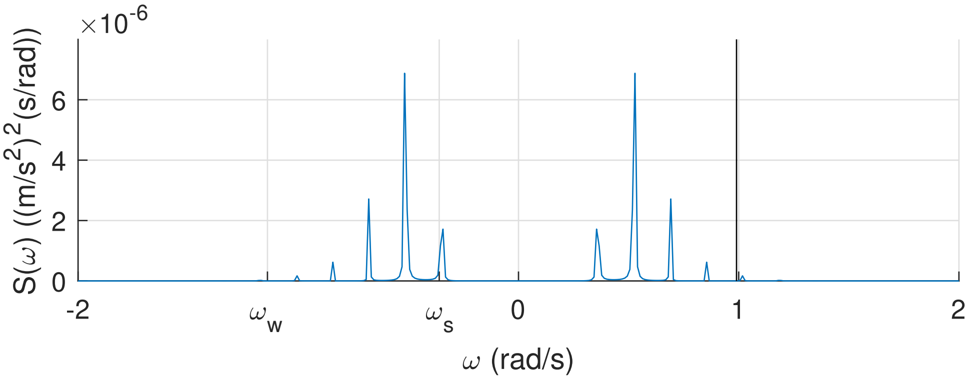

(b) Spectral densities of vertical acceleration at mid-span

Figure 6.40: Spectral densities of horizontal acceleration at mid-span (a), and vertical acceleration at quarter-span (b), irregular wave dynamic analysis, model B

6.6 Conclusions

In this chapter the double arch tunnel configuration is compared with a straight tunnel configuration through static, modal and dynamic analysis. In the static analysis there are no evident advantages on adopting a double arch configuration, due to the fact that large initial displacement affects the arch configuration.

The modal analysis shows that the double arch configuration is stiffer than the straight tunnel configuration, in fact it has lower first natural period, if the same number of tether is adopted.

From the regular wave dynamic analysis it appears that the double arch configuration considerably reduces the oscillation amplitudes. In particular the double arch configuration shows sufficient stiffness in the horizontal direction, indeed inclined tethers have proved to be unnecessary. The response in terms of accelerations is more dependent on the number of tethers adopted than on the tunnel alignment. However, horizontal accelerations are slightly reduced if the double arch configuration is adopted.

Generally, the double arch configuration is more sensitive than the straight configuration on BWR effects. The double arch configuration with a pair of vertical tethers at mid-span is tested under more severe sea state and the structural requirements are fulfilled. The rotational stiffnesses at the abutments are analyzed, and the results show that a convenient cost-effective solution is in between the pin and the fixed connections.

Finally an irregular wave analysis including the wave energy spreading is performed, and the probability distribution function of extreme values is computed. Comparing the irregular wave analysis with the regular wave analysis, it is found that the regular wave analysis is highly conservative based on the aforementioned assumptions.

Chapter 7

Conclusions

This thesis aimed to identify the effects of Submerged Floating Tunnel (SFT) alignment on the structural response. No specific studies regarding the SFT alignment are found in the literature, even thought several SFT designs have been proposed in the last two decades. The results obtained in each section are detailed in the following.

Initially, a conceptual design of the structure is performed. Aim of the conceptual design is to select the materials and find a preliminary tunnel configuration, through a simple and effective draft design process. Through the analytical methods established and some recommendations a suitable vertical and horizontal tunnel alignment is selected. It is so obtained a double parabolic arch configuration with a rise of $10m$ in the horizontal direction, and a rise of $5m$ in the vertical direction.

Three different variants of the double arch configuration are modelled in Abaqus. The first variant is a SFT with no tethers, the second one has a pair of vertical tethers at mid-span, and the third one has one inclined and one vertical tethers at mid-span. In order to make further comparison, a straight configuration SFT with a pair of vertical tethers at mid-span is also modelled in Abaqus.

The four models are improved individually, trough sensitivity studies and several cycles of analysis varying the main parameters.
In order to avoid compression forces in the inclined tether, a pulley connection between the two tethers is developed. In this way the forces between the tethers are kept automatically in equilibrium, and the probability of tether slacking is reduced.

The SFTs behaviour under the hydrodynamic loads due to waves and currents is investigated by means of static, modal and dynamic analysis. Through the static analysis, which neglects the fluid-structure interactions, is highlighted the dependence of each model on the BWR. The static analysis is performed in both calm water conditions, and severe sea state conditions where wave forces are modelled through the Morison equations. The results of the static analysis show that the double arch configuration has a large initial deformation due to buoyancy forces, in both horizontal and vertical directions. However, the double arch configuration is less dependent on wave and current static forces than the straight tunnel configuration.

The sea states that are take into consideration are dominated by swell waves, which have an low significant frequency. The double arch configuration has a generalized stiffness higher than the straight configuration, thus a higher first natural frequency, which reduces the probability of resonance with swell waves.

An harmonic regular wave dynamic analysis is performed for the four configurations, in order to have a conservative result the wave period is reduced by 10% and the wave height is increased by 90%. From the analysis it appears that the double arch configuration considerably reduces the oscillation amplitudes, while the structural accelerations are mainly governed by the number of tethers.

Moreover, it is found that the double arch configuration has sufficient horizontal stiffness and insufficient vertical stiffness. Therefore the configuration together with a pair of vertical tethers it appeared the most favourable solution. The effects on the dynamic response varying the rotational stiffnesses at the abutments are also studied.

An irregular wave analysis adopting the Torsethaugen double peak wave spectrum and considering the wave energy spreading function is performed. The irregular analysis demonstrates that the assumptions made during the harmonic wave analysis are highly conservative.

The thesis's work serves useful bases for the preliminary design of a SFT. The results obtained might be a starting point for a more thorough design.

Further developments of the present work consist in creating a more realistic model and consider different load conditions. Ship collision, earthquake, seaquake and partial flooding of the structure might be considered. Moreover, water ballast distribution can be optimize in order to reduce the bending moment amplitudes.

Additionally, soil-structure interaction effects may be analyzed and dissipation devices might be added at the tunnel ends. In a more detailed model it might be necessary to investigate the hydrodynamic coefficients. The amount of reinforcement and local post-tensioning of the concrete cross section is also necessary for a complete design.

This thesis project focuses in different design concepts, and once a concept has been determined more rigorous wave analysis should be performed in the design checks for extremes values.

Bibliography

Deokhee Won, Jihye Seo, Seungjun Kim, and Woo Sun Park. Hydrodynamic behavior of submerged floating tunnels with suspension cables and towers under irregular waves. *Applied Sciences (Switzerland)*, 9(24):1–27, 2019.

Dr. Techn. Olav Olsen, Norconsult, and Reinertsen. Bjørnafjord submerged floating tube bridge, k3/k4 technical report. 2016.

Xu Xiang, Arianna Minoretti, Mathias E. Eidem, Kjell H. Belsvik, Tale E. Aasland, and Mikhail Vodolazkin. Simplified hydrodynamic design procedure of a submerged floating tube bridge across the Digernessund of Norway. In *Proceedings of the ASME 2017 36th International Conference on Ocean, Offshore and Arctic Engineering OMAE2017*, 2017.

Shunji Kanie. Feasibility studies on various SFT in Japan and their technological evaluation. *Procedia Engineering*, 4:13–20, 2010.

Anna Feriani, Mariagrazia Di Pilato, and Federico Perotti. Dynamic behaviour of Submerged Floating Tunnels (SFT) subjected to seismic and hydrodynamic excitation. 2006.

F. M. Mazzolani, R. Landolfo, B. Faggiano, M. Esposto, F. Perotti, and G. Barbella. Structural analyses of the submerged floating tunnel prototype in Qiandao Lake (PR of China). *Advances in Structural Engineering*, 11(4):439–454, 2008.

F. Perotti, F. Foti, L. Martinelli, and M. Tomasin. Sfts under dynamic loads: New design issues and numerical simulation. *Maintenance, Safety, Risk, Management and Life-Cycle Performance of Bridges - Proceedings of the 9th International Conference on Bridge Maintenance, Safety and Management, IABMAS 2018*, (Npra 2014):885–892, 2018.

Lisland Torkjell. Mooring Pulley Tensioning System. European Patent Application, 2017. Application number 17174596.1.

DNV GL AS. Position mooring. *Offshore Standard*, 2015.

Knut Torsethaugen. Two peak wave spectrum model Simplified double peak spectral model for ocean waves. *Proceedings of the International Conference on Offshore Mechanics and Arctic Engineering - OMAE*, 2:175–180, 1993.

Federico Perotti, Roberto Paulucci, and Shi Chunxia. *Problems related to the seismic behaviour of Submerged Floating Tunnel.* PhD thesis, Politecnico di Milano, 2013.

Authors Gang, Luo Gang, Zhou Xiao-jun, and Chen Jian-xun. The Dynamic Response of an Experimental Floating Tunnel with Different Cross Sections under Explosive Impact The Dynamic Response of an Experimental Floating Tunnel with Different Cross Sections under Explosive Impact. 82:212–217, 2020.

Reinertsen and Olav Olsen Group. Feasibility study for crossing Sognefjorden Submerged Floating Tunnel. 2012.

S. Tariverdilo, J. Mirzapour, M. Shahmardani, R. Shabani, and C. Gheyretmand. Vibration of submerged floating tunnels due to moving loads. *Applied Mathematical Modelling*, 35(11):5413–5425, 2011.

Xiang Yiqiang and Chao Chunfeng. Vortex-induced dynamic response analysis for the submerged floating tunnel system under the effect of currents. *Journal of Waterway, Port, Coastal and Ocean Engineering*, 139(3):183–189, 2013.

Heng Lin, Yiqiang Xiang, Ying Yang, and Zhengyang Chen. Dynamic response analysis for submerged floating tunnel due to fluid-vehicle-tunnel interaction. *Ocean Engineering*, 166:290–301, 2018.

Y. Hong and F. Ge. Dynamic response and structural integrity of submerged floating tunnel due to hydrodynamic load and accidental load. *Procedia Eng.*, (4):35–50, 2010.

X. Long, F. Ge, L. Wang, and Y. Hong. Effects of fundamental structure parameters on dynamic responses of submerged floating tunnel under hydrodynamic loads. *Acta Mechanica Sinica*, pages 335–344, 2009.

Lu W.and Ge F., Wang L.and Wu X., and Hong Y. On the slack phenomena and snap force in tethers of submerged floating tunnels under wave conditions. *Marine Structures*, pages 358–376, 2011.

N. Kuznetsov, V. Maz'ya, and B. Vainberg. Introduction: Basic Theory of Surface Waves. *Linear Water Waves*, pages 1–18, 2009.

R. Moreau. *Integrated modelling of fully coupled fluid structure interactions using analysis, computations and experiments*, volume 75. Springer, New Jersey, U.S.A., 2003.

Murilo Teixeira Silva. Ocean surface wave spectrum. 2015.

Det Norske Veritas. *Free Spanning Pipelines, Recommended Practice DNV-RP-F105*. 2002.

Jimin He and Zhi Fang FU. *Modal Analysis*. Planta Tree, Linacre House, Jordan Hill, Oxford, 1st, edition, 2001.

B. N. Parlett and D. S. Scott. The Lanczos Algorithm with Selective Orthogonalization. *Mathematics of Computation*, 33(145):217, 1979.

Zhiqiang Song and Chenhui Su. Computation of Rayleigh Damping Coefficients for the Seismic Analysis of a Hydro-Powerhouse. *Hindawi*, (2046345), 2017.

Indrajit Chowdhury and Shambhu P. Dasgupta. Computation of Rayleigh damping coefficients for large systems. *Electronic Journal of Geotechnical Engineering*, 2003.

S. Chandrasekaran. *Dynamic Analysis and Design of Offshore Structures* , volume 5. Sringer Singapore, Singapore, 2018.

China Xiang and Yuan ZHENG. Nonlinear Stochastic Response of Offshore Structures: With Focus on Spectral Analysis CESOS Highlights. In *Conference & AMOS Visions Deepwater Research Centre Dalian University of Technology Dalian*, 2013.

C. Bajer and B. Dyniewicz. *Numerical Analysis of Vibrations of Structures under Moving Inertial Load* , volume 65. Springer Berlin Heidelberg, Berlin, Heidelberg, 2012.

Edward J. Norminton Erwin Kreiszyg, Herbert Kreiszyg. *Advanced Engineering Mathemathics*. Laurie Rosatone, 10 edition, 2008.

D. E. Newland. *Random Vibrations, Spectral & Wavelet Analysis*. Dover Publications, New York, third edition, 2005a.

Narasimhan Dey, P. and Walbridge. Calibrating Pedestrian-Bridge Standards for Vibration Serviceability. *Journal of Bridge Engineering*, pages 1–17, 2018.

American Association of State Highway Transportation Officials Task Force for Roadside Safety, Roadside design guide. American Association of State Highway and Transportation Officials, Washington, 2002.

Norwegian Public Roads. *Road tunnels*, volume 8. 1993.

Shy Bassan. Sight distance and horizontal curve aspects in the design of road tunnels vs. highways: Part II (trucks). *Tunnelling and Underground Space Technology*, pages 422–434, 2017.

A. Khennane. *Introduction to finite element analysis using MATLAB® and Abaqus.* CRC Press, Taylor & Francis Group, Boca Raton, 2013.

S. Attaway. *Matlab: A Practical Introduction to Programming and Problem Solving.* 2nd edition, 2011.

G. Papazafeiropoulos, M. Muñiz-Calvente, and E. Martínez-Pañeda. Abaqus2Matlab: a suitable tool for finite element post-processing. Advances in Engineering Software. pages 9–16, 2017.

Einar N. Strømmen. *Theory of bridge aerodynamics*. 2006.

K. Choi and N. Kim. *Structural Sensitivity Analysis and Optimization* . Springer New York, New York, NY, 1st edition, 2005.

D.E. Newland. An Introduction to Random Vibrations, Spectral & Wavelet Analysis. (7491):477, 2005b.

Appendix A

Matlab and Abaqus Codes

Appendix A

MATLAB and Abaqus Codes

A.1 Hand calculations double clamped arch, Matlab

```matlab
%% Geometry
Re=6.3; %External radius
Ri=5.5; %Internal radius
L=500;%Tunnel length
I=pi/64*((2*Re)^4-(2*Ri)^4); %Moment of inertia
A=pi*(Re^2-Ri^2); %Cross-section Area
E=36283^6; % Elastic modulus concrete C45/55
z=[0:1:L];
%% Load
v=1; %current velovity m/s
Cd=1;%drag coeficient
Ca=1;%added mass coefficient
wa=1029 ; %water density Kg/m^3
p=200; %water depth
T_s=17; %swell waves period
T_w=7; % wind waves period
```

```
omega_swell=2*pi/T_s;%swell waves frequency
omega_wind=2*pi/T_w; %wind waves frequency
h_s=3.42; %height swell
h_w=4.32; %height wind
amplitude_s=h_s/2;% swell wave amplitude
amplitude_w=h_w/2;% wind wave amplitude
g=9.81; %gravitational consstand
length_s=447.78 ;%length_s=((g*T_s^2)/(2*pi))*tanh(2*pi*p/length_s)
length_w=76.48 ;%length_w=((g*T_s^2)/(2*pi))*tanh(2*pi*p/length_w)
d=30+Re/2; %center of the tunnel depth
k_s=0.014031774; %swell wave number (by a trial and error procedure)
k_w=omega_wind^2/g; %wind wave number (deep water assumption is ...
    valid)
q_drag=(1/2*Cd*wa*v^2*2*Re); %drag force[N/m]
q_inertia_s=(1+Ca)*wa*(pi*Re^2)*(omega_swell^2)*exp(-(k_s*d))*h_s;% ...
    Morison inertia force swell waves
q_inertia_w=(1+Ca)*wa*(pi*Re^2)*(omega_wind^2)*exp(-(k_w*d))*h_w;% ...
    Morison inertia force wind waves
q_inertia=(q_inertia_s+q_inertia_w)/(pi*Re^2);%[N/m^2]
q=q_drag+q_inertia_s+q_inertia_w;%[N/m]
%%
fv=[8,9,10,11,12,14,14,15]; %Rise of the arch
M=zeros(length(fv),501);
T=zeros(length(fv),501);
r=[];
for kk=1:1:length(fv)
    f=fv(kk);
    r=[r,L^2/(8*f)+f/2];
alpha=[];
A0=[];
I0=[];
y=[];

    for i=0:1:L
    alphau=atan(-4*f*(2*i-L)/(L^2));
    alpha=[alpha,alphau];
    A0u=A*cos(alphau);
    A0=[A0,A0u];
    I0u=I*cos(alphau);
    I0=[I0,I0u];
    yu=4*f*(-(i/L)^2+(i/L));
    y=[y,yu];
    end

X1=-((15*atan(4*f/L)*I*L^3*q)/(4*(16*A*f^3 + ...
    45*atan(4*f/L)*I*L))); %[N*m], Redundant force
X2=((15*atan(4*f/L)*I*L^3*q)/(8*(16*A*f^3 + ...
    45*atan(4*f/L)*I*L)));%[N*m], Redundant force
M(kk,:)=(X1+(X2-X1).*(y./f))./10^6; %[MN*m], Bending moment ...
    distribution
T(kk,:)=(q.*cos(alpha).*((L/2)-z)+((sin(alpha)./f).
```

```
*(X2-X1-(L^2*q/8)))./10^3;%[KN] Shear distribution

end
%% Plot

figure(1)
plot(z,M)
xlabel('x(m)')
ylabel('Bending Moment [MN*m]')

%% Maximum Moment
 Mmax=[];
 r_variable=[];
 fvariable=[];
 for f_variable=8:0.1:15
     fvariable=[fvariable,f_variable];
     r_variableu=L^2/(8*f_variable)+f_variable/2;
X1m=-((15*atan(4*f_variable/L)*I*L^3*q)/(4*(16*A*f_variable^3 + ...
    45*atan(4*f_variable/L)*I*L)));
Mmaxu=X1m/10^6;
Mmax=[Mmax,Mmaxu];
r_variable=[r_variable,r_variableu];% Radius of curvature
 end
 figure
plot(fvariable,Mmax)
hold on
xline(10.39,'r:','Speed Limitation','LineWidth',4,'fontsize',20);
 title('Bending moment at the landfall')
  xlabel('rise f (m)')
 ylabel('Bending moment [MN*m]')
```

A.2 Simplified method for eigenfrequencies, Matlab

```
%%
Omega_s=[]; % Swell waves angular frequencies
Omega_h=[];% Wind waves angular frequencies
for n=1:4 %mode number
L=500;%Tunnel Length
Re=6.3;%Exterlan Radius
Ri=5.5;%Internal Radius
A_tether=2*0.410593593;%Area tether
L_tether=160-2*Re;%Length Tether
k=(n+1/2)*pi -((1)^n / cosh((n+(1/2))*pi));%k(n)
beta=k/L;%beta(n)
alpha=sin(k)/((-1^n)-cos(k));%alpha(n)
syms x
```

```
fun_phi=matlabFunction((exp(-beta*x)-cos(beta*x)+alpha*sin(beta*x) ...
    - ...
    ((-1^n)*((exp(beta*(x-L))-exp(-beta*(x+L)))))/(1+exp(-2*k)))); ...
    % Modal shape
fun_phi_2=matlabFunction(beta^2*exp(-beta*x)+beta^2*cos(beta*x) ...
    -alpha*beta^2*sin(beta*x)-((-1^n)*((beta^2*exp(beta*(x-L)) ...
    -beta^2*exp(-beta*(x+L)))))/(1+exp(-2*k))); % second order ...
    derivative modal shape
PHI=[];
PHI_2=[];
for i=1:0.1:L
     x=i;
     phi=fun_phi(x);
     phi_22=fun_phi_2(x);
PHI = [PHI,phi];
PHI_2=[PHI_2,phi_22];
end
x=[1:0.1:L];
%Normalization of modal shapes
max_value= max(PHI);
PHI_normalized=PHI/max_value;
figure();hold on; grid on
plot(x,PHI_normalized)
%% MASS
mass_pipe=101567.1768; %[Kg/m ] Tunnel mass
ro_w=1025;%[kg/m^3] Sea water density
Ca=1; % Added mass coefficient
added_mass=ro_w*pi*Re^2*Ca; % added mass
mass_pipe_tot=added_mass+mass_pipe;
added_mass_tether=A_tether*ro_w;
mass_tether=1.71*10^3+added_mass; %Kg/m points upwword
%% STiffness
I=pi/64*((2*Re)^4-(2*Ri)^4); % Moment of inertia tunnel cross-section
E=36283*10^6;%Pa
E_tether=1.12923E+11;%Pa
K_tet_ver=E_tether*A_tether/L_tether;
T_tehter=9.3964e+07;%Tension Tether
K_tet_hor=T_tehter/L_tether;
%% Modal Masses
M_sway=trapz(mass_pipe_tot.*PHI.^2)+(1/3)*mass_tether*PHI(L/2)^2;
M_heave=trapz(mass_pipe_tot.*PHI.^2)+mass_tether*PHI(L/2)^2;
%% MOdal Stiffnesses
K_sway=trapz((E*I).*PHI_2.^2)+K_tet_hor*PHI(L/2)^2;
K_heave=trapz((E*I).*PHI_2.^2)+K_tet_ver*PHI(L/2)^2;
%% EigenValue
omega_sway=sqrt(K_sway/M_sway);
omega_heave=sqrt(K_heave/M_heave);
Omega_s=[Omega_s,omega_sway];
Omega_h=[Omega_h,omega_heave];
end
```

A.3 Abaqus keyword of model B

```
*HEADING
Model B
*MATERIAL, NAME=CONCRETE
*ELASTIC
3.6283e+10, 0.20
*DENSITY
2.500e+03
*EXPANSION
0,
*DAMPING, ALPHA=0.009316 , BETA=0.006673
*MATERIAL, NAME=STEEL
*ELASTIC
2.100e+11, 0.300
*DENSITY
8.750e+03
*EXPANSION
 0.00
*DAMPING, ALPHA=0.009316 , BETA=0.006673
*MATERIAL, NAME=COMPOSITE
*ELASTIC
1.12923E+11, 0.226
*DENSITY
5.26E+03
*EXPANSION
 0.00
*DAMPING, ALPHA=0.009316 , BETA=0.006673
*AQUA
-200, 0, 9.81, 1025
0, -1, 0, -200
0, -1, 0, -00
*WAVE, TYPE=AIRY,WAVE PERIOD
1.33,15.3,0,0,-1
3.61,4.95,0,0,-1
*PART, NAME=TUNNEL
*INCLUDE,INPUT=pipe_nodes.inp
*NSET, NSET=PIPE_END
101, 601
*ELSET,ELSET=PIPE_END
1001,1500
*NSET, NSET=CENTRAL_NODES
351,226
*ELSET,ELSET=CENTRAL_NODES
1251,1126
*NODE, NSET=CABLE_1
2001,   250,    16.3,   -200.000
2002,   250,    16.3,   -192.630
2003,   250,    16.3,   -185.260
```

```
2004,   250,    16.3,   -177.890
2005,   250,    16.3,   -170.520
2006,   250,    16.3,   -163.150
2007,   250,    16.3,   -155.780
2008,   250,    16.3,   -148.410
2009,   250,    16.3,   -141.040
2010,   250,    16.3,   -133.670
2011,   250,    16.3,   -126.300
2012,   250,    16.3,   -118.930
2013,   250,    16.3,   -111.560
2014,   250,    16.3,   -104.190
2015,   250,    16.3,   -96.820
2016,   250,    16.3,   -89.450
2017,   250,    16.3,   -82.080
2018,   250,    16.3,   -74.710
2019,   250,    16.3,   -67.340
2020,   250,    16.3,   -59.970
2021,   250,    16.3,   -52.600
*NODE, NSET=CABLE_2
2101,   250,    3.7,    -200.000
2102,   250,    3.7,    -192.630
2103,   250,    3.7,    -185.260
2104,   250,    3.7,    -177.890
2105,   250,    3.7,    -170.520
2106,   250,    3.7,    -163.150
2107,   250,    3.7,    -155.780
2108,   250,    3.7,    -148.410
2109,   250,    3.7,    -141.040
2110,   250,    3.7,    -133.670
2111,   250,    3.7,    -126.300
2112,   250,    3.7,    -118.930
2113,   250,    3.7,    -111.560
2114,   250,    3.7,    -104.190
2115,   250,    3.7,    -96.820
2116,   250,    3.7,    -89.450
2117,   250,    3.7,    -82.080
2118,   250,    3.7,    -74.710
2119,   250,    3.7,    -67.340
2120,   250,    3.7,    -59.970
2121,   250,    3.7,    -52.600
*ELEMENT, TYPE=B31, ELSET=CABLE_1
2001,   2001,   2002.000
2002,   2002,   2003.000
2003,   2003,   2004.000
2004,   2004,   2005.000
2005,   2005,   2006.000
2006,   2006,   2007.000
2007,   2007,   2008.000
2008,   2008,   2009.000
2009,   2009,   2010.000
2010,   2010,   2011.000
```

```
2011,   2011,   2012.000
2012,   2012,   2013.000
2013,   2013,   2014.000
2014,   2014,   2015.000
2015,   2015,   2016.000
2016,   2016,   2017.000
2017,   2017,   2018.000
2018,   2018,   2019.000
2019,   2019,   2020.000
2020,   2020,   2021.000
*ELEMENT, TYPE=B31, ELSET=CABLE_2
20101,  2101,   2102.000
20102,  2102,   2103.000
20103,  2103,   2104.000
20104,  2104,   2105.000
20105,  2105,   2106.000
20106,  2106,   2107.000
20107,  2107,   2108.000
20108,  2108,   2109.000
20109,  2109,   2110.000
20110,  2110,   2111.000
20111,  2111,   2112.000
20112,  2112,   2113.000
20113,  2113,   2114.000
20114,  2114,   2115.000
20115,  2115,   2116.000
20116,  2116,   2117.000
20117,  2117,   2118.000
20118,  2118,   2119.000
20119,  2119,   2120.000
20120,  2120,   2121.000
*MPC
BEAM, 2021, 351
BEAM, 2121, 351
*NSET, NSET=CABLE
CABLE_1,CABLE_2
*ELSET, ELSET=CABLE
CABLE_1,CABLE_2
*NSET, NSET=CABLE_UP
2021,2121
*NSET, NSET=CABLE_LOW
2001,2101
*ELSET,ELSET=CABLE_UP
2020,20120
*BEAM SECTION, ELSET=CABLE, MATERIAL=COMPOSITE, SECTION= PIPE
1.029,0.068
0,1,0
*ELSET, ELSET=PIPE1001
1001
*INCLUDE,INPUT=beam_orientation.inp
*INCLUDE,INPUT=water_surf.inp
```

```
*NSET,NSET=WATER_CENTER
22006
*SURFACE SECTION, ELSET = WATER_SURF, AQUAVISUALIZATION = YES
*END PART
*INITIAL CONDITIONS,TYPE=TEMPERATURE
TUNNEL.PIPE, 0.
*ASSEMBLY, NAME=ASSEMBLY_TUNNEL
*INSTANCE, NAME=TUNNEL, PART=TUNNEL
*END INSTANCE
*NONSTRUCTURAL MASS, ELSET=TUNNEL.PIPE, UNITS=MASS PER LENGTH
18864.74988
*END ASSEMBLY
**********
*STEP , NLGEOM=YES, INC=10000
*STATIC
.1,1,1e-12,0.2
*BOUNDARY, OP=NEW
TUNNEL.PIPE_END,1,6,0
*BOUNDARY, OP=NEW
TUNNEL.CABLE_LOW,1,3,0
*DLOAD, OP=NEW
, GRAV, 9.8100, 0 , 0 , -1
** Name: Prestress   Type: Temperature
*Temperature, OP=new
TUNNEL.PIPE, 1.
** Load on the pipe
*DLOAD,OP=NEW
TUNNEL.PIPE,PB,0.953629744,12.6
TUNNEL.PIPE,FDD,1,12.6,1,1
TUNNEL.PIPE,FI,1,12.6,2,1
** Load in the cable
*DLOAD,OP=NEW
TUNNEL.CABLE,PB,1,2.055
TUNNEL.CABLE,FDD,1,2.055,1,1
TUNNEL.CABLE,FI,1,2.055,2,1
*DLOAD, OP=NEW
TUNNEL.PIPE, PZ, -40500
*OUTPUT, FIELD, FREQUENCY=1
*ELEMENT OUTPUT, ELSET=TUNNEL.PIPE
SF
*OUTPUT, FIELD, FREQUENCY=1
*ELEMENT OUTPUT, ELSET=TUNNEL.PIPE
SM
*OUTPUT, FIELD, FREQUENCY=1
*NODE OUTPUT, NSET=TUNNEL.PIPE
U
*OUTPUT, FIELD, FREQUENCY=1
*ELEMENT OUTPUT, ELSET=TUNNEL.CABLE
SF
*END STEP
**********
```

```
*STEP , NLGEOM=YES, INC=30000
*DYNAMIC, TIME INTEGRATOR=HHT-TF,ALPHA=-0.05
.1,150,1e-5,0.05
*DLOAD, OP=NEW
TUNNEL.PIPE, PZ, -40500
*DLOAD, OP=NEW
, GRAV, 9.8100, 0 , 0 , -1
*DLOAD,OP=NEW
TUNNEL.PIPE,PB,0.953629744,12.6
TUNNEL.PIPE,FDD,1,12.6,1,1
TUNNEL.PIPE,FI,1,12.6,2,1
TUNNEL.CABLE,PB,1,2.055
TUNNEL.CABLE,FDD,1,2.055,1,1
TUNNEL.CABLE,FI,1,2.055,2,1
*OUTPUT, FIELD, FREQUENCY=2
*NODE OUTPUT, NSET=TUNNEL.PIPE
U
*OUTPUT, FIELD, FREQUENCY=2
*NODE OUTPUT, NSET=TUNNEL.CABLE
U
*OUTPUT, FIELD, FREQUENCY=2
*NODE OUTPUT, NSET=TUNNEL.WATER_SURF
U
*OUTPUT, FIELD, FREQUENCY=2
*ELEMENT OUTPUT, ELSET=TUNNEL.PIPE
SF
*OUTPUT, FIELD, FREQUENCY=2
*ELEMENT OUTPUT, ELSET=TUNNEL.CABLE
SF
*OUTPUT, HISTORY
*ELEMENT OUTPUT, ELSET=TUNNEL.CABLE_UP
SF1
*ELEMENT OUTPUT, ELSET=TUNNEL.PIPE_END
SM
*ELEMENT OUTPUT, ELSET=TUNNEL.CENTRAL_NODES
SM
*ELEMENT OUTPUT, ELSET=TUNNEL.PIPE_END
SF
*ELEMENT OUTPUT, ELSET=TUNNEL.CENTRAL_NODES
SF
*NODE OUTPUT, NSET=TUNNEL.CABLE_UP
U2,U3
*NODE OUTPUT, NSET=TUNNEL.WATER_CENTER
U2,U3
*NODE OUTPUT, NSET=TUNNEL.CENTRAL_NODES
U2,U3,UR1
*NODE OUTPUT, NSET=TUNNEL.CENTRAL_NODES
AT
*END STEP
```

Appendix B

Modal Analysis

Appendix A

Modal Analysis

B.1 Modal shapes

Here are reported the first six modal shapes calculated with Abaqus/Aqua of models B Figure B.1, model C Figure B.2 and model D Figure B.3. The projections in the vertical and horizontal plane are shown for each modal shape.

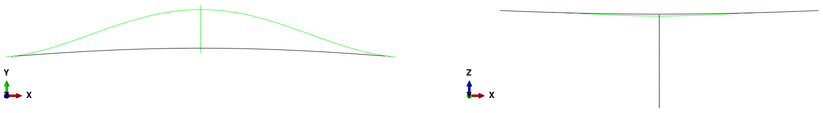

(a) Mode 1 horizontal projection **(b)** Mode 1 vertical projection

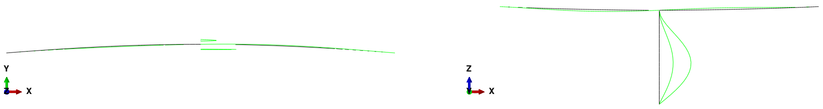

(c) Mode 2 horizontal projection **(d)** Mode 2 vertical projection

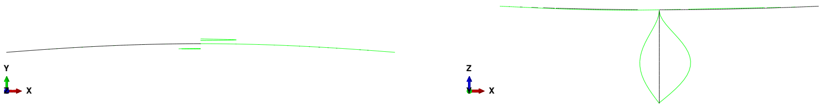

(e) Mode 3 horizontal projection **(f)** Mode 3 vertical projection

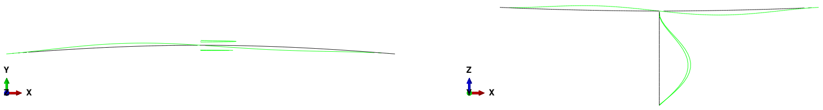

(g) Mode 4 horizontal projection **(h)** Mode 4 vertical projection

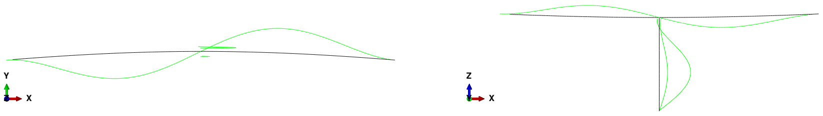

(i) Mode 5 horizontal projection **(j)** Mode 5 vertical projection

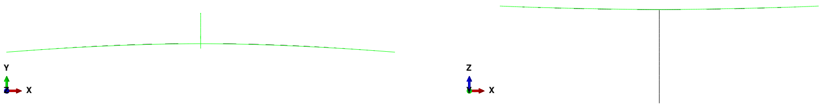

(k) Mode 6 horizontal projection **(l)** Mode 6 vertical projection

Figure B.1: Modal shapes illustration of first 6 modes, Model B

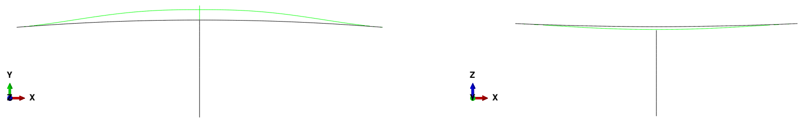

(a) Mode 1 horizontal projection **(b)** Mode 1 vertical projection

(c) Mode 2 horizontal projection **(d)** Mode 2 vertical projection

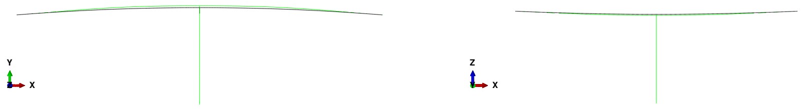

(e) Mode 3 horizontal projection **(f)** Mode 3 vertical projection

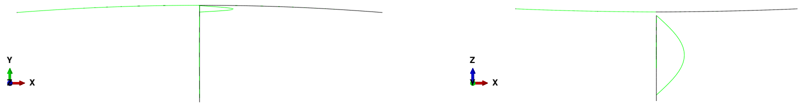

(g) Mode 4 horizontal projection **(h)** Mode 4 vertical projection

(i) Mode 5 horizontal projection **(j)** Mode 5 vertical projection

(k) Mode 6 horizontal projection **(l)** Mode 6 vertical projection

Figure B.2: Modal shapes illustration of first 6 modes, Model C

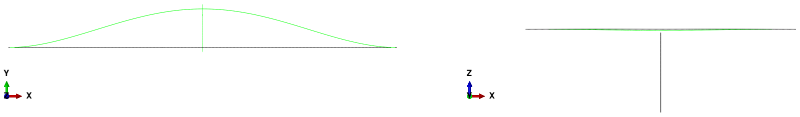

(a) Mode 1 horizontal projection **(b)** Mode 1 vertical projection

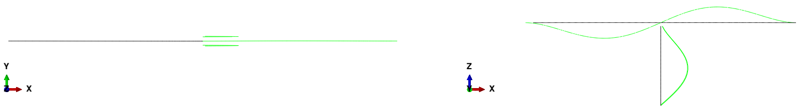

(c) Mode 2 horizontal projection **(d)** Mode 2 vertical projection

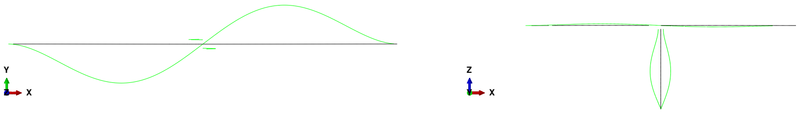

(e) Mode 3 horizontal projection **(f)** Mode 3 vertical projection

(g) Mode 4 horizontal projection **(h)** Mode 4 vertical projection

(i) Mode 5 horizontal projection **(j)** Mode 5 vertical projection

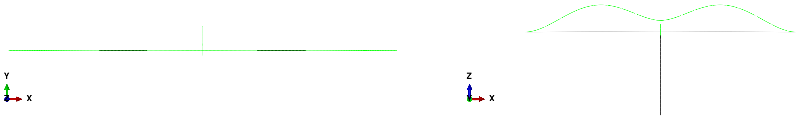

(k) Mode 6 horizontal projection **(l)** Mode 6 vertical projection

Figure B.3: Modal shapes illustration of first 6 modes, Model D

B.2 Rayleigh damping curves

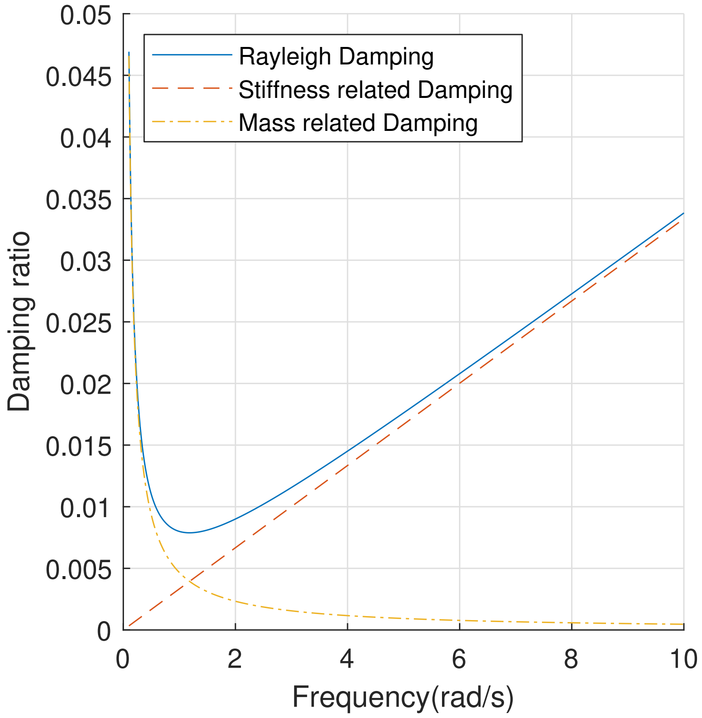

Figure B.4: Rayleigh damping ratio curve for model B

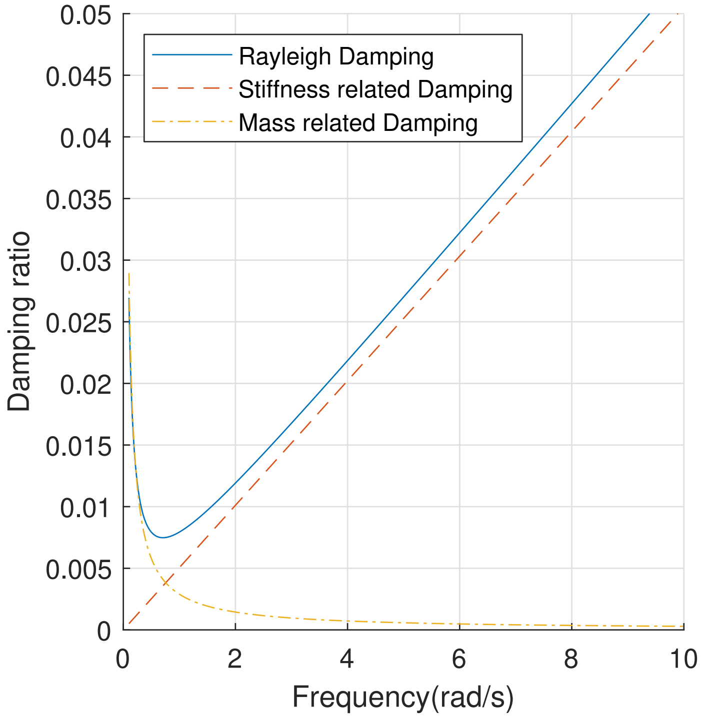

Figure B.5: Rayleigh damping ratio curve for model C

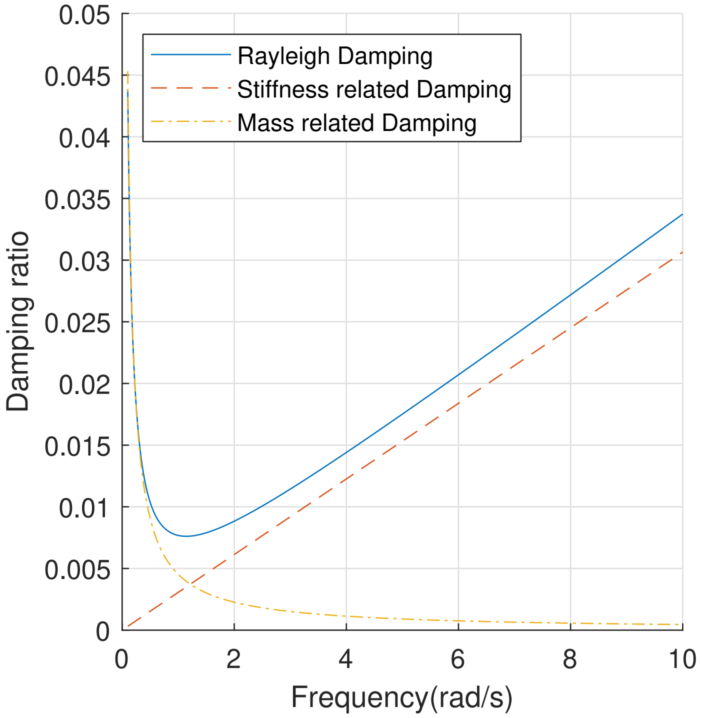

Figure B.6: Rayleigh damping ratio curve for model D

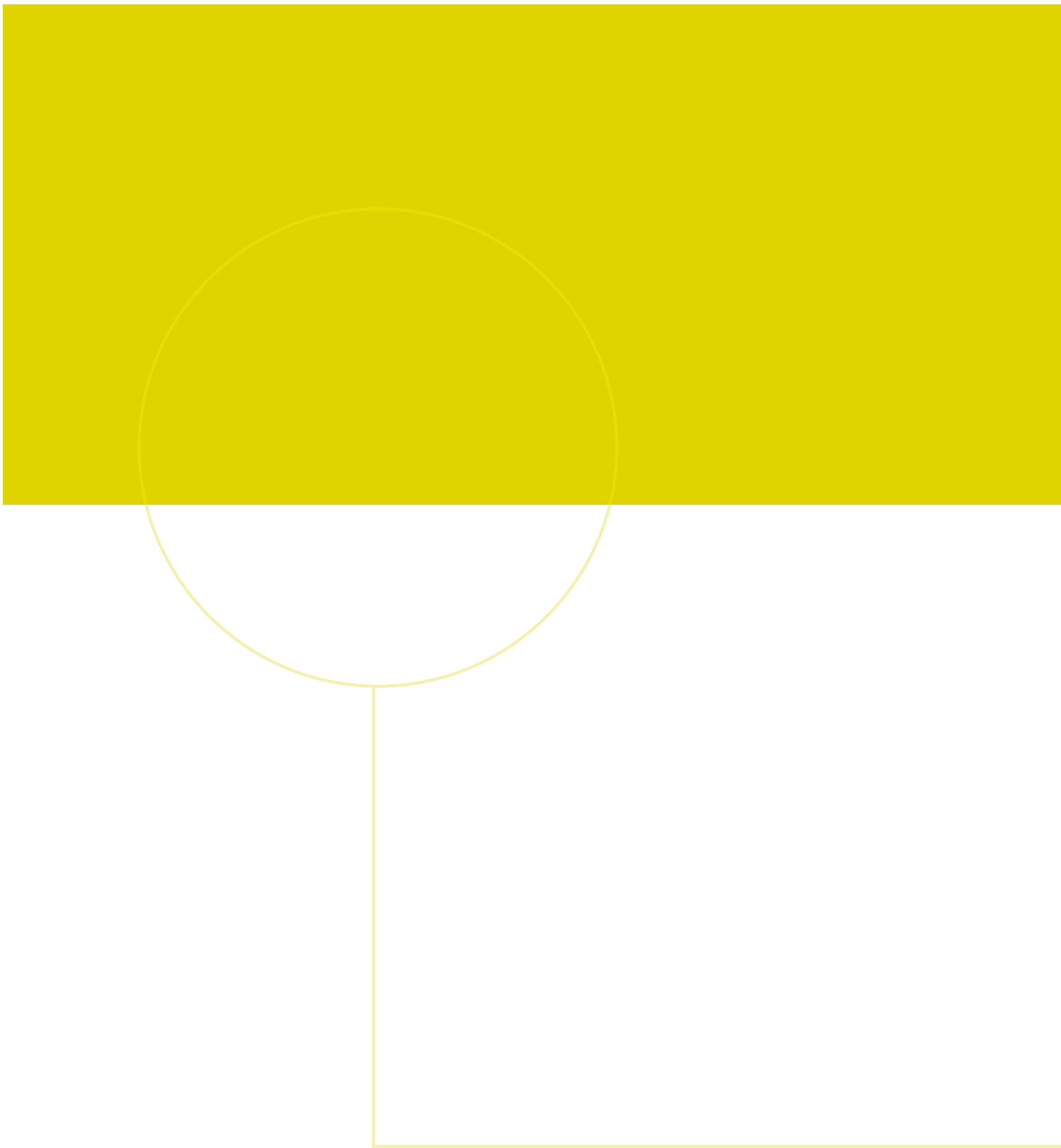

NTNU
Norwegian University of
Science and Technology